



UNIVERSITY OF HONG KONG

DOCTORAL THESIS

---

# Outflows from Star-forming Galaxies in the Early Universe

---

*Author:*

James Michael George  
NIANIAS

*Supervisor:*

Prof. Jeremy Jin Leong LIM

*A thesis submitted in fulfillment of the requirements  
for the degree of Doctor of Philosophy*

*in the*

Department of Physics  
Faculty of Science

2025/08/01



Abstract of thesis entitled

# **Outflows from Star-forming Galaxies in the Early Universe**

Submitted by

**James Michael George NIANIAS**

for the degree of Doctor of Philosophy

at The University of Hong Kong

in August, 2025

In this thesis, I present three studies centered on galactic outflows driven by star formation in the early universe, and the systems that play host to them.

Observations of outflowing molecular gas from star-forming galaxies are crucial to understanding how outflows may regulate the growth of galaxies' stellar mass, as molecular gas provides the fuel for star formation. In the first part of this thesis, I investigate signatures of outflows in molecular gas from dusty star-forming galaxies in the early universe ( $z > 4$ ). I re-visit observations of hydroxyl (OH) absorption lines from five such galaxies that a previous study identified as exhibiting evidence for molecular outflows. I show that the spectral features that were used to diagnose outflows are not statistically significant. Moreover, I show that these features suffer from inherent pitfalls that make them unreliable indicators of outflows. I then conduct a more thorough search for outflow signatures, utilising the full spatio-kinematic information as seen in spatially-resolved channel maps. I find spatio-kinematic patterns consistent with outflows in all five sources inspected, including one not identified in the prior study, thus providing more robust evidence of ubiquitous molecular outflows in such galaxies.

Due to limited spatial resolution when observing distant objects, searches for outflows in the early universe are often forced to rely on spectral signatures alone. For this reason, Lyman- $\alpha$  emission has become a valuable indicator of outflows due to its resonant nature, which couples the emergent line profile to the kinematics of the gas in and around galaxies. In my second study, I present a spectral analysis of 339 gravitationally-lensed star-forming galaxies in the early universe that exhibit Lyman- $\alpha$  emission. The lensing magnification provides a boost in signal-to-noise ratio, facilitating the detection of weak spectral signatures that I use, in conjunction with the Lyman- $\alpha$  profiles, to diagnose clumpy, multiphase outflows from these objects. I also search for relationships between the Lyman- $\alpha$  spectral profiles and other spectral features, finding evidence that sources with double-peaked Lyman- $\alpha$  profiles are associated with H II regions with more intense ionization fields yet slower outflows, while those with single peaks

are associated with more gas-rich environments and faster outflows. I compare these findings with idealised models that reproduce the Lyman- $\alpha$  profiles using expanding shells of partially neutral gas.

In the final study, I investigate the star formation history of one of the most highly gravitationally-magnified sources from the second study. A previous study found this object to have a compact size  $< 100$  pc, and a stellar population with a young age of  $< 10$  Myr. I perform spatially-resolved stellar population modelling of the source, using images from the James Webb Space Telescope. I present, for the first time, evidence that this source also harbors an older underlying stellar population (age  $\lesssim 1$  Gyr). I argue that the morphology is consistent with a picture in which the old stellar population extends to a larger radius than the young. I consider a scenario in which metal-enriched gas ejected into the circumgalactic medium by the first generation of stars is accreted to fuel the present star formation.

[Abstract is 499 words](#)

# **Outflows from Star-forming Galaxies in the Early Universe**

by

**James Michael George NIANIAS**  
BSc *HKU* MPhil *HKU*

A Thesis Submitted in Partial Fulfilment  
of the Requirements for the Degree of  
Doctor of Philosophy

at

University of Hong Kong  
August, 2025

COPYRIGHT ©2024, BY JAMES MICHAEL GEORGE NIANIAS  
ALL RIGHTS RESERVED.

## Declaration

I, James Michael George NIANIAS, declare that this thesis titled, "Outflows from Star-forming Galaxies in the Early Universe", which is submitted in fulfillment of the requirements for the Degree of Doctor of Philosophy, represents my own work except where due acknowledgement has been made. I further declare that it has not been previously included in a thesis, dissertation, or report submitted to this University or to any other institution for a degree, diploma or other qualification.

Signed:   

---

Date: 

---

 2025/08/01



## *Acknowledgements*

It is said that it takes a village to raise a child, and that is no less true of writing a PhD thesis. I am truly grateful to all the people who have supported and encouraged me in my journey as a scientist, despite it starting somewhat later in life than is customary. Chief among these is my supervisor, Prof. Jeremy Lim, who has taught me to walk the tightrope of doing meaningful, grounded science while also telling (I hope) a compelling story, and has demonstrated to me that one can be a good scientist while also being kind to one's colleagues. My mother, Felicity Hall, also taught me to be kind to others, and eventually convinced me to be kind to myself – advice that helped enormously in the writing of this thesis. My father, George Nianias, has been my steadfast supporter throughout, helping me to traverse the inevitable ups and downs of doing a PhD. My long-time partner, Wu Mei Yee, has been my greatest comfort and companion, never failing to make me smile even during stressful periods. I also thank my science family – my lab mates both within and outside our research group – for putting up with my eccentricities over the years, especially Amruth Alfred, Alex Chow, Arsen Levitsky, Sung Kei Li, Yuxuan Zeng, and Jiashuo Zhang.

James Michael George NIANIAS  
University of Hong Kong  
2025/08/01

# List of Publications

## JOURNALS:

- [1] **James Nianias**, Jeremy Lim, and Michael Yeung, "On the Evidence for Molecular Outflows in High-redshift Dusty Star-forming Galaxies" *The Astrophysical Journal*, vol. 963, number 1, pp. 19, March 2024.

## CONFERENCES:

- [1] **James Nianias**, Jeremy Lim, Yik Lok Wong, Gordon Wong, Ishika Kaur, and Wenjun Chen, "Tracing Outflows from Stellar Feedback in the Early Universe with Lyman- $\alpha$ " Accepted for publication in *Proceedings of the International Astronomical Union* 2024.



# Contents

<b>Abstract</b>	<b>i</b>
<b>Declaration</b>	<b>i</b>
<b>Acknowledgements</b>	<b>ii</b>
<b>List of Publications</b>	<b>iii</b>
<b>List of Figures</b>	<b>ix</b>
<b>List of Tables</b>	<b>xi</b>
<b>List of Abbreviations</b>	<b>xiii</b>
<b>1 Introduction</b>	<b>1</b>
1.1 Galactic Outflows and what Drives them . . . . .	2
1.2 The Cosmological Significance of Galactic Outflows . . . . .	4
1.2.1 Galaxy properties . . . . .	5
Stellar Mass . . . . .	5
Baryon fraction . . . . .	6
Mass-metallicity relation . . . . .	7
1.2.2 Metal enrichment of the CGM/IGM . . . . .	8
1.2.3 Reionization . . . . .	10
1.3 Galactic Outflows in the Local Universe . . . . .	11
1.3.1 M82: A Prototypical Galactic Outflow . . . . .	11
1.3.2 Other Outflows in the Local Universe . . . . .	13
Ly $\alpha$ emitters . . . . .	13
1.4 Galactic Outflows in the Early Universe . . . . .	17
1.4.1 Ionized/Neutral Atomic Gas . . . . .	17
1.4.2 Molecular Gas . . . . .	18
1.5 Overview . . . . .	21
<b>2 Candidate molecular outflows</b>	<b>25</b>
2.1 Introduction . . . . .	26
2.2 Archival Observations and Data Reduction . . . . .	30
2.2.1 Calibration . . . . .	30
2.2.2 Self-calibration . . . . .	33

2.2.3	Channel maps and integrated spectra . . . . .	34
2.3	Results and Analysis . . . . .	35
2.3.1	Integrated spectra . . . . .	35
2.3.2	Channel maps . . . . .	37
2.4	Discussion . . . . .	44
2.4.1	Outflow inferences . . . . .	44
2.4.2	Outflow properties . . . . .	45
2.4.3	Improving observing strategies . . . . .	46
2.5	Summary and Conclusion . . . . .	47
2.6	Acknowledgments . . . . .	49
2.7	Software . . . . .	50
<b>3</b>	<b>Outflow signatures from low-mass galaxies</b>	<b>51</b>
3.1	Introduction . . . . .	52
3.2	Catalogue . . . . .	56
3.3	Archival Observations and Data Reduction . . . . .	58
3.3.1	MUSE/VLT Integral Field Spectroscopy . . . . .	58
3.3.2	Sample Selection and Spectrum Extraction . . . . .	58
3.3.3	Initial Spectral Fitting . . . . .	58
3.3.4	Flagging potential contaminants . . . . .	61
3.3.5	Identifying and Aggregating Lensed Counterparts . . . . .	63
3.3.6	Atmospheric Residuals . . . . .	64
3.3.7	Final Sample . . . . .	65
3.4	Results and Analysis . . . . .	65
3.4.1	$\text{Ly}\alpha$ profiles . . . . .	65
3.4.2	Other emission/absorption lines . . . . .	68
Emission lines . . . . .	68	
Absorption lines . . . . .	70	
3.4.3	Averaged line profiles . . . . .	71
3.4.4	Fitting Expanding Shell Models . . . . .	76
3.5	Discussion . . . . .	79
3.5.1	Origin of Emission Lines . . . . .	79
3.5.2	Origin of Absorption Lines . . . . .	81
3.5.3	Origins of blue $\text{Ly}\alpha$ peaks . . . . .	82
3.5.4	Comparison with expanding shell models . . . . .	83
3.6	Summary and Conclusion . . . . .	84
3.7	Acknowledgments . . . . .	84
3.8	APPENDIX . . . . .	84
<b>4</b>	<b>SFH of a Lyman-<math>\alpha</math> source</b>	<b>87</b>
4.1	Introduction . . . . .	88
4.2	Archival Observations and Data Reduction . . . . .	90
4.2.1	Alignment and PSF Matching . . . . .	92

4.3	Results and Analysis	95
4.3.1	Source morphology	95
4.3.2	SED Extraction	98
4.3.3	SED Fitting	99
	Identifying low- $z$ interlopers	102
	Comparing SEDs along the arc	104
4.4	Discussion	107
4.4.1	LAE3.24 as a rejuvenated LAE	107
4.4.2	Source plane morphology	108
4.5	Summary and Conclusion	109
4.6	Acknowledgments	110
<b>5</b>	<b>Conclusions</b>	<b>111</b>
5.1	Conclusions	112
5.2	Ongoing/future work	113
5.2.1	SED modelling of Ly $\alpha$ emitters	113
5.2.2	Lensing reconstruction of LAE3.24	116



# List of Figures

1.1	Orion Molecular Cloud Complex	2
1.2	Schematic representation of a galactic outflow	3
1.3	Baryon cycle	4
1.4	Stellar mass function with vs. without outflows	5
1.5	Outflow efficiency and baryon fraction vs halo mass	6
1.6	Galaxy mass-metallicity relation	8
1.7	Quasar absorption line spectra	9
1.8	Lyman continuum escape	10
1.9	The outflow in M82	12
1.10	Lyman- $\alpha$ emitter with outflow	14
1.11	Lyman- $\alpha$ radiative transfer through an expanding shell	15
1.12	Simulated Lyman- $\alpha$ profiles	16
1.13	Blueshifted absorption in an LAE	18
1.14	Disc model of Herrera-Camus et al. (2019)	19
1.15	Spatially-resolved outflow from Herrera-Camus et al. (2019)	20
1.16	Example of a candidate high-z outflow spectrum in CO	21
1.17	Candidate outflows seen in OH absorption by Spilker et al. (2020b)	22
2.1	ALMA bandpasses used for OH observations	27
2.2	Bandpass calibration	31
2.3	Spatially-integrated spectra	36
2.4	SPT0202-61 channel maps	38
2.5	SPT0418-47 channel maps	39
2.6	SPT0441-46 channel maps	40
2.7	SPT2132-58 channel maps	41
2.8	SPT2319-55 channel maps	42
3.1	Example Ly $\alpha$ profiles	53
3.2	Blueshifted absorption in an LAE	54
3.3	Sample properties of lensed Ly $\alpha$ emitters	55
3.4	Example sources	59
3.5	Criterion for determining whether Ly $\alpha$ peaks are resolved	60
3.6	Dealing with contamination by cluster members	61
3.7	Lensed counterparts	63
3.8	Residual atmospheric lines	64

3.9	Distributions of redshift, Ly $\alpha$ luminosity and magnification in final sample	65
3.10	Examples of Ly $\alpha$ profiles	66
3.11	Distributions of various Ly $\alpha$ profile parameters	67
3.12	Velocity offsets of emission and absorption relative to Ly $\alpha$	69
3.13	Emission line EWs	69
3.14	Absorption spectra	70
3.15	Weak absorption seen in double-peaked spectra	72
3.16	Stacked low- and high-ionization absorption lines	73
3.17	Stacked individual absorption lines	74
3.18	Ly $\alpha$ offsets	74
3.19	Stacked emission lines	75
3.20	Measured systemic vs zELDA estimated redshifts	76
3.21	Distributions of zELDA fitted parameters	77
3.22	zELDA estimated intrinsic Ly $\alpha$ width vs measured emission line width	78
3.23	Measured emission line width for single vs double peaked sources	79
3.24	Observed vs. model line ratios	81
A.1	Spectra with unambiguous absorption lines (part 1 of 2)	85
A.2	Spectra with unambiguous absorption lines (part 2 of 2)	85
4.1	RGB image of MACS0416	89
4.2	Postage stamp cutouts of LAE3.24	91
4.3	Alignment of images	92
4.4	Identifying stars for PSF matching	93
4.5	Empirical PSFs	94
4.6	PSF residuals	94
4.7	UV - optical/NIR subtracted image of LAE3.24	95
4.8	Background fitting and subtraction	96
4.9	Cuts along the arc of LAE3.24	97
4.10	Apertures used to extract SEDs	98
4.11	Apertures used to generate uncertainties in the SEDs	99
4.12	Identification of intermediate- $z$ interlopers via SED fitting	100
4.13	Identification of low- $z$ interlopers via SED fitting	101
4.14	BIC of fitted models	103
4.15	Posterior distributions for single-burst models	104
4.16	Comparing best-fit model spectra	105
4.17	Posteriors for constant SFH models	106
4.18	Cartoon lensing configuration	108
4.19	Posterior distributions for double-burst models	110
5.1	Subtraction of cluster members	114
5.2	Example SEDs	115

# List of Tables

2.1	Candidate OH outflow systems in this study . . . . .	30
2.2	Results from spatially-integrated spectra . . . . .	37
3.1	MUSE observations . . . . .	57
3.2	Emission line ratios . . . . .	80
4.1	Filters Used to Image the Target . . . . .	92



# List of Abbreviations

<b>AGN</b>	Active Galactic Nucleus/i
<b>ALMA</b>	Atacama Large Millimeter/sub-millimeter Array
<b>BIC</b>	Bayesian Information Criterion
<b>CGM</b>	CircumGalactic Medium
<b>EUV</b>	Extreme UltraViolet
<b>HST</b>	Hubble Space Telescope
<b>ICGC</b>	IntraCluster Globular Cluster
<b>IGM</b>	InterGalactic Medium
<b>ISM</b>	InterStellar Medium
<b>JWST</b>	James Webb Space Telescope
<b>LAE</b>	Lyman-Alpha Emitter
<b>LBG</b>	Lyman Break Galaxy
<b>MUSE</b>	Multi-Unit Spectroscopic Explorer
<b>MZR</b>	Mass-Z[metallicity] Relation
<b>RT</b>	Radiative Transfer
<b>SED</b>	Spectral Energy Distribution
<b>SFH</b>	Star Formation History
<b>SFR</b>	Star Formation Rate
<b>sSFR</b>	specific Star Formation Rate
<b>SMF</b>	Stellar Mass Function
<b>SNa/e</b>	SuperNova/e
<b>SNR</b>	Signal-to-Noise Ratio
<b>VLT</b>	Very Large Telescope
<b>VMS</b>	Very Massive Star



## Chapter 1

# Introduction

## 1.1 Galactic Outflows and what Drives them

Galactic outflows (sometimes used interchangeably with the term "galactic super-winds"), consist of large-scale bulk motion of gas out of the interstellar medium of galaxy and into the surrounding intergalactic medium (IGM) or circumgalactic medium (CGM)<sup>1</sup>. They are powered by energetic processes that take place within the host galaxy itself (distinguishing them from other processes that can remove matter from galaxies such as ram pressure stripping and tidal interactions), chiefly energetic feedback from accretion onto central supermassive black holes – also known as active galactic nuclei (AGN) – and/or processes associated with star formation including radiation pressure, stellar winds, and supernovae (SNe). This thesis focuses on outflows powered by star formation, which are believed to play a dominant role in shaping the evolution of most galaxies.

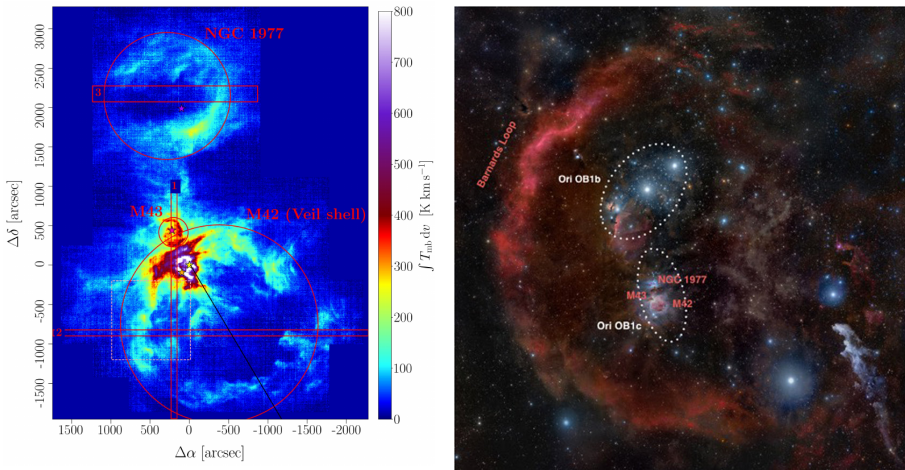


**Figure 1.1:** *Left:* Part of the Orion molecular cloud complex seen in integrated [C II] 158  $\mu\text{m}$  flux. The bubble structures indicated with circles show evidence of expansion, which is thought to be driven by stellar winds and/or thermal pressure from the hot, ionized gas in the interior. The red rectangles mark the positions of spectroscopic slits. Figure reproduced from Pabst et al. (2020). *Right:* RGB image of Barnard's Loop, believed to be a super-bubble driven by multiple SNe, with H $\alpha$  emission shown in red. Also indicated are the structures shown in Figure 1.1 for reference, as well as two associations of O/B type stars (OB associations) indicated with white dotted ellipses. Figure reproduced from Pabst et al. (2019).

To illustrate how feedback from star formation can drive outflows of gas from a galaxy, consider a star-forming region such as the Orion molecular cloud complex, the closest such region to the Sun hosting a significant number of newly-formed massive O- and B-type stars. Powerful stellar winds generated by some of these stars – such as that seen emanating from  $\theta^1$  Orionis C – can impart significant energy and momentum to the surrounding gas (see, e.g., Pabst et al. 2019). The high flux of ionizing photons generated by these stars also ionizes and heats the surrounding gas, driving up the

<sup>1</sup>The CGM is usually defined as gas outside a galaxy's disc but within its virial radius; see, e.g., Tumlinson et al. (2017)

thermal pressure and causing it to expand (Pabst et al., 2020). Intense UV radiation from massive stars may itself also exert outward pressure on the surrounding material through scattering and absorption by dust grains which couple to the gas. Similarly, extreme UV (EUV) photons ( $\lambda < 912 \text{ \AA}$ , the Lyman limit) and Lyman- $\alpha$  (Ly $\alpha$ ) photons exert radiation pressure due to their large scattering cross sections with neutral H in the ISM<sup>2</sup>. The expanding shells shown in the left panel of Figure 1.1 are a direct result of these processes. Furthermore, when massive stars exhaust their supply of fuel and collapse, ejecta from the resulting supernovae (SNe) impart outwards momentum into the surrounding ISM. Acting in concert, multiple SNe give rise to large expanding shells or super-bubbles, such as Barnard’s Loop, shown in the right panel of Figure 1.1 (Foley et al., 2023).

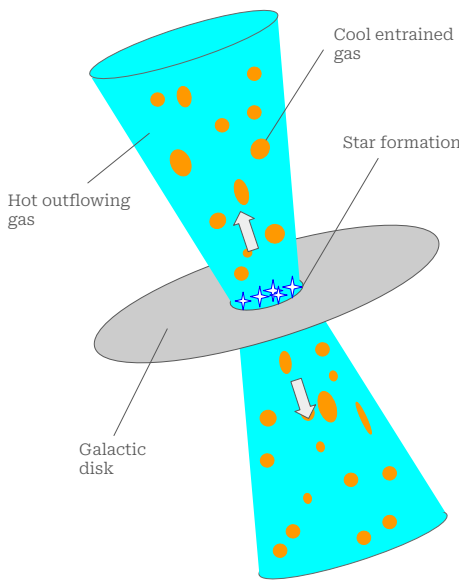


**Figure 1.2:** Schematic representation of a multiphase outflow from a star forming galaxy. Here, star formation is concentrated in the center of the galactic disc, from which a biconical hot outflow emerges, entraining cooler neutral/molecular gas.

If sufficiently energetic and acting over multiple star forming regions, the feedback processes outlined above give rise to hot winds that stream out perpendicular to the galactic disc. Clouds of cooler, denser neutral or even molecular gas can also be entrained by the hot gas, blowing it out of the galactic disc in a multiphase outflow (Thompson and Heckman, 2024). This picture is illustrated schematically in Figure 1.2. On the macro scale of whole galaxies, other factors may also come into play. For instance, cosmic rays (CR) – originating chiefly from SNe – may drive outflows by depositing momentum into the ISM as well as by heating it (Owen et al., 2023). While the precise details of the physics underpinning outflows and the relative importance of all these driving mechanisms is still hotly debated, they are believed to have profound

<sup>2</sup>In the specific case of Orion, radiation pressure (both on dust grains and neutral H) is not thought to produce a significant effect relative to other feedback mechanisms, though this does not rule out its importance to galactic outflows in general; see Thompson and Heckman (2024).

effects on the evolution of galaxies and the CGM/IGM. It is to these effects that we turn our attention next.

## 1.2 The Cosmological Significance of Galactic Outflows

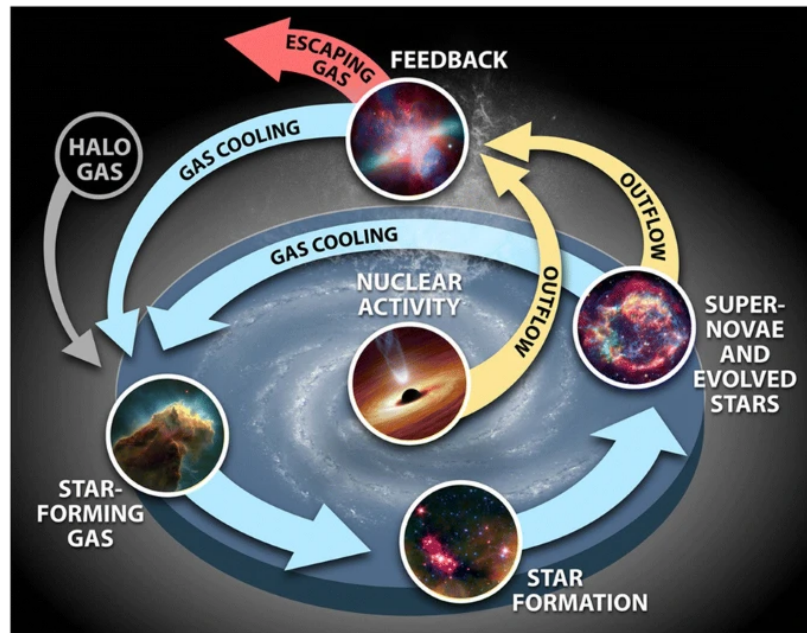


**Figure 1.3:** A visualisation of the baryon cycle highlighting the main pathways by which baryons are thought to "cycle" in and out of galaxies. Initially, cool gas accretes into dark matter halos, where some of it condenses to form stars. The energetic processes associated with short-lived massive stars (primarily SNe and stellar winds) then inject large amounts of energy into the surrounding ISM, which heats the gas, suppressing further star formation, as well as, at least in some cases, ejecting gas entirely from the galactic disc. Some of that gas may carry enough energy to escape the halo entirely, while some of it may eventually cool and fall back into the galaxy, beginning the cycle anew. Central supermassive black holes (AGN) are also known to drive energetic outflows, though their formation and growth is less well understood. Figure reproduced from Meixner et al. (2021).

Large-scale outflows of gas from galaxies are thought to be an important step in the baryon cycle – the "conveyor belt" of processes illustrated in Figure 1.3 that transports and transforms baryonic matter over the course of cosmic history. In this picture, gas cools and accretes into the potential wells of dark matter halos, where it can form stars once it reaches a sufficiently cool and dense molecular phase. Feedback from processes associated with star formation – discussed in detail in Section 1.1 above – both disrupts the surrounding molecular gas and removes gas from the galactic disc via outflows, thus suppressing further star formation. In this way, outflows are believed to play a crucial role in regulating the build-up of stellar mass in galaxies, thus helping to shape their overall distribution (known as the stellar mass function) in the present-day universe. When the outflowing gas escapes from the galaxy's host dark matter halo

entirely, the fraction of baryonic matter to dark matter in the halo (baryon fraction) is also suppressed. Furthermore, by enabling the escape of metal-enriched gas from galaxies, outflows are also posited to regulate galaxy metallicity and hence the mass-metallicity relation, as well as the build-up of metals in the CGM/IGM. Finally, outflows are also thought to have played an important role in cosmic reionization – the process wherein the previously neutral atomic IGM became ionized – by allowing EUV photons to escape from star-forming galaxies and into the IGM. The following section provides a review these processes and the role(s) played by outflows therein.

### 1.2.1 Galaxy properties

#### Stellar Mass

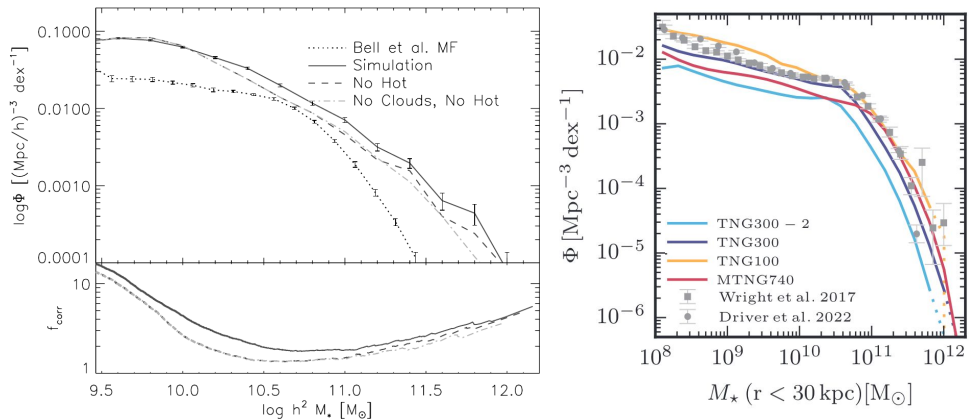


**Figure 1.4:** *Left:* A comparison of the SMF derived from cosmological simulations without stellar feedback versus the observed SMF from Bell et al. (2003), who estimate the masses of a large sample ( $N \sim 12000$ ) of nearby galaxies using stellar population synthesis models. The trace labelled "No Hot" is obtained by shutting off preventative feedback that stops the hot CGM from cooling and accreting into the galaxy, while the trace labelled "No Clouds, No Hot" shuts off both this effect as well as feedback preventing accretion of cold gas from the IGM. These feedback modes are preventative, i.e. preventing the accretion of new gas into the ISM rather than disrupting/ejecting the existing ISM, and mimic the effect of a radio mode AGN feedback. Reproduced from Kereš et al. (2009). *Right:* Simulated (solid lines) versus observed (grey points) SMFs from modern cosmological simulations including stellar (and AGN) feedback. The various simulations shown have different volumes and resolution, but all are able to reproduce the approximate shape of the observed SMF.

Cosmological simulations show that injections of energy and momentum from processes associated with star formation (as well as AGN) are required to suppress further star formation and thus explain the stellar masses of galaxies in the present day universe. For instance, Kereš et al. (2009) compare the stellar mass function (SMF) of galaxies derived from a feedback-free simulation with that observed in the present-day universe ( $z \sim 0$ ). Figure 1.4 shows this comparison in the upper panel, with the observed SMF as a dotted line, and the feedback-free simulated SMF as a solid line. In the lower panel is shown the fractional over-abundance between the predicted and

observed SMF. Without feedback from star formation/AGN, there are significant over-abundances in the number density of galaxies at all masses, especially at high and low masses, where this over-abundance can reach an order of magnitude. Moreover, they find that these differences cannot be explained by simply shutting off inflows of cool gas from the CGM/IGM. Instead, the authors argue that ejective feedback – i.e. outflows – is specifically required in low- to intermediate-mass objects ( $M_\star \lesssim 10^{10.5} M_\odot$ ) to remove the gas accreted from the IGM prior to the onset of star formation; otherwise this gas eventually cools and forms stars, leading to over-massive galaxies. Though the exact nature of the feedback is not determined in this study, the authors point to star formation as a natural source of the required energy and momentum needed to eject gas out of galaxies (particularly lower-mass galaxies) and into the CGM/IGM. In more massive galaxies, AGN-driven effects (outflows as well as heating of the CGM preventing accretion) become increasingly important or even dominant (see [Harrison 2017](#) and references therein). This explains why the discrepancy between the simulated feedback-free and observed SMF becomes greater towards high and low galaxy masses in Figure 1.4: star formation in low-mass galaxies is suppressed by star-formation-driven outflows, while in massive galaxies it is suppressed by AGN feedback. By modelling these feedback effects, contemporary cosmological simulations, such as MillenniumTNG ([Pakmor et al., 2023](#)), are able to reproduce the present-day SMF at low mass (and high) as shown in Figure 1.4. This highlights the importance of searching for outflows driven by star formation from low-mass galaxies, which is the focus of the study presented in Chapter 3.

### Baryon fraction

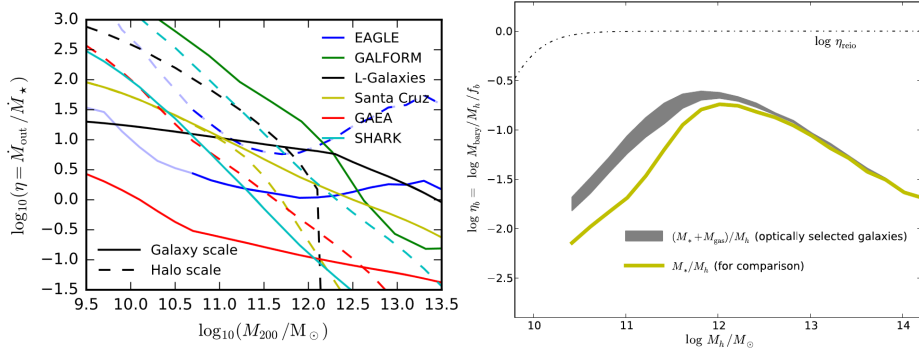


**Figure 1.5:** *Left:* Outflow efficiency (defined as the ratio of the mass outflow rate to the star formation rate) as a function of dark matter halo mass predicted by the EAGLE cosmological simulations ([Mitchell et al., 2020](#)) versus various semi-analytic models of galaxy evolution: GALFORM ([Mitchell et al., 2018a](#)), L-Galaxies ([Henriques et al., 2015](#)), Santa Cruz ([Somerville et al., 2015](#)), GAEA ([Hirschmann et al., 2016](#)), and SHARK ([Lagos et al., 2018](#)). Solid lines correspond to gas ejected from the ISM, while dashed lines correspond to gas entirely ejected from the halo including the CGM.. Reproduced from [Mitchell et al. \(2020\)](#). *Right:* Empirical baryon fraction as a function of halo mass inferred from abundance matching. Reproduced from [Papastergis et al. \(2012\)](#).

By removing gas from galaxies, outflows both reduce the gas mass and inhibit the growth of galaxies' stellar mass by removing the fuel for star formation. Consequently, outflows influence the baryon fraction of dark matter halos, i.e. the ratio of mass of baryonic matter in a galaxy (stars and gas) to that of dark matter halo in which the galaxy resides. The more efficient the outflow (in terms of  $\dot{M}_{\text{out}}/\dot{M}_\star$ , the ratio of outflow rate to star formation rate), the lower the baryon fraction of the host dark matter halo. A universal prediction among various simulations and semi-analytic models of galaxy feedback is that outflow efficiency increases with lower galaxy mass, as shown in the left panel of Figure 1.5. Intuitively, this is not surprising: lower-mass galaxies tend to reside in lower-mass dark matter halos, with shallower potential wells from which outflowing gas may escape more easily; furthermore, specific star formation rates (sSFR, the ratio of star formation rate to total galaxy mass) tend to increase with decreasing galaxy mass, providing more energy and momentum to drive outflows per unit gas mass. As a result, the baryon fraction of dark matter halos (and thus galaxies) may be expected to decrease with halo mass. Such a trend has been observationally inferred by Papastergis et al. (2012), who use abundance matching<sup>3</sup> between the observed baryonic masses of nearby galaxies (including gas mass measurements from H I 21 cm emission) and a theoretical  $\Lambda$ CDM halo mass function to estimate baryon fraction as a function of halo mass as shown in Figure 1.5. Note that the baryon fraction does not monotonically increase with halo mass across the entire mass range studied, but instead turns over at  $\sim 10^{12} M_\odot$ . This can be interpreted as a consequence of AGN feedback increasing towards higher galaxy mass, as in Figure 1.4.

### Mass-metallicity relation

One of the best-known galaxy scaling relations is the mass-metallicity relation (MZR, Lequeux et al. 1979) – the observed trend of increasing galaxy gas-phase metallicity with stellar mass. A recent measurement of the MZR obtained by Curti et al. (2020) for a sample of  $\sim 150\,000$  galaxies is shown in Figure 1.6, where the metallicity has been indirectly measured via oxygen abundance,  $12 + \log(\text{O}/\text{H})$ , which in turn is calculated using ratios between oxygen and Balmer lines along with estimates of the electron (gas) temperature,  $T_e$ . Other methods of estimating gas-phase metallicity yield similar results though with different normalisations, including direct measurements via absorption lines of individual blue supergiant stars (see Maiolino and Mannucci 2019, and references therein). As is the case with the baryon fraction and SMF, the MZR may be due in part to more efficient outflows in lower-mass galaxies, which may drive out metal-enriched gas from star forming regions more readily than in massive galaxies. Observational evidence that outflows are responsible for the MZR has been found by Chisholm et al. (2018), who study warm outflows in seven nearby star-forming galaxies. They find that (i) the outflowing gas has higher metallicity than the stars in the associated galaxies and (ii)

---

<sup>3</sup>Abundance matching is a technique used to search for relationships between two variables that cannot be simultaneously measured. In this case, the variables are baryonic mass, which is observationally estimated, and DM halo mass, which is not. The distribution in observed baryonic mass, appropriately binned, is compared with the theoretical distribution in halo mass. Assuming that the peaks of the two distributions coincide, it is possible to estimate the average baryonic to DM halo mass ratio in each bin.

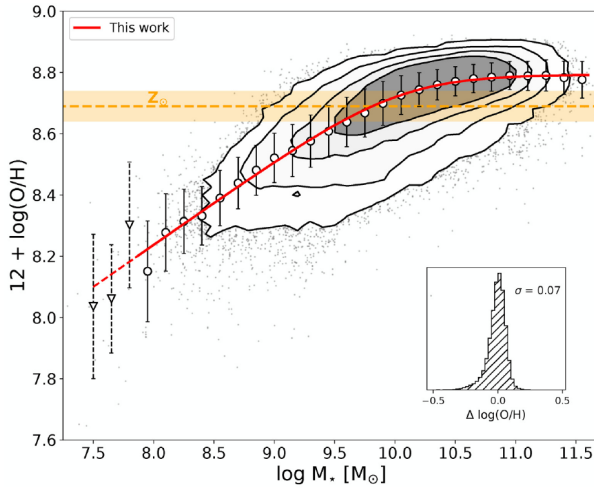


**Figure 1.6:** Mass metallicity relation shown via gas-phase oxygen abundance plotted against stellar mass for a sample of  $\sim 150\,000$  low-to-intermediate redshift ( $0.03 \lesssim z \lesssim 1.5$ ) galaxies. Figure reproduced from Curti et al. (2020).

this discrepancy decreases dramatically with increasing galaxy stellar mass, suggesting that metals are removed more efficiently from low-mass galaxies. Though contingent on metallicity measurements for the stars and gas that are based on different methods, these observations suggest that metal-enriched gas is indeed driven out of galaxies by outflows, suppressing the build up of metals. Simulations that incorporate outflows due to feedback from star formation such as the Feedback In Realistic Environments simulations (FIRE; Hopkins et al. 2014) are also able to reproduce the observed MZR.

### 1.2.2 Metal enrichment of the CGM/IGM

Another important ramification of outflows is the dispersal of metals into the CGM/IGM. The metallicity of the gaseous environment surrounding galaxies is of great importance to their formation and evolution. Even a small fractional abundance of metals can have a large impact on cooling rates of gas, and thus accretion into dark matter halos and eventual star formation. The presence of metals in the CGM/IGM has long been known through observations of distant quasars, which provide bright UV continuum sources against which metal absorption lines from the intervening gaseous halos at lower redshifts can be seen (e.g. Bahcall and Salpeter 1966). Figure 1.7 shows schematically how such measurements work. Numerous explanations for the metal enrichment of the IGM have been proposed, including dynamical removal of metal-enriched gas by galaxy mergers, outflows at very early epochs ( $10 \lesssim z \lesssim 20$ ), and outflows at later epochs ( $z \sim 2 - 3$ ) (Mongardi et al., 2018). Dynamical removal via mergers is no longer thought to play a dominant role as it can account for neither the distribution of metals in the IGM, nor the strength of the relation observed between galaxy mass and metallicity (Aguirre et al., 2001), leaving outflows as the most likely mechanism. Moreover, low-mass galaxies ( $\lesssim 10^9 M_\odot$ ), which are less able to retain their metal-enriched outflowing

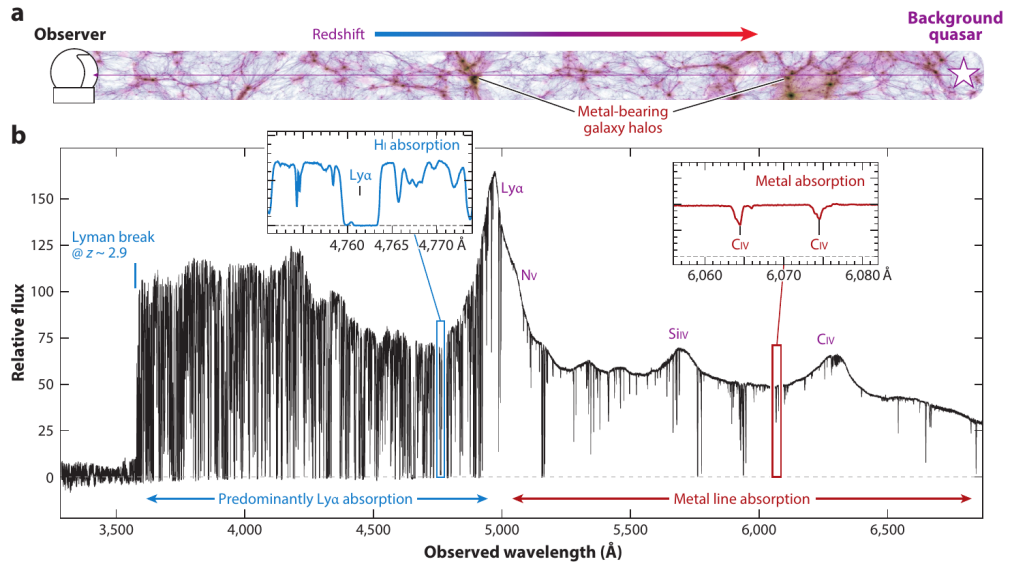


**Figure 1.7:** (a) a cartoon representation of quasar absorption spectra observations: intervening gaseous halos (at lower redshifts than the quasar) between the observer and the quasar create absorption lines against the UV continuum; (b) an example spectrum from a quasar at  $z = 3$ , showing Ly $\alpha$  forest absorption (left side) and metal absorption lines (right side). Reproduced from Péroux and Howk (2020).

gas in the CGM, are thought to be the primary drivers of IGM enrichment (Anglés-Alcázar et al., 2017). In Chapter 3, I present evidence for outflow signatures from such low-mass galaxies at  $3 \lesssim z \lesssim 7$ .

When absorption lines in background quasar spectra can be matched in redshift to nearby foreground galaxies, it is possible to investigate the relationships between individual galaxies and their CGM. Lundgren et al. (2021) apply this method to nine quasar sightlines with a total of 54 absorption systems at  $0.64 < z < 1.6$ , using the low-ionization Mg II doublet, which traces cool atomic gas. They show that (i) galaxies that are associated with circumgalactic Mg II absorption have enhanced star formation rates compared to those that are not, and (ii) Mg II absorption may be stronger for galaxies where the quasar sightline is within  $50^\circ$  of their minor axis. These findings are consistent with a picture of biconical metal enriched outflows driven by star formation as presented in Figure 1.2. In another study, Bordoloi et al. (2024) probe the CGM of seven star-forming galaxies at  $2.3 < z < 6.3$ , also via Mg II absorption, close to the sightline of a  $z = 6.33$  quasar. Based on the absorption line kinematics, they find that the metal-enriched gas is not gravitationally bound to the associated galaxies in five out of seven cases, contrasting with similar studies at lower redshift where most of the cool CGM is bound. This, they suggest, indicates that in the early universe, metal-enriched gas escapes more easily from galaxy halos to enrich the IGM.

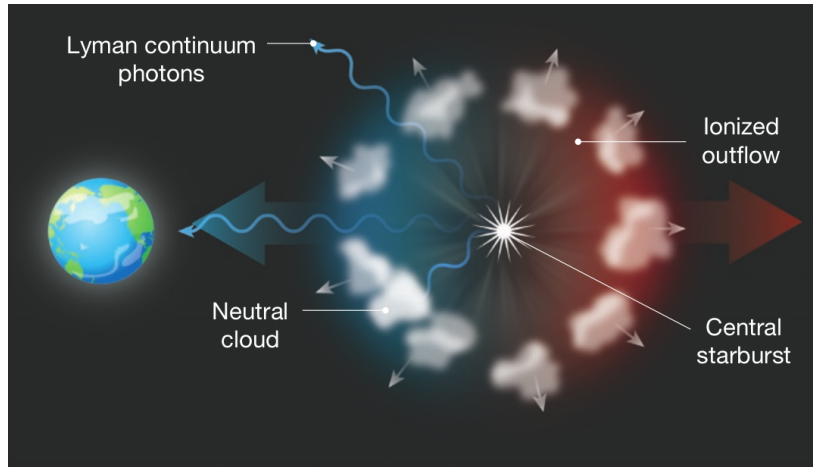


**Figure 1.8:** A cartoon representation of an outflow from a star-forming region driving ionized channels in the surrounding shell of neutral gas, through which LyC photons can escape into the IGM. Reproduced from Erb (2015).

### 1.2.3 Reionization

Cosmic reionization – wherein the previously neutral IGM became ionized between  $z \approx 10$  and  $z \approx 6$  – is another puzzle in which outflows are thought to play a key role. Reionization requires a large number of ionizing EUV photons, and the most promising candidate to supply these photons is young massive stars in the early universe. Since low-mass ( $\lesssim 10^9 M_\odot$ ) star-forming galaxies likely dominate the SMF in the early universe (Weaver et al., 2023), such objects are frequently cited as the primary drivers of reionization (e.g. Livermore et al. 2017). Outflows are thought to facilitate the escape of EUV photons – also known as Lyman continuum (LyC) photons – from sites of star formation by blowing holes in the surrounding neutral gas clouds as illustrated in Figure 1.8 (Erb, 2015). As outflows are more efficient in low-mass galaxies as discussed in Section 1.2.1, LyC escape fractions may be accordingly higher (Mascia et al., 2024). One of the easiest ways to detect and study low-mass galaxies hosting outflows is via Ly $\alpha$  emission, which arises from re-processed LyC photons produced in star-forming regions. When the ISM is sufficiently ionized and has low dust content<sup>4</sup>, the emergent Ly $\alpha$  line can have an equivalent width (EW)  $> 100 \text{ \AA}$ , facilitating the study of galaxies that are faint in the continuum (see Ouchi et al. 2020, and references therein). Furthermore, being a resonant line that is easily scattered by H $\text{i}$ , Ly $\alpha$  encodes the kinematics of the gas in and around star-forming galaxies. Radiative transfer modelling shows that observed Ly $\alpha$  spectral profiles are consistent with expanding shells of gas around star forming regions (see Section 1.3), which may enable the escape of LyC photons. Indeed, such Ly $\alpha$  profiles are seen well into the epoch of reionization (e.g. Jung et al. 2024). More information about Ly $\alpha$ -emitting galaxies is presented in Section 1.3, and studies of such objects are presented in Chapters 3 and 4.

<sup>4</sup>Dust grains can absorb Ly $\alpha$  photons and re-radiate their energy as thermal continuum in the infrared (IR), so that Ly $\alpha$  emission from dusty galaxies is strongly suppressed.

## 1.3 Galactic Outflows in the Local Universe

It is difficult, if not impossible, to understand the rationale and methods of searches for galactic outflows in the early universe without first discussing observations of galactic outflows in the local universe. The benefits of observing outflows in the local universe are obvious: greater spatial resolution and sensitivity allows us to map the spatio-kinematic structure of outflows and discs of their host galaxies out to much greater radii than is possible at high redshift. On the other hand, starburst galaxies are much rarer in the local universe than in the early universe, concordant with the overall decline in the cosmological star formation rate since  $z \sim 2$  (Madau and Dickinson, 2014). Furthermore, conclusions drawn based on outflows in local-universe galaxies may be of limited applicability to the early universe due to changing physical factors such as metallicity, which is generally much lower in the early universe (Madau and Dickinson, 2014), and the stellar initial mass function (IMF), which a growing body of evidence suggests may allow a greater proportion of very massive stars in the early universe (e.g. Li et al. 2023; Cameron et al. 2024). Nevertheless, there is a wealth of observations of star-forming galaxies hosting outflows in the local universe from which a number of important lessons may be learned.

### 1.3.1 M82: A Prototypical Galactic Outflow

The most extensively studied example of a galactic outflow from a star-forming galaxy is found in M82. At a distance of just 3.6 Mpc, M82 offers the opportunity to study such an outflow up close, and studies of it across the electromagnetic spectrum have strongly influenced expectations about outflows from star-forming galaxies in the early universe. Observations show that M82 hosts a prominent biconical, multiphase wind streaming out perpendicular to the disc. Figure 1.9 shows this wind in tracers of hot ionized gas (X-ray, from Bregman et al. 1995), warm atomic/ionized gas ( $\text{H}\alpha$ , from Shopbell and Bland-Hawthorn 1998), cold atomic gas ( $\text{H}\text{i}$  21 cm, from Martini et al. 2018), warm molecular gas ( $\text{H}_2$  2.12  $\mu\text{m}$ , from Veilleux et al. 2009), and cold molecular gas (CO (1–0), from Krieger et al. 2021). Studies in the mid-IR also reveal thermal emission from dust as well as emission from polycyclic aromatic hydrocarbons (Engelbracht et al., 2006). Semi-analytic 3D modelling of the wind in M82 by Yuan et al. (2023) estimates the combined mass of warm atomic and molecular gas to be substantial:  $\sim 8 \text{ M}_\odot \text{ yr}^{-1}$  and  $\sim 2 \text{ M}_\odot \text{ yr}^{-1}$  respectively, compared with an estimated star formation rate of  $\sim 4.1 \text{ M}_\odot \text{ yr}^{-1}$ . The same model also suggests that the gas is driven into the CGM/IGM, rather than falling back into the disc as a fountain, making it an outflow in the truest sense of the word. This also aligns with expectations from cosmological simulations, which invoke outflows as a way to suppress star formation and the build-up of gas in galaxies, as discussed in Section 1.2.1. That the outflow contains a substantial molecular component is particularly significant in this respect, as this gas comprises the direct fuel for star formation.

M82 provides observers with a sense of what signatures we can look for when searching for outflows in systems in the early universe. The wind clearly extends far

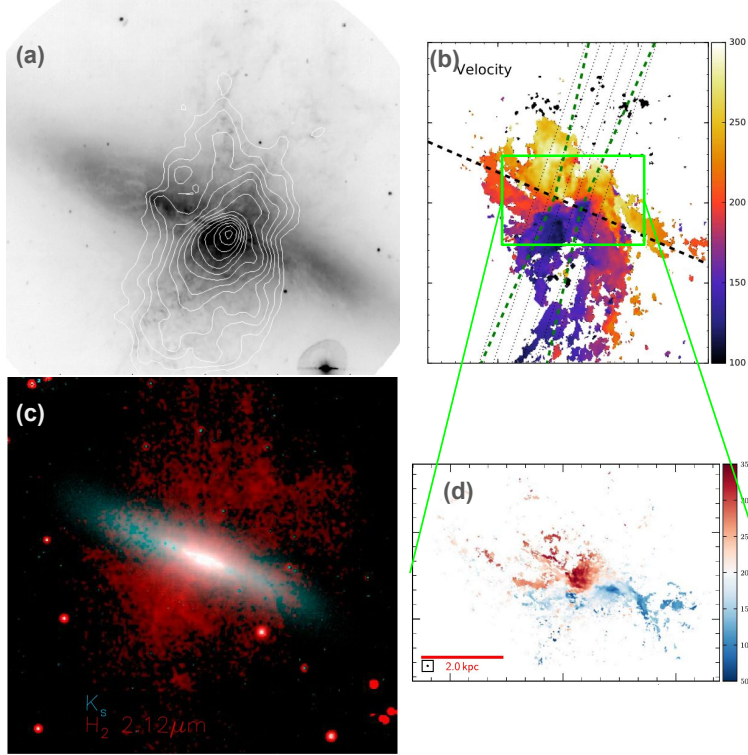


**Figure 1.9:** M82 and its prominent outflow containing (a) warm ionized/atomic gas emitting H $\alpha$ , from [Shopbell and Bland-Hawthorn \(1998\)](#), along with X-ray contours from [Bregman et al. \(1995\)](#); (b) velocity field of cold neutral gas seen in H $\text{I}$  21 cm emission, from [Martini et al. \(2018\)](#), showing clear evidence of motion out of the disc; (c) Warm molecular gas seen in H $_{\text{2}}$  2.12  $\mu\text{m}$  emission, from [Veilleux et al. \(2009\)](#); (d) velocity field of cold molecular gas seen in CO (1-0) emission, from [Krieger et al. \(2021\)](#).

beyond the disc – to almost 10 kpc – and in a direction approximately perpendicular to it. It also shows an ordered kinematic structure that is distinct from that of the disc. However, as can be seen from Figure 1.9(b) and (d), the extent of the wind in (line-of-sight) velocity space is somewhat modest, being just  $\sim \pm 150 \text{ km s}^{-1}$ , and indeed very close to the maximum line-of-sight rotational velocity of the stars in M82 as measured using stellar atmospheric absorption lines. This highlights one of the drawbacks of relying on spatially integrated line profiles alone to diagnose outflows, which is common in studies of high- $z$  galaxies where spatial resolution and sensitivity are limited. Partially this issue may simply be due to the large inclination angle of M82, estimated to be  $\sim 80^\circ$  ([Greve, 2011](#)), which, while helping to distinguish between the outflow and disc spatially, renders the line-of-sight velocity of the outflow relatively small. However, the 3D model of [Yuan et al. \(2023\)](#) suggests that the wind velocity out of the disc of M82 may not exceed  $150 \text{ km s}^{-1}$  at all. This result shows just how difficult it may be to detect outflows in spatially-unresolved spectra at high redshift, unless galactic outflows in the early universe are significantly faster than that of M82.

I discuss some of the potential difficulties in diagnosing outflows based on spectral signatures alone in Chapter 2.

### 1.3.2 Other Outflows in the Local Universe

Though M82 is the most spectacular outflow from a star-forming galaxy in the local universe, it is not unique. In a number of other nearby star-forming galaxies, comparable spatially-resolved outflows are observed in tracers including X-rays from hot ionized gas (Strickland et al., 2004), H $\alpha$  and [O III] $\lambda\lambda 4959, 5007$  from ionized/atomic gas (Bizyaev et al., 2019), H $_2$  ro-vibrational emission from warm molecular gas (Yui Dan et al., 2024), and CO from cold molecular gas (Krieger et al., 2019). Even at low redshift, however, the vast majority of outflows are not detected in this way, but rather via other techniques, such as blueshifted absorption lines seen in down-the-barrel spectroscopy (i.e. using the host galaxy itself as a continuum source against which interstellar absorption lines can be seen). We now turn the discussion to a class of low-redshift galaxies that exhibit signatures of outflows in Ly $\alpha$ , as well as in down-the-barrel absorption lines. These galaxies are the closest local-universe analogues of the high-redshift galaxies studied in Chapters 3 and 4, so warrant special attention.

#### Ly $\alpha$ emitters

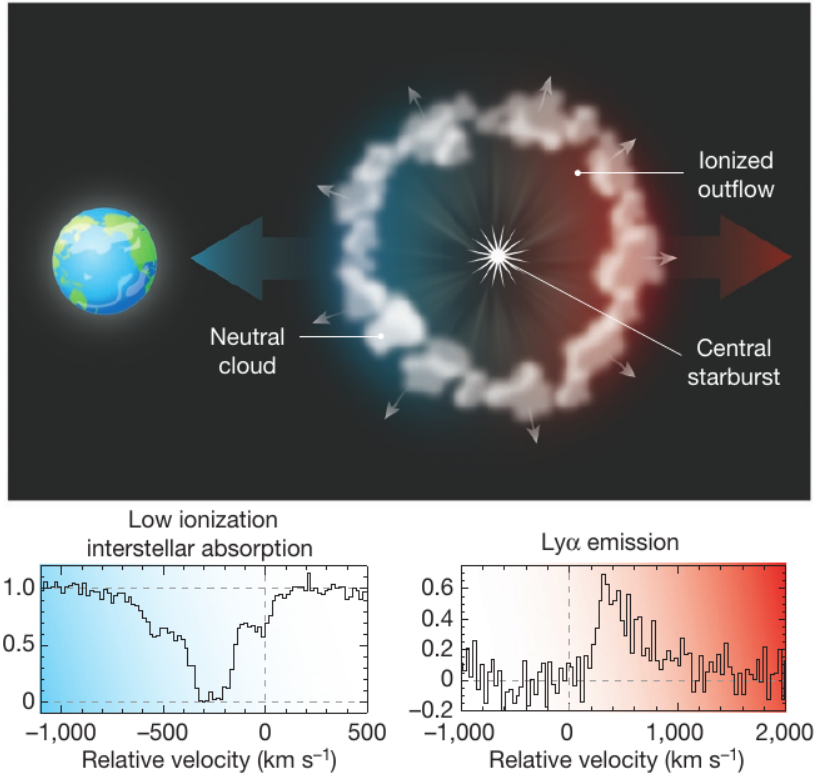
Evidence for outflows in ionized and neutral atomic gas are found in spectra of low-redshift/local ( $z < 0.2$ ) Ly $\alpha$  emitters (LAEs), such as those in the *Lyman Alpha Reference Sample* (LARS; see Hayes et al. 2013 for the original sample, Melinder et al. 2023 for the extended sample). The LARS galaxies have low to intermediate stellar masses, between  $\sim 10^{8.5} \text{ M}_\odot$  and  $\sim 10^{10.5} \text{ M}_\odot$ <sup>5</sup>, and star formation rates between  $\sim 10^{-1} \text{ M}_\odot \text{ yr}^{-1}$  and  $\sim 10^2 \text{ M}_\odot \text{ yr}^{-1}$ , placing them on or above the star-forming main sequence. These galaxies typically show asymmetric Ly $\alpha$  lines that are redshifted relative to the systemic velocity, as well as interstellar absorption lines that are blueshifted, similar to what is shown in the schematic diagram in Figure 1.10. In some instances, the redshifted Ly $\alpha$  profiles are accompanied by weaker, blueshifted peaks (resulting in double-peaked profiles). Such Ly $\alpha$  profiles have been shown to be qualitatively reproduced by Monte-Carlo radiative transfer (RT) models of expanding shells of partially-ionized gas (e.g. Ahn 2004, Verhamme et al. 2006, Duval et al. 2014). The major RT processes that give rise to the distinctive Ly $\alpha$  profiles in these models are as follows:

**Red peaks:** Ly $\alpha$  photons backscattered off the receding side of the neutral shell towards the observer are redshifted relative to the systemic velocity, and even more redshifted relative to the close (approaching) side of the shell; therefore, they are shifted out of resonance with, and hence can pass through, the approaching side towards the observer with minimal scattering.

**Blue peaks:** Secondary blueshifted Ly $\alpha$  peaks can arise through scattering through the front (oncoming) side of the expanding shell as shown in the schematic cartoon in

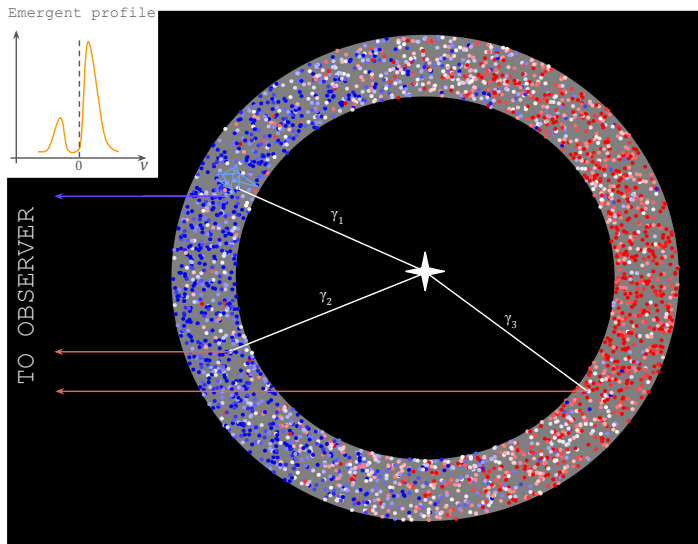
---

<sup>5</sup>C.f. an estimated mass of  $10^{11} \text{ M}_\odot$  for M31 (Sick et al., 2015).



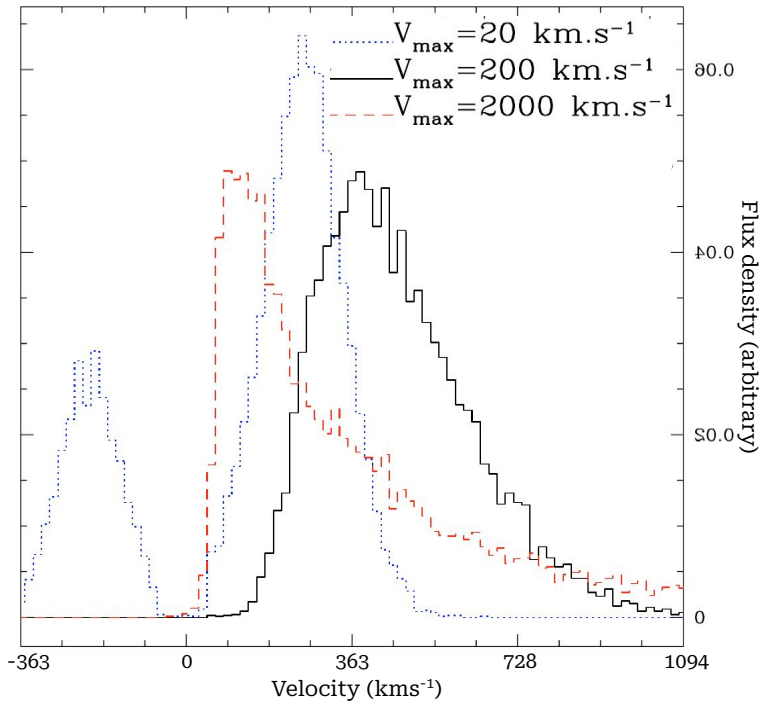
**Figure 1.10:** Above: schematic cartoon of an expanding shell model that can explain the observed spectra of LAEs. Ly $\alpha$  photons produced by the ionized gas in the receding (red) side of the outflow are shifted out of resonance with the approaching (blue) side, and so can pass out of the neutral shell towards the observer. This produces a redshifted Ly $\alpha$  peak as shown in the lower right panel. The approaching side of the neutral shell also screens the continuum source in the center, producing low-ionisation interstellar absorption lines that are blueshifted as shown in the lower left panel. Figure reproduced from Erb (2015).

Figure 1.11. There are a number of factors that may influence the appearance of blue peaks, including the outflow velocity, dust optical depth, clumpiness, and, possibly, inflows. If the outflow is slow and dust-free then Ly $\alpha$  photons can escape the approaching side of the shell in the blueshifted wing, without being absorbed by dust, after relatively few scatterings, as the required blueshift is not that great. The effect of increasing expansion velocity on the appearance of a blue peak is illustrated in the simulated line profiles from Verhamme et al. (2006) shown in Figure 1.12. Additionally, Duval et al. (2014) show that if the outflow is comprised of optically-thick clumps of (possibly dusty) neutral gas embedded in an ionized medium, then the strength of the blue peak may be slightly enhanced as compared to the homogeneous shell model. In both the clumpy and homogeneous scenarios, Ly $\alpha$  photons in the blue peak must undergo multiple scatterings to escape the outflow, and hence are very strongly attenuated by even small amounts of dust (the more scatterings they undergo within the outflow, the more likely it is that they eventually are absorbed by a dust grain).



**Figure 1.11:** Schematic cartoon illustrating how homogeneous expanding shells can give rise to double-peaked Ly $\alpha$  profiles (as shown in the upper left panel). Here, the colored points represent H $1$  atoms, with blue ones being blueshifted relative to the central star forming region (i.e. approaching the observer), and red ones being redshifted (i.e. receding from the observer). Due to the internal thermal motion of the gas, there are plenty of atoms in the approaching (and receding) side that are instantaneously at rest with respect to the systemic velocity (colored white). Thus, when a Ly $\alpha$  photon, such as  $\gamma_1$  or  $\gamma_2$ , enters the approaching side of the shell, it is scattered by this population of atoms, with which it is in resonance. The process of scattering changes not only the direction in which the photon travels, but also its wavelength; if it is scattered to shorter wavelengths like  $\gamma_1$ , then in order to escape the shell towards the observer it must be absorbed and re-emitted many times, as there are many more atoms that can absorb it. Only if it is lucky enough to be scattered into the extreme blue wings of the velocity distribution will it be able to escape the gas, as there are few atoms that will be in resonance with it. Conversely,  $\gamma_2$  gets scattered to longer wavelengths. Since there are now very few atoms in resonance with it (i.e. very few red atoms on the approaching side), it can pass through the shell to the observer with minimal scattering. The net result of this is that the approaching side of the outflow produces an asymmetric double-peaked profile with the red peak being higher than the blue. When we then add photons such as  $\gamma_3$  to this, which are backscattered off the receding side, the disparity between the red and blue peaks becomes even greater.

Of course, the geometry of real outflows, such as that in M82, is generally far from spherical shells. Radiative transfer models including more complex geometries such as those of [Orsi et al. \(2012\)](#) find significant effects on the emergent Ly $\alpha$  line profile when compared to spherical shells. Full magnetohydrodynamic radiative transfer simulations of LAEs performed by [Blaizot et al. \(2023\)](#) also demonstrate that when the geometry is not spherically-symmetrical, line-of-sight effects may become important. Another factor which may affect the emergent Ly $\alpha$  profile is inflows, in which case the resulting line profile is exactly the reverse of that for an outflow: a dominant blue peak, possibly with a secondary red peak. The simulations of [Blaizot et al. \(2023\)](#) show that a superposition of inflows with narrow opening angles and outflows with broad opening angles may



**Figure 1.12:** Simulated Ly $\alpha$  emission line profiles for expanding halos with varying velocity gradients. The central velocity of each halo is 0 km s<sup>-1</sup>, while the maximum velocities are indicated in the figure. The slowest of the halos, with a maximum velocity of just 20 km s<sup>-1</sup>, shows a clear blueshifted peak in addition to the redshifted peak. Figure adapted from Verhamme et al. (2006).

produce double-peaked Ly $\alpha$  lines, with a wide range of ratios between the blue and red peak flux.

While interpretation of the Ly $\alpha$  line profiles is model-dependent, the blueshifted interstellar absorption seen in low-redshift LAEs constitutes a more unambiguous signature of outflows. Observed absorption lines in low-redshift LAEs arise from low-ionisation species including Si II and C II, which are associated with predominantly neutral gas, but also from high-ionisation species such as Si IV which are associated with ionized gas. Rivera-Thorsen et al. (2015) find such blueshifted absorption features in nine out of 14 LAEs, with outflow velocities up to 500 km s<sup>-1</sup>. They also calculate the covering fraction of optically thick neutral gas as a function of velocity by comparing the relative absorption strengths of four Si II lines (in the optically thick limit, all absorption lines from a given species are saturated and so have the same depth regardless of relative transition probabilities; the fractional depth of the absorption, therefore, simply reflects the covering fraction). They find sources with a maximum covering fraction of  $\gtrsim 0.9$  to show very little or no Ly $\alpha$  escape from the inner star-forming regions, suggesting that while Ly $\alpha$  is a useful tool for detecting outflows, it is biased towards objects with sparser, more highly ionized ISM.

## 1.4 Galactic Outflows in the Early Universe

Observations of galaxies in the early universe usually lack the sensitivity and/or spatial resolution to directly detect biconical outflows like that seen in M82. As a result, many studies fall back on interpreting spatially-unresolved spectra. Studies that use optically-thin emission lines look for broad line components indicative of extreme velocity. If the velocity is high enough (i.e. higher than the estimated escape velocity of the host galaxy), an outflow is inferred. While this method can detect high-velocity outflows (more commonly driven by AGN), it may be of limited use for detecting more typical outflows, as discussed in Section 1.3.1. Absorption spectra and/or resonant lines like Ly $\alpha$  represent more promising ways of detecting slower outflows from spatially unresolved sources. In the following section, I summarise observations of candidate outflows in the early universe.

### 1.4.1 Ionized/Neutral Atomic Gas

Ly $\alpha$  emission has become one of the most valuable tools for detecting candidate outflows in the early universe. As discussed in Section 1.2.3, Ly $\alpha$  is a valuable tool for observing galaxies with low masses that may be extremely faint in the continuum. Observations of LAEs in the early universe and cosmic noon show ubiquitous asymmetric single- or double-peaked profiles like those discussed in Section 1.3 (Jones et al., 2012; Kulas et al., 2012; Orlitová et al., 2018; Claeysens et al., 2019). In one strongly gravitationally lensed LAE, Chen et al. (2021) find evidence of extended Ly $\alpha$ -emitting lobes around the central galaxy with velocity gradients extending along their lengths, possibly consistent with a resolved biconical outflow structure. Sometimes high-redshift LAEs also exhibit blueshifted interstellar absorption lines, either in individual objects as in Chen et al. (2021), or in stacked spectra such as in Shapley et al. (2003) and Jones et al. (2012). Figure 1.13 shows example spectra from one such object at  $z = 3.2$ , where the systemic velocity has been measured using the [O III] $\lambda 5007$  emission line. Studies of the stellar continuum from LAEs in the early universe find their spectral energy distributions (SEDs) to be well-characterised by low stellar masses ( $10^6 M_\odot \lesssim M_\star \lesssim 10^{9.5} M_\odot$ ), consistent with theoretical expectations of the primary drivers of reionization (Goovaerts et al., 2023).

In Chapter 3, I present a systematic search for outflow signatures from a sample of  $\sim 340$  gravitationally-lensed LAEs at  $2.9 < z < 6.7$ . Some of these objects have extreme lensing magnifications  $10 < \mu < 100$ , enabling study of intrinsically faint spectral features that may otherwise be undetected in un-lensed fields. Similarly to Kulas et al. (2012), I use optically thin emission lines to trace the systemic redshifts, and compare them to the Ly $\alpha$  spectral profiles and interstellar absorption lines. In Chapter 4, I present a study of the star formation history of a particularly highly magnified ( $\mu \approx 70$ ), compact (effective radius  $< 100$  pc) and low-mass ( $M_\star \sim 10^6 M_\odot$ ) object from this sample.

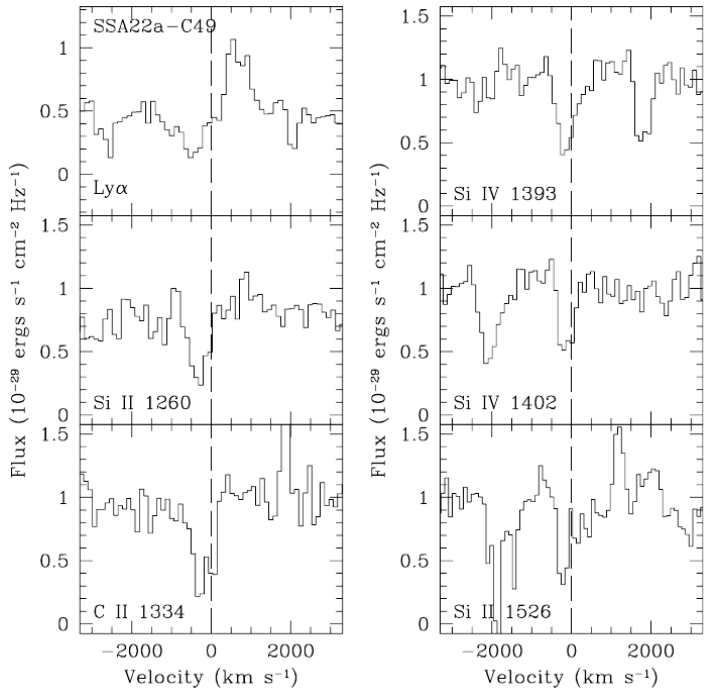


**Figure 1.13:** Blueshifted low-ionization absorption lines seen in an LAE with a single-peaked Ly $\alpha$  profile (upper left panel). The systemic velocity is measured using an optically-thin optical emission line. Figure adapted from [Kulas et al. \(2012\)](#).

### 1.4.2 Molecular Gas

As discussed in Section 1.3.1, studies of M82 have influenced expectations about the properties of outflows in the early universe. Though, as stated by [Krieger et al. \(2021\)](#), it is not clear what the relationship between the molecular and ionized/atomic phases of the outflow in M82 is – whether the molecular clouds condense out of the atomic/ionized phase, or are entrained in the outflow from within the disc – the observations make clear that molecular gas may indeed be found in outflows. Outflows containing molecular gas are of special significance when considering the role of outflows in suppressing star formation, as they constitute direct evidence of the fuel for star formation being driven out of the host galaxy.

The strongest evidence to date for outflows of cool molecular gas in the early universe comes from spatially-resolved studies of CO emission from systems hosting AGN. Perhaps the best example of this is from [Herrera-Camus et al. \(2019\)](#), wherein the authors utilise Atacama Large Millimeter/submillimeter Array (ALMA) CO(3–2) observations of a main sequence galaxy hosting an AGN at  $z = 2.3$ . Moment maps of this galaxy, shown in Figure 1.14, reveal a well spatially-resolved rotating disc. In order to disentangle the proposed outflow from the disc, they first construct a spatio-kinematic model of the disc based on the channel maps in the  $[-250, +250]$   $\text{km s}^{-1}$  velocity range (choosing this limited velocity range so as to mitigate as far as possible contamination by any outflowing gas, while still encompassing the velocity range of the

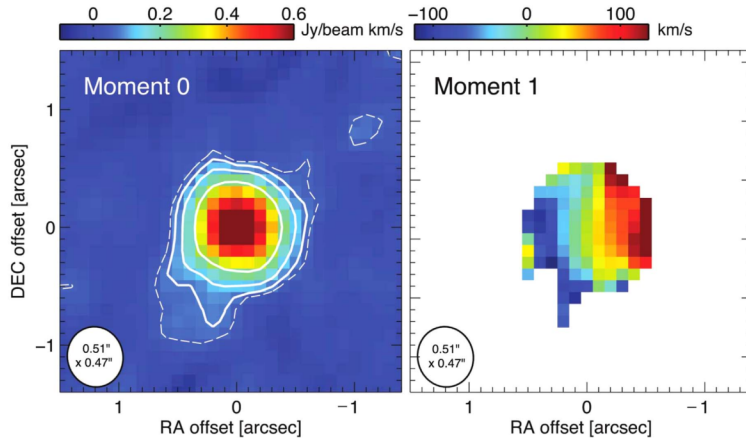


**Figure 1.14:** ALMA CO(3–2) moment maps of zC400528, a main sequence galaxy at  $z = 2.3$  that hosts an AGN. Clearly visible in the moment 1 map (right) are the structured dynamics of a rotating disc. Figure adapted from [Herrera-Camus et al. \(2019\)](#).

detectable disc as shown in the right panel of Figure 1.14). After subtracting the model from the ALMA spectral cube, they ascribe any remaining surface brightness in the channel maps to outflowing material. Figure 1.15 shows the ALMA CO(3–2) moment 0 map over the  $[-250, +250] \text{ km s}^{-1}$  velocity range (upper left panel), the residual after modelling the disc over the same velocity range and subtracting the model (upper right panel), the spatially-integrated spectrum before and after subtraction of the model disc (lower left panel), and the moment 0 map over the  $[+300, +700] \text{ km s}^{-1}$  velocity range (lower right panel). As is evident from the moment 0 map of the apparent outflow, it is well-distinguished from the disc kinematically, extending in velocity space far beyond the detectable disc. It is also spatially distinct from the disc, with statistically significant (i.e.  $> 3\sigma$ ) emission extending beyond the detectable disc up to  $\sim 10 \text{ kpc}$ . Furthermore, the brightness peak in the velocity range ascribed to an outflow coincides spatially with a region of the disc that has a relatively low projected velocity of  $\lesssim 100 \text{ km s}^{-1}$ , suggesting that it arises from the center of the host galaxy.

Despite the evidence presented above, caution must be exercised when interpreting such features as can be seen in the lower right panel of Figure 1.15, as it is not possible to conclusively rule out that such features could arise due to tidal interaction between the host galaxy and a second, lower-mass galaxy. Indeed, molecular gas has recently been detected by [Maeda et al. \(2024\)](#) in the tidal tails of interacting galaxies at low redshift.

Though such candidate outflows are, as yet, all ascribed to AGN feedback rather than star formation, they illustrate the best-case scenario for searching for molecular outflows at high redshifts: spectral signatures of highly blueshifted or redshifted emission (relative to the systemic), accompanied by clear evidence of a spatio-kinematic component separate from the galactic disc of the host galaxy. Owing to limitations in spatial resolution and sensitivity, however, candidate molecular outflows detected in emission at high redshifts are more commonly inferred solely from asymmetric broad

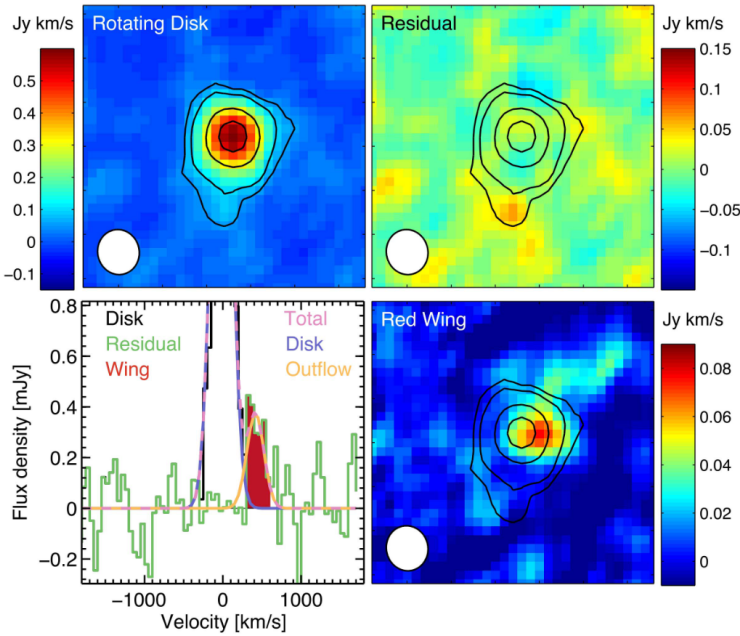


**Figure 1.15:** A spatially resolved outflow seen in CO emission from cool molecular gas. Figure adapted from [Herrera-Camus et al. \(2019\)](#).

line wings in spatially-integrated spectra, an example of which shown in Figure 1.16 for a quasar at  $z = 3.9$ . Without any spatially-resolved maps allowing the separation of the candidate outflow from the rotating disc, however, there is even less certainty that such signatures trace gas escaping from the host galaxy. For instance, extreme line wings could be due to recent or ongoing mergers, inflows, or simply contamination of the spectra by foreground emission.

Due to the difficulties in detecting molecular outflows in the early universe using emission lines, observers have turned instead to absorption lines, the most often used being the OH 119  $\mu\text{m}$  doublet. The advantage of using absorption lines rather than emission is that all that is needed is a sufficiently bright continuum source; in the case of spectral lines at infrared wavelengths (e.g. the OH 119  $\mu\text{m}$  doublet), this can be provided by thermal dust emission. [Spilker et al. \(2018\)](#) and [Spilker et al. \(2020b\)](#) observed the OH 119  $\mu\text{m}$  doublet in 11 dusty star-forming galaxies using ALMA, detecting OH absorption against the dust continuum in all of them. They also utilised archival observations of [C II] 158  $\mu\text{m}$  emission (5/11 sources) or CO emission (6/11 sources) that, they argue, trace only the ISM in the discs of the target galaxies (on the basis of a lack of high-velocity line wings expected of outflows). They generated spatially-integrated spectra from these observations, and compared the OH profiles in velocity space against emission from the ISM. In 8/11 sources, they reported OH absorption blueshifted beyond any ISM emission, as in the spectra shown in figure 1.17. They argue that these spectral features are a signature of gas outflowing along the line of sight towards the observer. However, as I show in Chapter 2, great care must be taken when

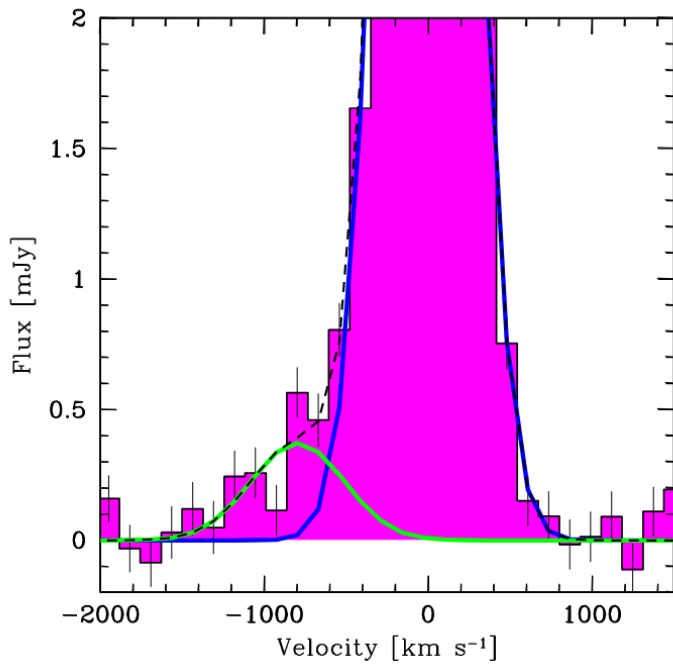


**Figure 1.16:** CO emission from a  $z = 3.9$  quasar with blueshifted line wing. Such signatures are commonly used to infer outflows in unresolved sources at high redshifts. Figure adapted from Feruglio et al. (2017).

interpreting the spatially-integrated spectra in this way, as the results can be misleading due to (i) dilution of patches of ISM emission by the process of spatial integration, (ii) wavelength-dependent spectral uncertainties due to atmospheric absorption features, and/or (iii) possible contamination by the same atmospheric features. Moreover, this method of identifying outflows suffers from the inherent drawback of being limited by the signal-to-noise ratio of the ISM emission, meaning it is impossible to know exactly its full extent in velocity space. I go on to show a more powerful method of identifying a kinematic component traced in OH separate from the galactic disc, by comparing the spatio-kinematic distributions in OH absorption and ISM emission shown in the ALMA channel maps.

## 1.5 Overview

In the following chapters, I present three studies investigating outflows and the systems that play host to them.

In Chapter 2, I examine evidence for outflows of molecular gas from dusty star-forming galaxies in the early universe. I demonstrate that spectral signatures used by previous studies to diagnose outflows in these objects are inherently unreliable, and go on to establish more reliable outflow diagnostics. Using these improved diagnostics, I

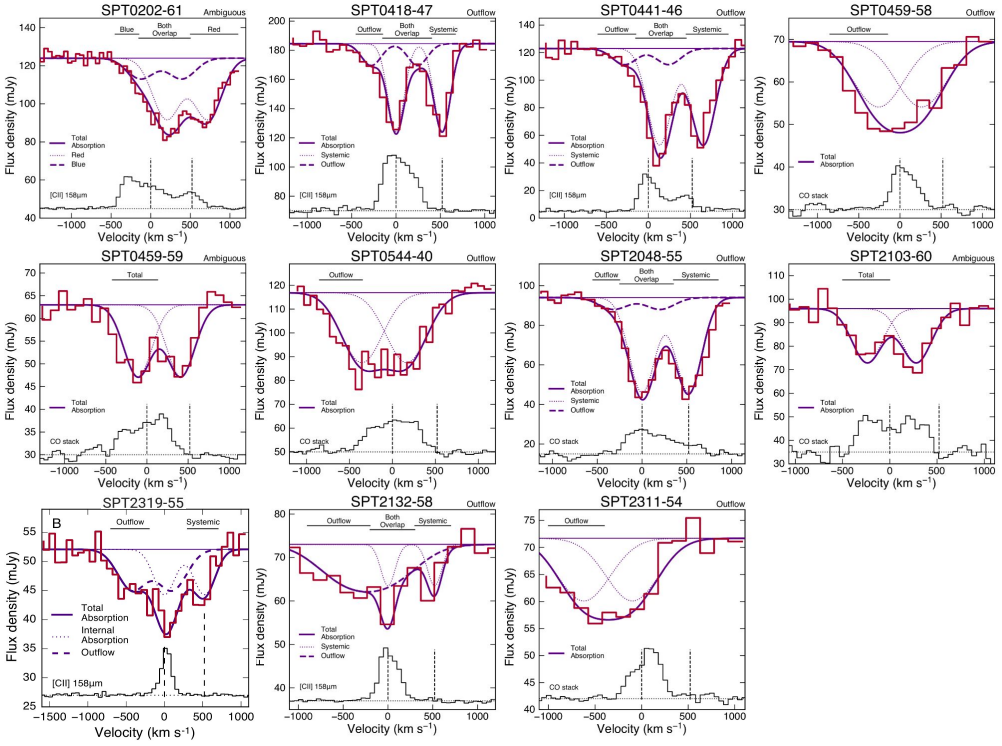


**Figure 1.17:** OH absorption spectra of 11 DSFGs compared against C II or CO emission, which traces the ISM. Apparent OH absorption blueshifted beyond the ISM emission is used to argue for molecular outflows. Figure adapted from Spilker et al. (2018) and Spilker et al. (2020b).

show that evidence for molecular outflows is ubiquitous in dusty star-forming galaxies in the early universe. This provides direct evidence of stellar feedback depleting the reservoir of molecular gas in star-forming galaxies, thus suppressing future star formation.

In Chapter 3, I search for spectral signatures of outflows from faint gravitationally-lensed Ly $\alpha$ -emitting galaxies in the early universe. I find evidence of widespread outflows from these objects both indirectly via interpretation of the Ly $\alpha$  spectral profiles, and directly via interstellar absorption lines that are blueshifted relative to the systemic redshift of the host galaxy. That such outflows appear to be common among faint star-forming galaxies supports the contention that feedback is more effective at suppressing star formation in low-mass galaxies. I also demonstrate that sources with harder ionizing spectra are associated with slower, less massive outflows (i.e. lower mass outflow rates), and suggest that this may be due to a greater abundance of ionizing photons in low-mass, low-metallicity galaxies. Finally, I investigate whether outflow parameters may be reliably inferred by fitting homogeneous expanding shell radiative transfer models to the observed Ly $\alpha$  spectral profiles. The results suggest that such simple models lack crucial elements required to accurately capture how real Ly $\alpha$  profiles are shaped by outflow properties.

Chapter 4 presents an in-depth analysis of the star formation history of one of the most highly magnified lensed Ly $\alpha$ -emitting galaxies from Chapter 3 using images from the Hubble Space Telescope and James Webb Space Telescope. I uncover evidence of multiple stellar populations in this object, a finding that is unprecedented given its faint and compact nature. I consider possible evolutionary scenarios including (i) accretion of pristine gas from the IGM to fuel the second burst of star formation and (ii) expulsion of metal enriched gas as an outflow by the first burst of stars and subsequent re-accretion from the CGM to form the second burst. In light of the metal-enriched nature of the second generation of stars, I argue that the latter of these scenarios is more plausible, raising the possibility that outflows from low-mass galaxies need not entirely quench future star formation.



## Chapter 2

# Candidate Molecular Outflows in the Early Universe

The following chapter is drawn from the journal article "On the Evidence for Molecular Outflows in High-redshift Dusty Star-forming Galaxies" by James Nianias, Jeremy Lim, and Michael Yeung, published February 23, 2024 in *The Astrophysical Journal*. I prepared the manuscript including all writing and figures, and performed all the data analysis herein. Initial discovery of the strong atmospheric absorption feature coinciding with the purported spectral outflow signature in SPT0418-47 was made by M.Y.. There are some minor formatting and spelling changes relative to the final published version, as well as some additional clarifying remarks and an extended discussion section.

## Abstract

Galactic-scale outflows of molecular gas from star-forming galaxies constitute the most direct evidence for regulation of star formation. In the early universe ( $z > 4$ ), such outflows have recently been inferred from gravitationally-lensed dusty star-forming galaxies (DSFGs) based on ubiquitous detections of OH absorption extending to more blueshifted velocities than [C II] or CO emission in spatially-integrated spectra. Because these lines are redshifted to sub-mm wavelengths, such measurements require careful corrections for atmospheric absorption lines, and a proper accounting of sometimes large variations in measurement uncertainties over these lines. Taking these factors into consideration, we re-analyze OH and [C II] data taken with ALMA for the five sources where such data is available, of which four were categorised as exhibiting outflows. Based on their spatially-integrated spectra alone, we find statistically significant ( $\geq 3\sigma$ ) OH absorption more blueshifted than [C II] emission in only one source. By contrast, searching channel maps for signals diluted below the detection threshold in spatially-integrated spectra, we find evidence for a separate kinematic component in OH absorption in all five sources in the form of: (i) more blueshifted OH absorption than [C II] emission and/or (ii) a component in OH absorption exhibiting a different spatio-kinematic pattern than [C II] emission, the latter presumably tracing gas in a rotating disc. Providing a more complete and accurate assessment of molecular outflows in gravitationally-lensed DSFGs, we suggest methods to better assess the precision of corrections for atmospheric absorption and to more accurately measure the source continuum in future observations.

### 2.1 Introduction

Feedback processes related to star formation, active galactic nuclei, or both, are thought to have regulated the formation of stars in galaxies since early times. Without feedback, cosmological models predict galaxies to have much larger stellar masses than are seen in the present-day universe (e.g., see Kereš et al. 2009 and references therein). The most easily visible manifestation of such feedback is galactic-scale outflows, a prominent example of which can be seen in the nearby starburst galaxy M82. This outflow is detectable in X-ray, H $\alpha$ , and CO, tracing ionised, atomic, and molecular gas, along with

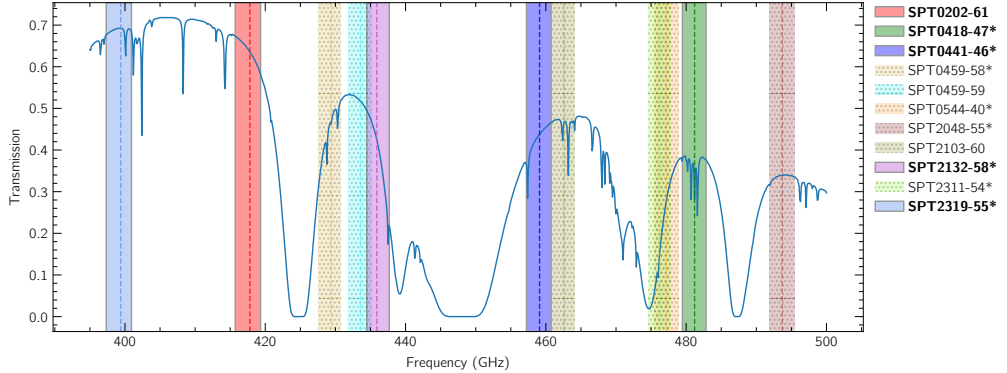


**Figure 2.1:** OH-containing bandpasses of the sources observed in S18 and S20 (coloured bands) overlaid on a representative atmospheric transmission model (blue curve) produced in CASA (McMullin et al., 2007). Sources with high-resolution [C II] observations are indicated in bold, while those in which S18 or S20 detect blueshifted OH absorption are indicated with asterisks. Dashed vertical lines indicate the frequency of the higher-frequency OH line at the respective source redshift. The broad absorption bands in the transmission model are produced by H<sub>2</sub>O, while the narrow lines are due to O<sub>3</sub>. The bandpasses of SPT0418-47 (green band) and SPT2319-55 (light blue band) contain O<sub>3</sub> atmospheric absorption lines, while the atmospheric transmission drops steeply towards the high-frequency (low-velocity) edge of the bandpass of SPT2132-58 (purple band).

infrared emission tracing dust, all streaming outwards perpendicular to the disc. Since young galaxies can exhibit more vigorous star formation, outflows at high redshift may be even stronger (Sugahara et al., 2019); furthermore, galaxies have lower masses in the early universe, so both gas and dust can escape more easily from the galaxy owing to radiation pressure and stellar winds from star-forming regions.

Unlike in nearby galaxies, galactic outflows at high redshifts are generally not spatially resolved and are instead inferred from emission and/or absorption line profiles. High-redshift star-forming galaxies have been shown to exhibit spectral signatures of ubiquitous ionized/atomic outflows: Ly $\alpha$  emission lines with peaks redshifted relative to the systemic velocity of the host galaxy, sometimes accompanied by weaker blueshifted peaks, are interpreted in terms of scattering of Ly $\alpha$  through partially- or fully-ionized outflows (see, e.g., Jones et al. 2012, review by Erb 2015), though radiative transfer models are as yet unable to reproduce the observed distribution of different Ly $\alpha$  profiles (Gurung-López et al., 2022). A more unambiguous indicator of outflows is the presence of blueshifted metal absorption lines arising from partially neutral material outflowing from starburst regions towards the observer (see Steidel et al., 2010), though such features are difficult to detect when the stellar continuum is weak.

The apparent abundance of ionized/atomic outflows in star-forming galaxies at high redshifts naturally raises the question of whether molecular gas also is driven out. Molecular gas is of particular interest because it comprises the fuel for star formation, making outflows of molecular gas the most direct signature for feedback-regulated star formation in star-forming galaxies. At the present time, however, high-redshift

molecular outflows seen in line emission, as inferred from broad CO line wings, have only been reported in a small number of objects – around ten – all thought to be AGN-driven (e.g., review by Veilleux et al. 2020). Given the limited success in observing high-redshift molecular outflows in line emission, observers have resorted to searching for outflows in line absorption, since all that is required is a sufficiently bright background continuum source such as dust emission. Spilker et al. (2018) and Spilker et al. (2020b) (hereafter S18 and S20, respectively) took advantage of a sample of gravitationally-lensed galaxies with particularly bright dust continua – dusty star-forming galaxies or DSFGs – to search for spectral signatures of outflowing molecular gas traced in OH 119  $\mu\text{m}$  doublet absorption. They observed eleven of these galaxies with the Atacama Large Millimeter/submillimeter Array (ALMA) in Band 8 (covering 385 – 500 GHz, corresponding to a redshift range of  $z \sim 4 - 5.7$  in the OH 119  $\mu\text{m}$  doublet), and compared the resulting OH absorption spectra with archival observations of either [C II] or CO emission from the same objects. In eight of the eleven sources observed, they detect OH absorption blueshifted to velocities greater than any detectable [C II] or CO emission. Interpreting the [C II] and CO emission as tracing gas contained in the disc of the target galaxies, they argue that the blueshifted OH absorption traces outflowing gas. Moreover, they find no strong evidence of AGN-related emission based on mid-IR photometry, suggesting that these outflows may be driven by feedback from star-formation.

As was pointed out in both S18 and S20, observations in the sub-mm are complicated by both broad and narrow atmospheric absorption features. These features can be seen in a representative atmospheric transmission curve for ALMA band 8, the band in which all the OH observations in S18 and S20 were made, as plotted in Figure 2.1. The coloured bands in this figure indicate the bandpasses of each target from S18 and S20. As can be seen, some of these bandpasses coincide with large changes in atmospheric transmission, either in the form of narrow lines due to O<sub>3</sub> (e.g., SPT2319-55 and SPT0418-47) or broad features across the bandpass due to H<sub>2</sub>O absorption (e.g., SPT2132-58). The strong and sometimes rapid changes in atmospheric absorption with observing frequency, as well as variations in time owing to changes in atmospheric conditions and/or source elevation, have two important consequences that observers must consider. Firstly, although corrections are made to such changes through measurements of atmospheric opacity towards each object observed (see Section 2.2.1), it is still necessary to assess the precision of these corrections to ensure that no residual atmospheric features remain. Secondly, varying atmospheric transmission with frequency leads to a varying noise level across the target spectra. While this effect is mentioned in S18, it is crucial to explicitly compute measurement uncertainties in each channel separately so as to assess the statistical significance of any spectral features.

Here, we re-analyse all sources in S18 and S20 for which high-resolution [C II] 158  $\mu\text{m}$  observations have been made with ALMA – five out of eleven in total, as listed in Table 2.1. The remaining sources (all from S20) only have available observations in CO at angular resolutions far too low to permit the checks described above, and are

therefore excluded from our study. To address the concerns raised above, we check the precision of the overall bandpass calibration to define the minimum level whereby OH absorption features can be considered genuine. In so doing, we find that in all but one case, the bandpass is corrected to a sufficiently high precision that any residual atmospheric effects must be well below the noise level of the target spectra. We also determine the measurement uncertainty in each spectral channel, necessary to assess the statistical significance of any putative OH absorption. As a first step in searching for outflows, we compare spatially-integrated OH and [C II] spectra in exactly the same manner as S18 and S20 to search for OH absorption blueshifted beyond detectable [C II] emission<sup>1</sup>. Of the five sources included in our study, S18 and S20 find such evidence for outflows in four; by contrast, with a proper accounting of measurement uncertainties in different spectral channels, our analysis reveals just one source in which this spectral signature is statistically significant.

Owing to gravitational lensing, all of the sources studied are strongly magnified into Einstein rings, allowing other diagnostics to be used for assessing outflows. Thus, secondly, to guard against the possibility of localised OH absorption and/or [C II] emission being diluted below the detection threshold in the spatially-integrated spectra, we examine maps in individual spectral channels (channel maps) for each source. We find [C II] emission extending to more blueshifted velocities than is detectable in the spatially-integrated spectra in two sources, highlighting a major potential pitfall in relying on spatially-integrated spectra alone to diagnose outflows. On the other hand, we find OH absorption extending to more blueshifted velocities than [C II] emission not just in the source mentioned above showing such behavior in its spatially-integrated spectrum, but also in two further sources where the corresponding features are not detectable in their spatially-integrated spectra. Finally, we search the channel maps for a component in OH absorption exhibiting a different spatio-kinematic pattern than the [C II] emission, thus providing direct evidence for a separate kinematic component possibly tracing an outflow, finding three such examples.

In Section 2.2, we describe our reduction of the data taken by ALMA, focusing in particular on how well the effects of atmospheric absorption are accounted for in the calibration process. We stress that we follow the same steps in the data reduction as S18 and S20, and obtain the same results within random noise fluctuations – except now explicitly quantifying the accuracy to which corrections in atmospheric absorption have been made in the target sources as well as quantifying the level of noise fluctuations in each spectral channel. In Section 2.3, we compare the spatially-integrated [C II] and OH spectra of each source as well as the spatio-kinematic structure of [C II] and OH in maps of individual spectral channels. In Section 2.4, we summarise the complete suite of evidence for outflows in each source. We then discuss ramifications for the mass outflow rates as calculated by Spilker et al. (2020a). We end our discussion with

---

<sup>1</sup>The only difference in our approach is that we (i) bin the OH and [C II] spectra to the same velocity grid – unlike S18 and S20 where the [C II] has much finer velocity bins than the OH – and (ii) explicitly compute the statistical significance of the outflow signatures, which is not done in S18 and S20

**Table 2.1:** Sources

Source	z	int. time (min)	
		OH	[C II]
SPT0202-61	5.0180	43	54
SPT0418-47	4.2248	87	19
SPT0441-46	4.4770	28	29
SPT2132-58	4.7677	17	25
SPT2319-55	5.2943	30	21

suggestions to mitigate the difficulties in detecting weak astronomical absorption lines in the presence of strong atmospheric absorption lines in ALMA observations. Finally, in Section 2.5, we summarise our work and offer our thoughts on how future searches of OH outflows from high- $z$  galaxies ought to be conducted.

## 2.2 Archival Observations and Data Reduction

We obtained data for the same OH 119  $\mu\text{m}$  observations presented in S18 and S20, along with data from ancillary observations covering the [C II] 158  $\mu\text{m}$  line of each target, from the ALMA archive. The OH observations were made with one sideband containing two partially-overlapping spectral windows covering the OH lines at the source redshift, and an alternate sideband containing two partially-overlapping spectral windows covering only the dust continuum. Further details of the OH observations can be found in S18 and S20. Similarly, the [C II] observations utilised two spectral windows to cover the [C II] line at the source redshift in one sideband, and two spectral windows to cover the dust continuum in the other sideband. In both the OH and [C II] observations, each spectral window is configured at its maximal possible bandwidth of 1.875 GHz. Table 2.1 lists the redshifts and integration times of the observations in OH and [C II] for each source.

### 2.2.1 Calibration

The ALMA Science Archive provides uncalibrated visibilities along with scripts that allow users to calibrate the visibilities using the corresponding pipeline for the ALMA cycle in which the observations were made. We calibrated each visibility set in the same manner as reported in S18 and S20, using the calibration script either executed by us (for SPT0418-47 and SPT2132-58) or by the East Asia ALMA helpdesk (for the remaining sources<sup>2</sup>). The only exceptions are the OH data for SPT0441-46 and [C II] data for SPT2132-58, which we re-calibrated manually, though excluding the data flagged

<sup>2</sup>Although we ran the calibration pipelines ourselves for all the sources, owing to a number of technical issues, we had to revert to the ALMA helpdesk for calibrating the data for some of these sources.

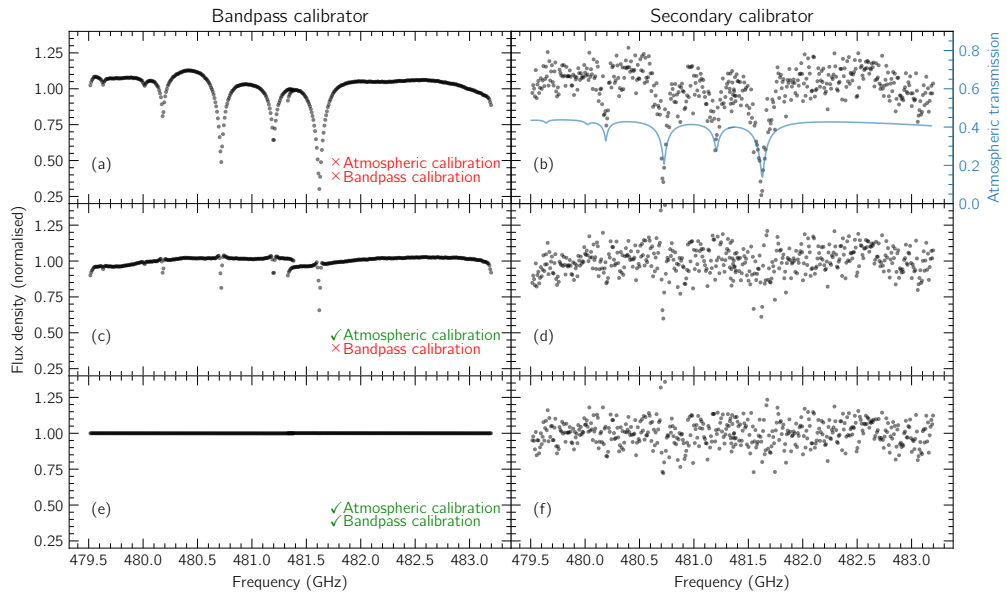


**Figure 2.2:** (a)-(b): Spectrum of the bandpass calibrator and secondary (phase) calibrator for SPT0418-47 with neither atmospheric nor instrumental bandpass calibration applied. Each spectrum clearly shows narrow absorption lines due to atmospheric O<sub>3</sub>, closely matching the atmospheric transmission model in (b) (blue curve). (c)-(d): the same spectra after atmospheric calibration but before instrumental bandpass calibration. Both spectra clearly show residual features around the O<sub>3</sub> lines due to the lower spectral resolution of the atmospheric opacity measurements. (e)-(f): the same spectra after both atmospheric and instrumental bandpass calibration. Since the instrumental bandpass correction is derived from this spectrum, the bandpass calibrator spectrum in panel (e) is almost perfectly flat; however, the secondary calibrator spectrum in panel (f) shows enhanced scatter around the O<sub>3</sub> lines due to higher thermal noise, residual atmospheric features, or both.

in the initial automatic pipeline as for the other sources<sup>3</sup>. Following subsequent self-calibration of the visibilities (described in Section 2.2.2), the dust continuum maps that we produced for all sources have morphologies and signal-to-noise ratios in close agreement with those reported in S18 and S20; furthermore, the spatially-integrated OH spectra also are similar to those presented in S18 and S20 within random noise fluctuations.

Prior to calibration, the atmospheric absorption features shown in Figure 2.1 are imprinted on the spectra of the target as well as the calibrators. These features are clearly visible in the uncalibrated spectra of the bandpass and secondary calibrators (the purposes of these calibrators are described below), examples of which are shown in Figure 2.2(a) for the primary calibrator and Figure 2.2(b) for the secondary calibrator used in the observations of SPT0418-47. ALMA corrects for variable atmospheric transmission by measuring the signal strength emitted by the atmosphere, expressed as the atmospheric temperature  $T_{atm}$ , which is then used to estimate atmospheric opacity and hence also transmission (for details see He et al. 2022). By making this measurement as a function of both frequency (at a resolution of 16 MHz) and time (immediately before an observation of a calibrator or the target object), the calibration pipeline corrects for changes in the atmospheric transmission due to the changing elevation of the target as well as varying weather conditions. Because measurements of  $T_{atm}$  are obtained at lower spectral resolution than the calibrators and target spectra, however, residual atmospheric features remain even after the atmospheric calibration is applied. Such residuals are most readily apparent for relatively narrow atmospheric absorption lines that are not spectrally resolved in the  $T_{atm}$  measurements, as can be seen in Figure 2.2(c) for the bandpass calibrator and Figure 2.2(d) for the secondary calibrator after atmospheric calibration is applied.

The remaining gradual variation with frequency bracketed by roll-offs towards the edges of each spectral window, most clearly apparent in Figure 2.2(c) and also present in Figure 2.2(d), is due to the instrumental response. To correct for this, an observation of a bright continuum source (referred to as the bandpass calibrator, which has no known spectral lines) is conducted to derive corrections for the instrumental spectral response; as there are residual atmospheric features in the spectrum of the bandpass calibrator, these features are also removed in the bandpass calibration. Figure 2.2(e) shows the spectrum of the bandpass calibrator after bandpass calibration is applied: as expected, it is perfectly flat to within the noise level. On the other hand, the bandpass calibration does not necessarily remove (and may even exacerbate) the residual atmospheric features in the spectrum of the secondary calibrator and target, which are often observed at different (lower) elevations than the bandpass calibrator and therefore suffer different (larger) degrees of atmospheric absorption. Figure 2.2(f) shows the spectrum of the secondary calibrator after bandpass calibration is applied, in which channels coinciding

<sup>3</sup>Our re-calibration of the OH observations of SPT0441-46 was motivated by concerns about the high noise level found in the images made with the original calibration; our re-calibrated data shows reduction in sidelobe levels. For SPT2132-58, an issue in the original ALMA calibration script manifested as a discontinuous jump in noise level between two adjacent spectral windows.

with the narrow atmospheric O<sub>3</sub> lines can be seen to exhibit enhanced scatter owing to either residual atmospheric features or higher thermal noise in channels with higher atmospheric opacity (or a combination thereof). This check highlights the importance of determining the precision of the combined atmospheric and bandpass calibration to ensure that any residual atmospheric features are sufficiently small that they cannot significantly affect the target spectra.

The final step in the calibration is to derive temporal variations in amplitude and phase induced by both the atmosphere and the telescope instrumentation on the target object. Such corrections are derived from each scan of the secondary calibrator, and interpolated to the times of the target scans so as to be applied to the target.

Finally, the measurement uncertainty can change quickly across the spectrum of a given object owing to rapid changes in atmospheric transmission with frequency. Such rapid changes in the measurement uncertainty need to be recognised when assessing the statistical significance of any purported spectral line features, especially when the latter coincide with narrow and deep atmospheric absorption lines (e.g., as in the cases of SPT0418-47 and SPT2319-55 as described in Section 2.3.1).

### 2.2.2 Self-calibration

Owing to their different sky positions and changing weather conditions, the amplitude and phase corrections as interpolated from the secondary calibrator may leave residual amplitude and phase errors in the calibrated data for the target<sup>4</sup>. Such residual errors can be reduced using self-calibration, which in the cases here utilises a high-signal-to-noise continuum map<sup>5</sup> of the target itself to determine any remaining amplitude and phase corrections. In nearly all of the observations, the spectral windows containing the OH or [C II] lines have wide enough frequency coverage that they also permit measurements of the continuum adjacent to the respective line profiles. We therefore selected frequency ranges free from any OH absorption or [C II] emission, using the spectra shown in S18 and S20 as a guide, and combined these with the continuum-only sidebands when making continuum images. The sole exception is the OH observations of SPT2132-58, for which S20 infer OH absorption to cover nearly the entire bandpass, and which has no useable data in the continuum sidebands due to low atmospheric transmission. In this case, following S20, we used all channels in both OH-containing spectral windows to make the continuum image; as we will show in Section 2.3, most of these channels do not in fact contain statistically significant OH absorption. We then CLEANed<sup>6</sup> the resulting continuum maps to three times the thermal noise level<sup>7</sup> – not

<sup>4</sup>Secondary calibrators were observed at  $\sim$  10 min intervals, and thus are unable to correct for atmospheric changes on time scales shorter than this.

<sup>5</sup>The continuum images have peak signal-to-noise ratios between 70 and  $>$  300, making them suitable for self-calibration.

<sup>6</sup>The images generated are convolved with the point spread function (PSF) of the antenna array, known as the dirty beam. CLEANing deconvolves the dirty beam from the image and replaces it with a clean beam, a Gaussian ellipsoid fitted to the central lobe of the PSF.

<sup>7</sup>We determined the thermal noise level by making maps with large shifts in phase center relative to the source positions.

so deep as to pick up noise peaks or artefacts – for self-calibration. We then used these CLEAN continuum maps to perform phase-only self-calibration of the target visibilities, which resulted in smaller residual phase errors and hence significantly improved signal-to-noise in the final CLEAN continuum maps. Like S18 and S20, we did not perform any self-calibration in amplitude, as deriving robust amplitude corrections would require images having much higher signal-to-noise ratios.

### 2.2.3 Channel maps and integrated spectra

The channel maps used in our study as presented in Section 2.3.2 were generated from the self-calibrated visibilities. For each source, we CLEANed the channel maps to 1.5 times the thermal noise level as measured in the channel map corresponding to the central velocity of the higher-frequency (lower-velocity) component of the OH doublet. As a check on the quality of our CLEAN maps, we compute the root-mean-square (rms) variation over an annulus surrounding the source in each corresponding channel map, finding it to be only  $\sim 10\%$  to 30% higher than the thermal noise level. Table 2.2 lists the OH channel widths used for the individual channel maps of each source, chosen to be approximately the same as those in S18 and S20. To make a proper comparison of the OH and [C II] spectral profiles, we used the same widths when making [C II] channel maps for each source. To generate continuum-subtracted [C II] channel maps, like in S18 and S20, we performed continuum subtraction on the [C II] visibilities in the uv-plane, fitting the continuum level using the same channels in the [C II]-containing spectral windows as were used to make continuum maps, i.e., channels well away from any emission. We performed continuum subtraction in the same manner on the OH visibilities to make continuum-subtracted OH maps; when presenting the spatially-integrated spectra in OH, however, we retain the continuum to allow the depth in OH absorption relative to the continuum to be computed. By comparing the OH absorption depth to the precision in atmospheric and bandpass calibration for a particular source, we are able to assess whether this absorption genuinely arises in the source. Finally, we convolved the OH channel maps, continuum-subtracted [C II] channel maps, and dust continuum maps of each target source to the smallest possible common angular resolution (synthesised beam), which is listed in Table 2.2 for each object. After convolution, the final beam sizes are only slightly larger than the beam sizes reported in S18 and S20 for the OH observations.

As OH absorption can only arise from sightlines towards the dust continuum, we extracted spatially-integrated OH and [C II] spectra for each source by integrating over regions where continuum is detected above  $3\sigma$  following the same procedure as used in S18 and S20. To determine the  $1\sigma$  uncertainties in individual channels of the integrated OH or [C II] spectra, we use the ESSENCE software package (Tsukui et al., 2023). ESSENCE derives uncertainties in spatially-integrated flux density using the noise autocorrelation function, as measured from each channel map with the target source masked out. Computing the uncertainties in this manner accounts for the spatial correlation in the channel maps induced by both the CLEAN (synthesised) beam as well as any residual

amplitude and phase errors in the calibration<sup>8</sup>. The spatially-integrated OH and [C II] spectra along with the varying  $1\sigma$  uncertainties in each channel are shown in panels (c) and (d), respectively, for each target source in Figure 2.3. As can be seen by comparing the OH spectra with those of the un-corrected bandpass calibrators in panel (a) for each source in Figure 2.3, the noise in each channel of the OH spectra depends on the atmospheric transmission, such that the noise level is higher where the atmospheric transmission is lower – and can therefore vary considerably across the OH line profile (as is the case also in [C II] for the same reasons).

Quantifying the level of line absorption requires knowledge of the continuum level. To estimate the continuum level and its uncertainty in the spatially-integrated OH spectrum of all the target sources apart from SPT2132-58, we used the same channels in the OH-containing spectral windows that were used to generate the clean continuum map, i.e., channels well away from any absorption. For the spatially-integrated OH spectrum of SPT2132-58, where the continuum maps were made using the full OH-containing bandpass, we estimated the continuum level using the channels at the low-frequency (i.e. high-velocity) end of the bandpass. These channels are absorption-free according to the continuum estimate provided in S20. We show the continuum levels by the dashed grey lines and their  $\pm 1\sigma$  uncertainties by the horizontal grey bands in panel (c) for each source in Figure 2.3.

## 2.3 Results and Analysis

### 2.3.1 Integrated spectra

In both S18 and S20, an outflow is indicated by OH absorption extending to blueshifted velocities beyond any detectable [C II] emission in spatially-integrated spectra. Indeed, a comparison between the OH and [C II] spectra for all but one of the sources (SPT0202-61) shown in Figure 2.3 reveals systematic offsets below the continuum level at velocities lower than the lowest velocity at which [C II] is detected; furthermore, the nominal absorption depth in these channels is the same as that in S18 and S20 to within measurement uncertainties. To compute the statistical significance in the individual cases, we integrate the OH spectrum of each source over velocities bluewards of the lowest detectable [C II] velocity<sup>9</sup> until the signal-to-noise level of this putative absorption is maximised. The velocity ranges thus selected are shown by hatched blue bands in panels (c) and (d) for each source in Figure 2.3 except SPT0202-61, for which no systematic offset below zero is appreciable over the velocity range bluewards of the lowest detectable [C II] velocity. For comparison, we also show the approximate velocity ranges over which S18 and S20 report spectral signatures of OH outflows with double-headed

<sup>8</sup>The noise calculated this way is in close agreement with a commonly-used approximation whereby the uncertainty in spatially-integrated flux in each channel is taken to be the rms noise level multiplied by the square root of the number of beams within the region of integration (to within 5 – 15%, varying from source to source and channel to channel).

<sup>9</sup>That is, we sum the absorption in spectral channels with velocity less than the lowest velocity at which [C II] emission is detected at greater than  $3\sigma$  significance.

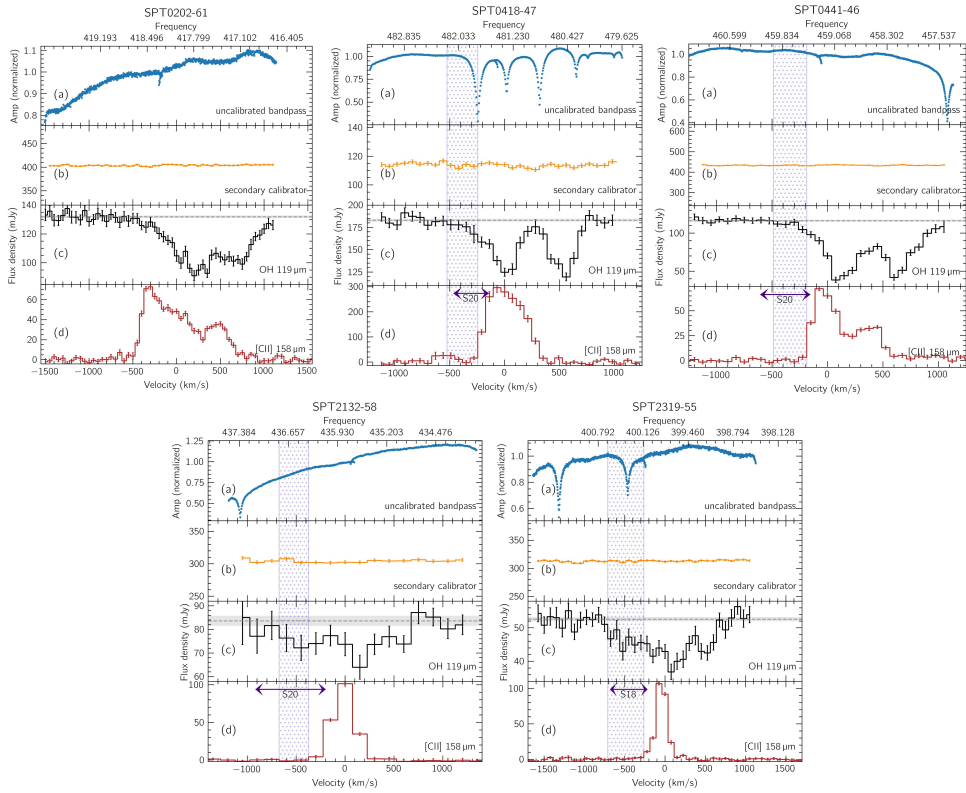


**Figure 2.3:** (a) Bandpass calibrator spectra without atmospheric or bandpass corrections, showing the dominant imprints of changing atmospheric transmission along with instrumental bandpass. (b) spectra of the secondary calibrators after calibration, showing no statistically significant residual features. (c) spatially-integrated OH spectra from each source, with grey horizontal bars indicating the  $\pm 1\sigma$  level of the continuum, blue hatched regions indicating the velocity ranges over which we obtain the highest signal-to-noise OH absorption blueshifted beyond the [C II] emission, and double-headed purple arrows indicating the approximate ranges over which S18 or S20 report blueshifted OH absorption. The  $\pm 1\sigma$  error bars of the OH spectra are shown for each channel, and can be seen to increase in size with decreasing atmospheric transmission. (d) [C II] spectra extracted over the same regions as OH, and binned to the same velocity resolution.

purple arrows<sup>10</sup>. The integrated intensity of the blueshifted OH absorption and its related measurement uncertainty, along with the velocity range over which we perform this integration, are given for each source in Table 2.2.

With a now complete accounting of the measurement uncertainties across the velocity range spanned by putative blueshifted OH absorption, we find statistically significant ( $\geq 3\sigma$ ) evidence for blueshifted absorption in the spatially-integrated spectrum of only one source, SPT2319-55, at  $6.1\sigma$ . The source that shows the next strongest putative blueshifted OH absorption is SPT0441-46, at a significance level of  $2.7\sigma$ , followed

<sup>10</sup>S18 and S20 do not claim these velocity ranges to be free of [C II] emission, but rather use them to qualitatively indicate where they believe the OH spectrum is dominated by the putative outflow kinematic component.

**Table 2.2:** Results from spatially-integrated spectra

Source	Channel width (km s <sup>-1</sup> )	BMAJ (arcsec)	BMIN (arcsec)	BPA (deg)	Outflow range (km s <sup>-1</sup> )	Absorption strength (mJy km s <sup>-1</sup> )	Correction accuracy (mJy km s <sup>-1</sup> )
SPT0202-61	50	0.48	0.42	63	N/A	N/A	N/A
SPT0418-47	70	0.55	0.35	89	[-525, -245]	2320 ± 980 (2.4 $\sigma$ )	890
SPT0441-46	75	0.35	0.26	79	[-462, -187]	1690 ± 620 (2.7 $\sigma$ )	200
SPT2132-58	150	0.43	0.36	114	[-675, -375]	2820 ± 1170 (2.2 $\sigma$ )	380
SPT2319-55	75	0.40	0.32	64	[-712, -262]	2890 ± 470 (6.1 $\sigma$ )	130

by SPT0418-47 at 2.4 $\sigma$  and SPT2132-58 at 2.2 $\sigma$ .

Before accepting as genuine any statistically significant blueshifted OH absorption, it is crucial to check that the calibration corrects the spectra to a sufficiently high precision that any residual atmospheric or bandpass features must be smaller than the depth of the putative OH absorption. To do this, we plot the spectra of the secondary calibrators as shown in panels (b) of Figure 2.3. These calibrators were observed at a similar elevation but have a higher signal-to-noise ratio in the continuum compared to the target sources. After atmospheric and bandpass calibration (described in Section 2.2.1), none of the secondary calibrator spectra exhibit statistically significant residual features. Applying the same velocity ranges given in Table 2.2 for each target to their respective secondary calibrator spectra, we compute 3 $\sigma$  upper bounds for any residual bandpass features as a fraction of the continuum; we can then be confident that the bandpasses of the target OH spectra have been corrected to within the same fraction of the continuum. The upper bounds thus derived are given in terms of integrated flux (in mJy km s<sup>-1</sup>) in Table 2.2. Comparing the strength of the putative blueshifted absorption in each source with the limits to the accuracy of atmospheric corrections, we find that in most cases the former is roughly an order of magnitude higher than the latter, indicating that imperfections in bandpass calibration cannot be responsible for the systematic offsets below the continuum in the spectra of most sources. The sole exception is SPT0418-47, for which the upper limit for residual bandpass features is comparable to the 1 $\sigma$  uncertainty in the blueshifted absorption, while the absorption strength itself is just 2.4 $\sigma$ : in this case there is a prominent atmospheric absorption line that partially overlaps with the putative blueshifted absorption. While the secondary calibrator spectrum does not show any statistically significant residual feature corresponding to this line, we cannot rule out the possibility that residual calibration errors contribute in part to the measured absorption.

### 2.3.2 Channel maps

Relying solely on the spatially-integrated spectra shown in Figure 2.3 to diagnose outflows raises two major potential pitfalls. First, the process of spatial integration may dilute signals that are confined to localised regions of the Einstein ring, whether they are small patches of OH absorption or of [C II] emission. Second, the possibility that [C II] emission extends to velocities beyond those detectable as dictated by the noise level can never be completely ruled out, making it ambiguous whether the detection of

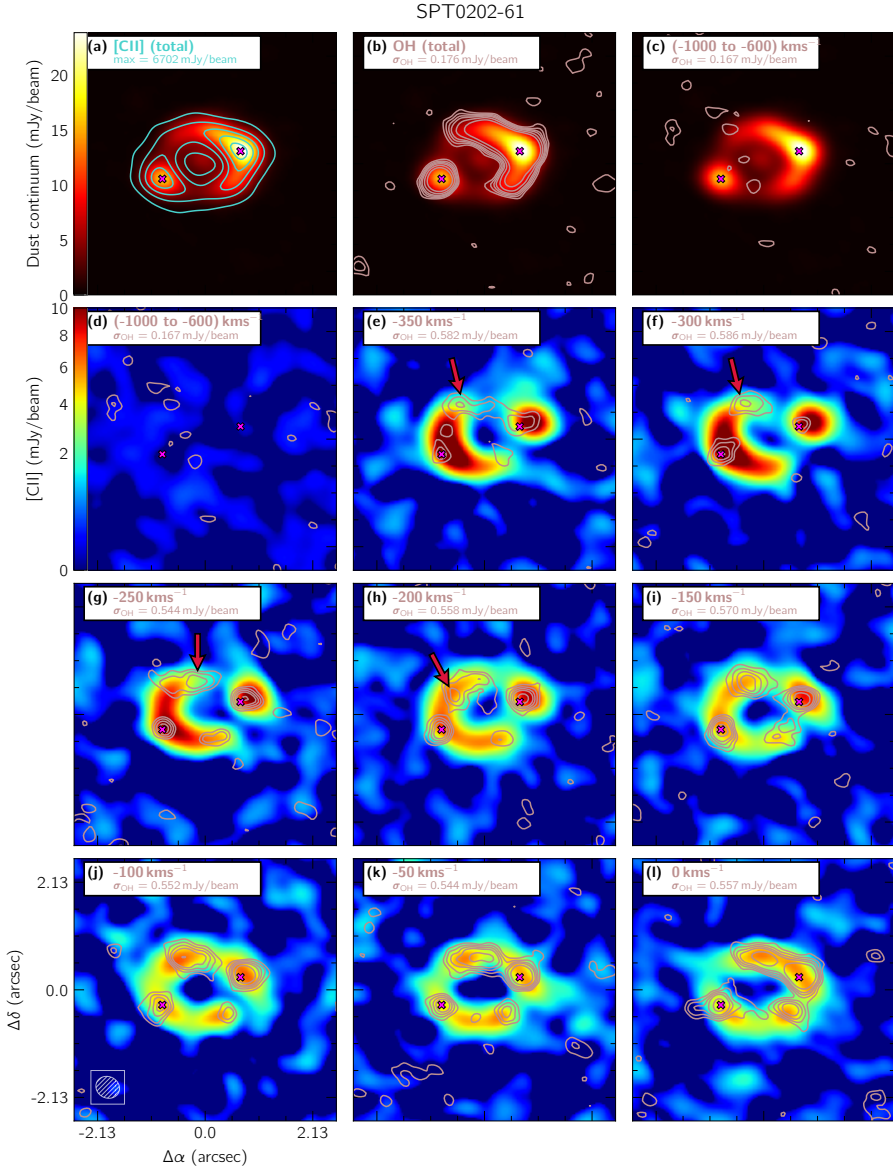


**Figure 2.4:** (a) Contours of total [C II] emission (moment 0) plotted at 10, 30, 50, 70, and 90% of the peak surface brightness (given in the box in the upper left corner) against dust continuum from SPT0202-61 (seen as an Einstein ring). (b) contours of total OH absorption (moment 0) plotted at  $2\sigma$ ,  $3\sigma$ ,  $4\sigma$ ,  $5\sigma$ ,  $7\sigma$ , and  $10\sigma$  against dust continuum ( $1\sigma$  given in the box in the upper left corner, as in the remaining panels). (c) contours of OH absorption integrated over putative outflow channels (blue hatched range in Figure 2.3) plotted at  $2\sigma$ ,  $3\sigma$ ,  $4\sigma$ ,  $5\sigma$ , and  $7\sigma$  against dust continuum. (d) the same contours as (c), now overlaid on [C II] emission integrated over the same velocity range. (e) – (l) contours of individual OH velocity channel maps with widths of  $50 \text{ km s}^{-1}$  at central velocities as indicated in each panel plotted at  $2\sigma$ ,  $3\sigma$ ,  $4\sigma$ ,  $5\sigma$ , and  $7\sigma$ , and overlaid on [C II] emission channel maps over the corresponding velocity ranges (colour). In all panels, magenta crosses mark the peaks of the dust continuum as shown in panels (a) to (c), and red arrows point to OH absorption features following a different spatio-kinematic trend to the [C II] emission, suggesting a separate kinematic component.

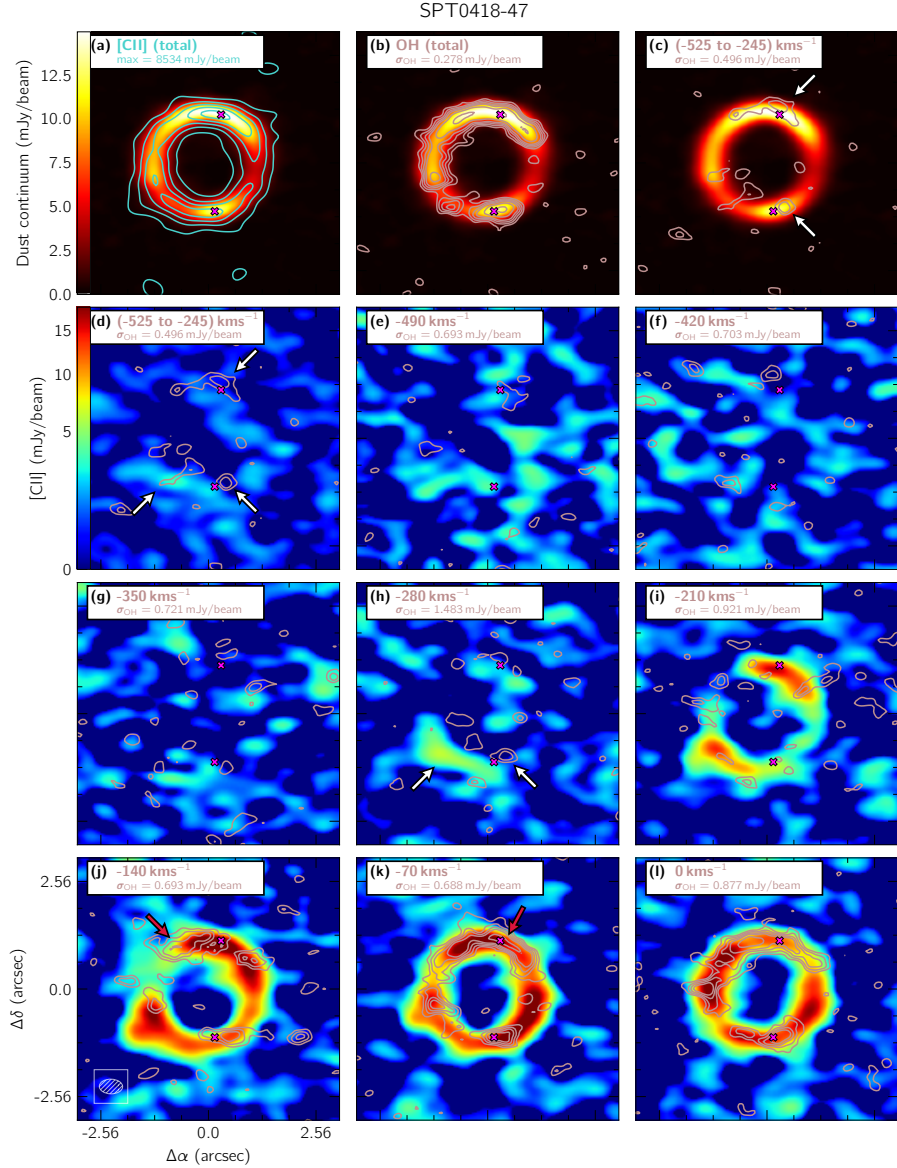


**Figure 2.5:** Same as figure 2.4, but for SPT0418-47, with channel width of  $70 \text{ km s}^{-1}$ . White arrows in panels (d) and (h) point to patches of OH absorption or [C II] emission diluted to below the detection threshold in the spatially-integrated spectrum, while red arrows in panels (j) and (k) point to OH absorption features following a different spatio-kinematic trend to the [C II] emission, suggesting a separate kinematic component.

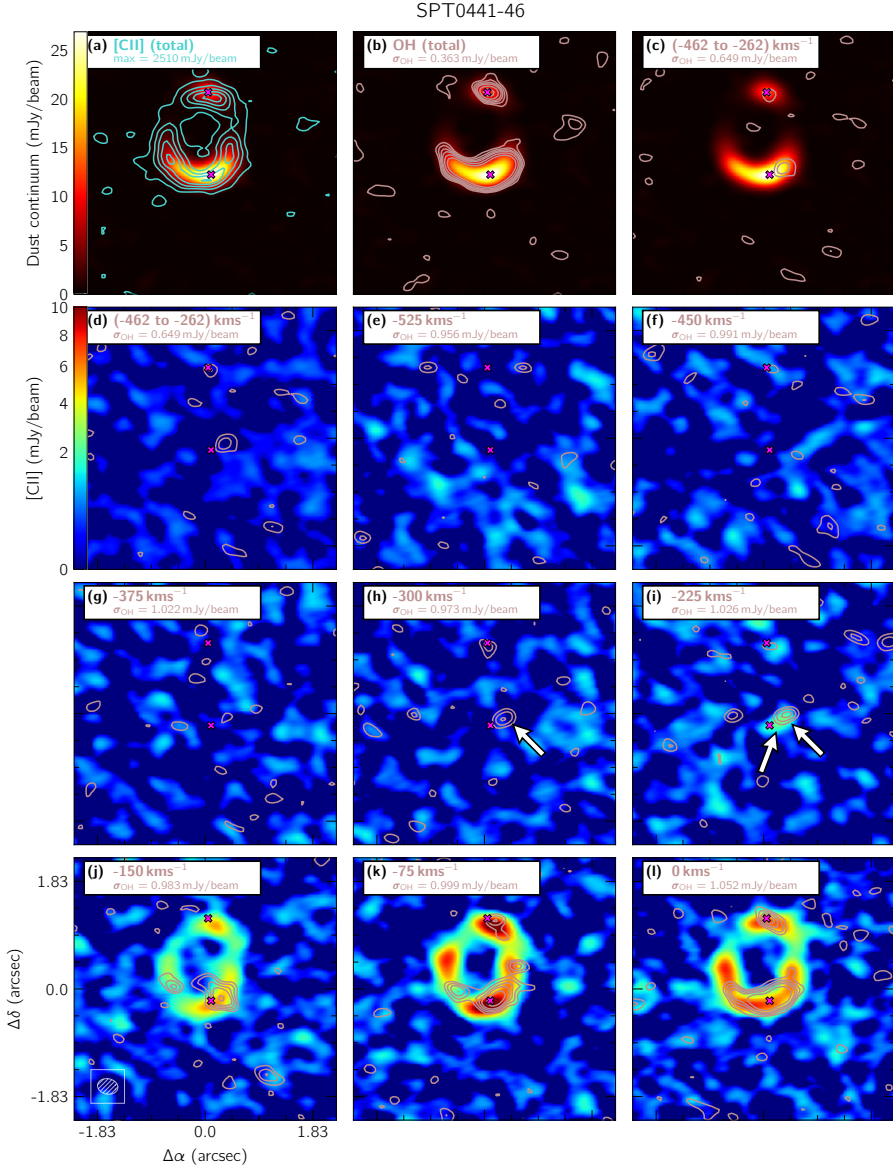


**Figure 2.6:** Same as Figure 2.4, but for SPT0441-46, with channel width of 75 km s<sup>-1</sup>. White arrows in panels (h) and (i) point to patches of OH absorption or [C II] emission diluted to below the detection threshold in the spatially-integrated spectrum, with panel (h) showing a patch of OH absorption blueshifted beyond any detectable [C II] emission.

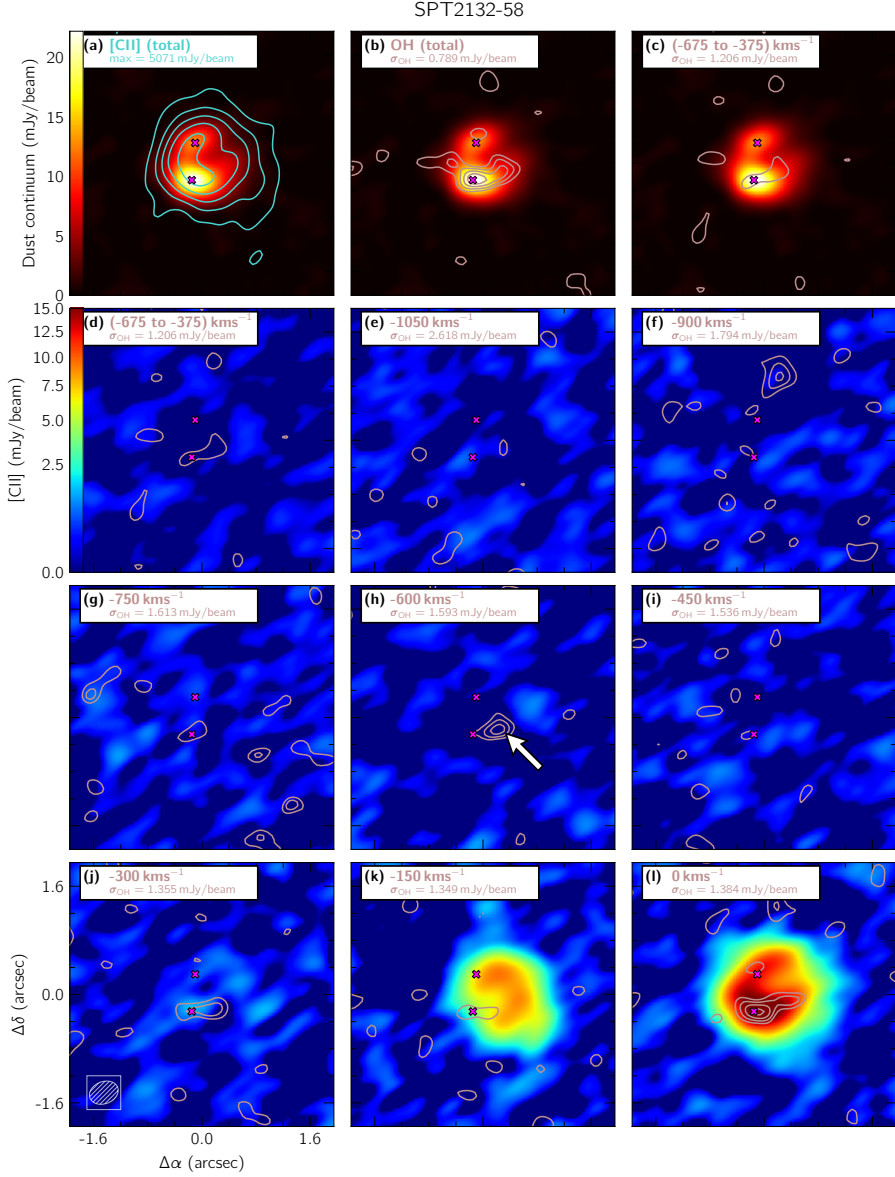


**Figure 2.7:** Same as Figure 2.4, but for SPT2132-58, with channel width of  $150 \text{ km s}^{-1}$ . The white arrow in panel (h) points to a patch of OH absorption blueshifted beyond any detectable [C II] emission, which is diluted to below the detection threshold in the spatially-integrated spectrum.

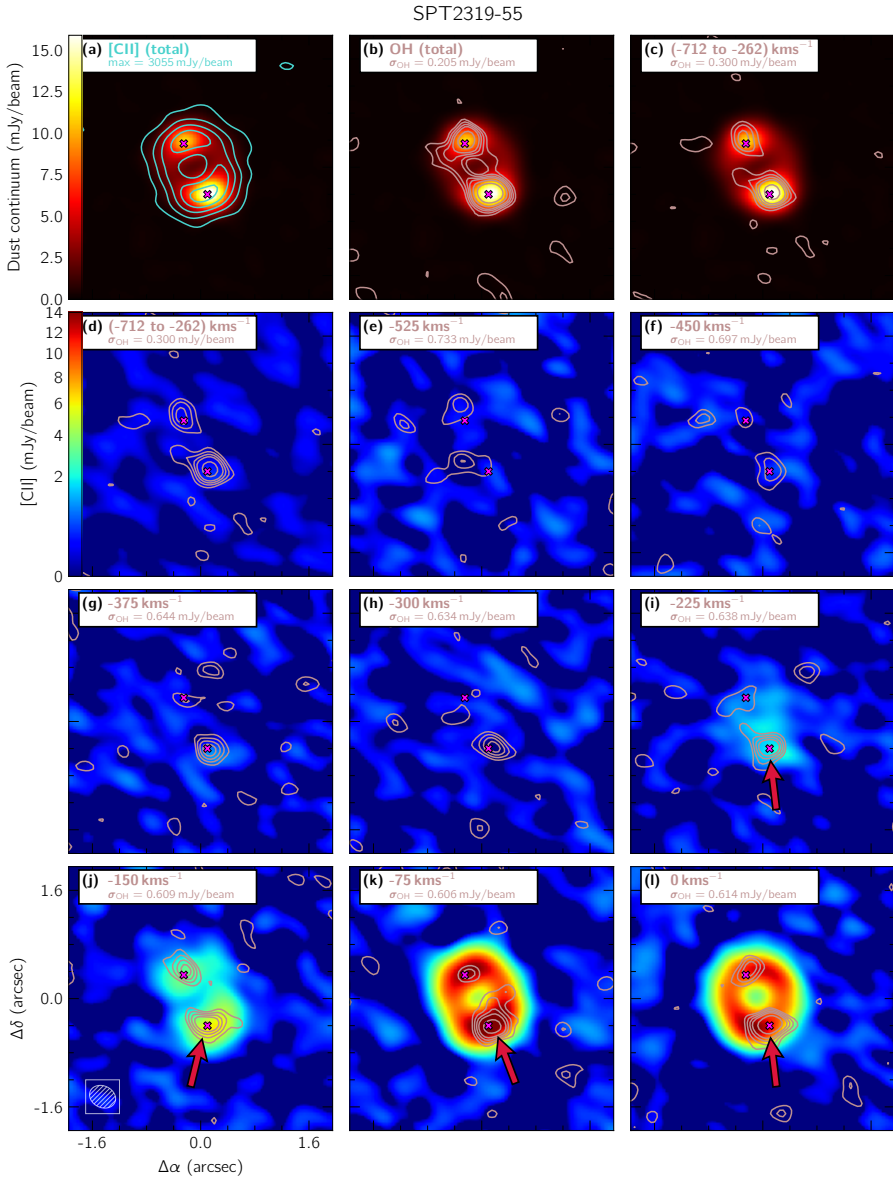


**Figure 2.8:** Same as Figure 2.4, but for SPT2319-55, with channel width of  $75 \text{ km s}^{-1}$ . Patches of blueshifted OH absorption with no accompanying [C II] emission are clearly visible in channels (h) to (e). In panels (i) to (j), red arrows indicate OH absorption features following a different spatio-kinematic trend to the [C II] emission, suggesting a separate kinematic component.

OH absorption more blueshifted than [C II] emission, alone, implies a kinematic component separate from the disc. To address both these issues, we made both OH and [C II] channel maps of each source at the same velocity resolution as the spectra shown in Figure 2.3, as well maps integrated over the full velocity ranges that we use to search for blueshifted OH (hatched blue bands in Fig. 2.3), using the continuum-subtracted OH and [C II] visibilities. These maps are shown in panels (b) to (l) of Figures 2.4 to 2.8 for each source in the same order as shown in Figure 2.3, where contours correspond to OH absorption, red background to the dust continuum, and rainbow background to [C II] emission – showing gravitationally-lensed images of each galaxy in the form of an Einstein ring.

When analysing the channel maps, it is important to take into consideration apparently statistically significant ( $\geq 4\sigma$ ) patches of OH "absorption" that are not spatially coincident with the dust continuum, as can be seen in Figures 2.5(j), 2.6(j), and 2.7(f). Such features may arise due to residual amplitude and phase errors left following calibration. We therefore only consider as genuine those absorption patches that are not only spatially-coincident with the dust continuum, but that are also deeper than any apparent absorption patches that are not spatially-coincident with the dust continuum.

White arrows in the channel maps of Figures 2.4 to 2.8 indicate selected features in either OH absorption or [C II] emission more blueshifted than are detectable in spatially-integrated spectra. The channel maps of SPT2319-55 confirm that its OH absorption extends to more blueshifted velocities than its [C II] emission in the same manner as in its spatially-integrated spectrum. Moreover, three other sources (SPT0418-47, SPT0441-46, and SPT2132-58) exhibit more blueshifted OH absorption in channel maps than is detectable in their spatially-integrated spectra, of which two (SPT0418-47 and SPT0441-46) also exhibit more blueshifted [C II] emission in a corresponding comparison. In one of these two sources (SPT0441-46), the OH absorption extends to more blueshifted velocities than the [C II] emission, whereas in the other (SPT0418-47), the OH absorption and [C II] emission extend to the same blueshifted velocities albeit at different positions within the Einstein ring. Thus, in total, three sources exhibit more blueshifted OH absorption than [C II] emission in channel maps, compared with only one (of the same three) in spatially-integrated spectra, demonstrating the importance of utilising channel maps rather than relying on spatially-integrated spectra alone to identify possible outflows.

To add to the evidence for separate kinematic components, we searched the channel maps for features in OH absorption that show a different spatio-kinematic pattern than [C II] emission. This approach has the additional advantage of permitting the identification of separate kinematic components in OH absorption even in channels with detectable [C II] emission. Before delving into this search, we first note that a one-to-one comparison between OH absorption and [C II] emission is complicated by the fact that the strength of OH absorption – unlike that of the [C II] emission – depends in part on the brightness of the background dust continuum, which can have a different surface

brightness distribution than that of the [C II] emission. Indeed, Figures 2.4(a) to 2.8(a) show such differences in some of the target sources (e.g. SPT0418-47 in Figure 2.5(a) and SPT2132-58 in Figure 2.7(a)), where cyan contours indicate the integrated [C II] emission and red background the dust continuum. Thus, we should not expect the morphology of the OH absorption to perfectly match that of the [C II] emission in individual channels even if both lines trace the same gas in the disc. In the channel maps of SPT2319-55, which shows by far the strongest and the only significant blueshifted OH absorption in spatially-integrated spectra, the OH absorption in the south of the Einstein ring indicated by the red arrows in Figures 2.8(i) to 2.8(l) can be seen to track the [C II] emission at velocities close to systemic where both move roughly counter-clockwise around the Einstein ring with decreasing velocity (between Figure 2.8(l) and 2.8(k)). At more strongly blueshifted velocities (between Figure 2.8(j) and 2.8(i)), however, the OH absorption appears to reverse this behavior and move clockwise, whereas the [C II] emission does not. This behavior suggests the presence of a separate kinematic component traced in OH absorption that moreover extends to higher blueshifted velocities than gas traced in [C II] emission contained in a rotating disc, making a strong case for a molecular outflow in SPT2319-55.

In SPT0202-61, for which [C II] emission is detectable to even higher blueshifted velocities than OH absorption in both spatially-integrated spectra and channel maps, the [C II] emission at the north of the Einstein Ring as seen in the channel maps of Figure 2.4 moves counter-clockwise from panels (h) to (e). By contrast, the patch of OH absorption indicated by the red arrows moves slightly in the opposite direction, suggesting that this feature comprises a separate kinematic component. As this patch of OH absorption coincides with relatively weak dust continuum, it does not appear merely as a consequence of bright continuum.

SPT0418-47 also shows no significant OH absorption more blueshifted than any [C II] emission in either spatially-integrated spectra or channel maps. As can be seen in the channel maps for this source in Figure 2.5, the [C II] emission in the northern portion of the Einstein ring moves clockwise starting around the systemic velocity in panel (f) to more strongly blueshifted velocities in panels (e) and (d). By contrast, the peak of the OH absorption – indicated by red arrows – moves in the opposite direction, again indicating the presence of a separate kinematic component.

## 2.4 Discussion

### 2.4.1 Outflow inferences

After determining the precision of corrections for atmospheric absorption as well as explicitly quantifying the measurement uncertainty in each spectral channel, we find that only one of the five sources that we analysed (SPT2319-55) shows statistically significant ( $\geq 3\sigma$ ) evidence for OH absorption more blueshifted than [C II] emission in its spatially-integrated spectrum. These results contrast with those reported by

[S18](#) and [S20](#), who argue that four of the same five sources display OH absorption more blueshifted than [C II] emission in spatially-integrated spectra, though without explicitly quantifying the statistical significance of this absorption (see Table ?? for source-by-source breakdown). On the other hand, we find all five sources to exhibit evidence for a component in OH absorption different from that in [C II] emission in their channel maps (which were not included in the analysis of [S18](#) and [S20](#)).

An inspection of channel maps for SPT2319-55 reveals, in addition to OH absorption more blueshifted than [C II] emission detected in its spatially-integrated spectrum, a component in OH absorption having a different spatio-kinematic pattern than [C II] emission even in channels where both OH and [C II] are detected. This source shows the strongest evidence for a molecular outflow. Both SPT2132-58 and SPT0441-46 exhibit OH absorption more blueshifted than [C II] emission in channel maps that is diluted below the detection threshold in spatially-integrated spectra, thus also providing evidence for outflows. SPT0202-61 and SPT0418-47, despite not displaying significant OH absorption more blueshifted than [C II] emission in either spatially-integrated spectra or channel maps, both exhibit features in OH absorption having different spatio-kinematic patterns than [C II] emission, and therefore evidence for separate kinematic components in OH absorption plausibly associated with outflows.

In 4/5 cases, spatio-kinematic signs of outflows are present even when there is no statistically significant OH absorption more blueshifted than [C II] emission. This may reflect (i) relatively slow outflows relative to the disc rotation speed, and/or (ii) anisotropic, collimated outflows as is seen in spatially-resolved disc galaxies in the local universe (e.g. M82). In both of these cases, the inclination angle of the disc plays an important role in whether or not an outflow can be detected in spatially-integrated spectra, with smaller inclination angles enhancing the kinematic contrast between outflows and discs, as well as providing greater column density in outflowing gas in the case of collimated outflows. That SPT2319-55 shows a much stronger outflow signature in the spatially-integrated spectrum compared to the other sources while also having a relatively narrow [C II] line profile suggests that it may have a relatively small inclination angle, lending some credence to this idea (though of course a lower dynamical mass cannot be ruled out either).

## 2.4.2 Outflow properties

In [Spilker et al. \(2020a\)](#), the mass outflow rate for each object thought to host an outflow is estimated using the depth of the blueshifted OH absorption. Assuming initially the absorption to be optically thin, the OH column density is measured from the depth of the blueshifted OH absorption integrated over velocities more blueshifted than  $-200 \text{ km s}^{-1}$ . The total gas column density is then computed assuming an OH abundance based on the study of a star-forming region in our Galaxy, Sgr B2 ([Goicoechea and Cernicharo, 2002](#)). Mass outflow rates are estimated using this column density, assuming a time-averaged thin shell geometry ([Rupke et al., 2005](#)) with inner radius set equal to the

effective radius of the dust continuum estimated using source-plane reconstructions of the gravitationally-lensed images of each source. To allow for the possibility that the OH absorption is optically thick, an empirical correction factor to the mass outflow rates is then introduced, based on observations of 14 nearby quasars and ultra-luminous infrared galaxies (ULIRGs) in multiple OH transitions (with P Cygni profiles or high-velocity absorption wings) for which radiative transfer models have been made by González-Alfonso et al. (2017). Specifically, the correction factor is based on a correlation in this sample between mass-outflow rate and the "maximum" blueshifted velocity of OH (defined as the velocity above which 98% of absorption takes place).

In addition, Spilker et al. (2020a) estimate alternative mass-outflow rates based on correlations in the González-Alfonso et al. (2017) sample between mass-outflow rate and equivalent width of blueshifted OH absorption beyond  $-100 \text{ km s}^{-1}$ , as well as equivalent width of blueshifted OH absorption beyond  $-200 \text{ km s}^{-1}$  multiplied by  $L_{IR}^{1/2}$ , where  $L_{IR}$  is the total infrared luminosity corrected for gravitational lensing. Lastly, Spilker et al. (2020a) apply a dimensionality-reduction technique similar to a principal component analysis to find an empirical correlation between the measured mass-outflow rates and combinations of other parameters in the González-Alfonso et al. (2017) sample. We find the same nominal depths of putative blueshifted OH absorption as those found by S18 and S20 within measurement uncertainties. However, having now calculated the statistical significance of these absorption features, we emphasise that the putative mass-outflow rates – derived solely from the spatially-integrated spectra – must have substantially higher uncertainties than presented in Spilker et al. (2020a), in at least some cases rendering them consistent with zero.

### 2.4.3 Improving observing strategies

Our analysis highlights the attention that must be paid to atmospheric absorption features when searching at sub-mm wavelengths for spectral signatures of high- $z$  outflows traced in absorption. Observers must not only carefully check the results of the ALMA calibration pipeline to assess the accuracy at which corrections for atmospheric absorption have been carried out, but also recognize the fact that large changes in atmospheric opacity across the bandpass lead to correspondingly large changes in the thermal noise and hence measurement uncertainties across the observed spectra.

Observers who want to better verify that atmospheric absorption has been fully removed by the ALMA pipeline (improving over the test made above from the secondary calibrator) can do so by planning observations accordingly. As observations are performed in two sidebands with one placed on the spectral line of interest and the other normally used to measure the line-free continuum, the latter sideband can be placed instead on a strong atmospheric O<sub>3</sub> line. The spectral windows in this sideband will then act as a control case for the OH-containing spectral windows, and can be checked to see whether any residual features associated with the atmospheric line remain after calibration. This check, however, may not be possible in many cases owing

to restrictions on the placement of spectral windows allowed by ALMA. In such cases, the only option left is to use the spectrum of the secondary calibrator to ensure that the degree to which corrections to atmospheric absorption have been made is likely smaller than the degree of absorption seen in the source (as conducted in our work). The downside of this approach is that, in order for this test to be effective, the secondary calibrator spectrum must be observed at a significantly higher signal-to-noise ratio than the target. Therefore, a relatively large amount of observing time may need to be spent on the secondary calibrator if the closest one to the target is relatively dim.

A separate issue that further complicates the detection of low-signal-to-noise outflows is the estimation of the continuum level in the target spectra. As shown above in the case of SPT2132-58, targets with broad absorption features may have few, if any, channels to use for continuum estimation in the spectral windows covering the OH line. In this situation, the other sideband could be used to estimate the continuum level, as is the approach taken in [S18](#) and [S20](#), but such estimates are subject to additional uncertainties introduced by the uncertain spectral index of the target source as well as errors in bandpass calibration. In the unfortunate case of SPT2132-58, the atmospheric transmission in the continuum sideband (which has a fixed offset of 12 GHz with respect to the OH sideband) is very low whether it is placed at either a lower or higher frequency than the target bandpass (see Figure [2.1](#)), so no useable continuum spectrum can be produced at all given the restrictions on the ALMA correlator set-up. Furthermore, the OH-containing sideband cannot be extended to cover a higher frequency range since it is already at the maximum possible width. The only remaining solution is to observe with two different correlator set-ups, with one set-up being used to measure the continuum level and the other the OH absorption. Although doubling the observing time, there may be no other choice but to adopt this strategy in ALMA band 8 owing to deep and closely-spaced H<sub>2</sub>O atmospheric absorption lines throughout this band (progressively less severe in lower-frequency bands).

## 2.5 Summary and Conclusion

We re-analysed observations of the five DSFGs from [S18](#) and [S20](#) for which both OH 119 μm and [C II] 158 μm images are available at comparable angular resolutions with ALMA. Such observations are complicated by strong absorption lines from the Earth’s atmosphere imprinted onto the spectra of all targeted objects, leaving two effects that must be carefully assessed: (i) residual atmospheric absorption even after standard bandpass calibration procedures; and (ii) varying measurement uncertainties over the spectra owing to varying atmospheric opacity. We therefore checked the precision to which corrections for atmospheric (together with instrumental) effects in the bandpass have been made, and also computed explicitly the measurement uncertainties in each velocity channel.

Extracting spatially-integrated spectra in the same manner as [S18](#) and [S20](#), we searched for OH absorption extending to more blueshifted velocities than detectable

[C II] emission – the signature used by both S18 and S20 to identify an outflow, indicating a kinematic component different from that of the [C II] emission attributed to the galactic disc. Over the velocity range selected to maximise the depth of any putative blueshifted OH absorption, we found the bandpass to have been corrected to within  $\lesssim 0.3\sigma$  for all sources except SPT0418-47, for which the bandpass is corrected to  $\sim 1\sigma$ . Thus informed, we found only one source (SPT2319-55) to show statistically significant ( $\geq 3\sigma$ ) evidence for blueshifted OH absorption in spatially-integrated spectra – in contrast to S18 and S20, who found four of the five sources examined here to show unambiguous signatures of outflows, though without explicitly quantifying the statistical significance of the putative blueshifted OH absorption.

In spatially-integrated spectra, signals that do not span the entire source can be diluted to below detectability, whether it be in OH absorption or [C II] emission. To guard against this possibility, we made channel maps in both OH absorption and [C II] emission to find signals that are even more blueshifted than are detected in spatially-integrated spectra. Furthermore, to find additional evidence for a separate kinematic component that can possibly arise from an outflow, we searched for an OH component exhibiting a different spatio-kinematic pattern than the [C II] emission. The full results for each source are summarised below.

SPT0202-61: no OH absorption blueshifted beyond the [C II] emission in its spatially-integrated spectrum (in agreement with S20) or in channel maps; on the other hand, component in OH absorption having different spatio-kinematic pattern than [C II] emission in channel maps.

SPT0418-47: tentative ( $2.4\sigma$ ) OH absorption blueshifted beyond detectable [C II] emission in spatially-integrated spectrum (cf. Spilker et al. (2020b), who argue for unambiguous outflow based on the spectrum); over the velocity range of the tentative blueshifted OH absorption, upper limit on precision of bandpass correction corresponding to  $\sim 1\sigma$  of the measurement uncertainty, and may therefore contribute in part to this tentative absorption feature; no OH absorption blueshifted beyond the [C II] emission in channel maps, but a clear component in OH absorption having different spatio-kinematic pattern than [C II] emission.

SPT0441-46: tentative ( $2.7\sigma$ ) blueshifted OH absorption in its spatially-integrated spectrum (cf. Spilker et al. (2020b), who argue for unambiguous outflow based on the spectrum); significant OH absorption blueshifted beyond any [C II] emission in channel maps.

SPT2132-58: tentative ( $2.2\sigma$ ) blueshifted OH absorption in its spatially-integrated spectrum (cf. Spilker et al. (2020b), who argue for unambiguous outflow based on the spectrum); significant OH absorption blueshifted beyond any [C II] emission in channel maps.

SPT2319-55: highly significant ( $6.1\sigma$ ) blueshifted OH absorption its spatially-integrated spectrum (verifying the outflow claim of [Spilker et al. \(2018\)](#)), also seen in channel maps; possible component in OH absorption having different spatio-kinematic pattern than [C II] emission in channel maps.

In brief, we find evidence of separate kinematic components plausibly associated with molecular outflows in all five of the sources included in our study.

These results highlight the potential pitfalls in relying on blueshifted OH absorption in spatially-integrated spectra alone to infer the presence of candidate outflows, and the importance of utilising the full spatio-kinematic information provided by the channel maps to search for and verify candidate outflows. Deeper follow-up observations are clearly warranted for the four sources that we find to exhibit evidence for molecular outflows, which if confirmed also permit a more precise determination of their outflow properties.

Future studies should make sure – as we have – that atmospheric absorption is fully corrected for at the level of any putative outflow absorption, and that the varying noise level across spectral channels is properly computed. In addition, the continuum level should be better measured where possible in those sources where the putative OH absorption spans most of the bandpass. As can be seen in Figure 2.1, two of the remaining four sources found to show signs of outflows presented in S20 based on OH absorption more blueshifted than detectable CO emission (SPT0544-40 and SPT2311-54) also contain large changes in atmospheric absorption across the OH-containing bandpasses, requiring a proper accounting of the measurement uncertainties at the velocities of the putative blueshifted OH absorption. We recommend that, for observations in spectral lines, example scripts for data calibration and analysis of ALMA data in CASA include descriptions for assessing the accuracy of bandpass calibration and computing the measurement uncertainties in individual spectral channels.

## 2.6 Acknowledgments

J. Lim and J. Nianias acknowledge support from the Research Grants Council of Hong Kong for conducting this work under the General Research Fund 17312122. This paper makes use of the following ALMA data: ADS/JAO.ALMA#2018.1.00191.S, ADS/JAO.ALMA#2016.1.01499.S. ALMA is a partnership of ESO (representing its member states), NSF (USA) and NINS (Japan), together with NRC (Canada), MOST and ASIAA (Taiwan), and KASI (Republic of Korea), in cooperation with the Republic of Chile. The Joint ALMA Observatory is operated by ESO, AUI/NRAO and NAOJ. We also acknowledge the assistance provided by the ALMA helpdesk East Asia.

## 2.7 Software

CASA ([McMullin et al., 2007](#)), Astropy ([Astropy Collaboration et al., 2013, 2018, 2022](#)),  
Matplotlib ([Hunter, 2007](#)), ESSENCE ([Tsukui et al., 2023](#))

## Chapter 3

# **Spectral Signatures of Outflows from Low-mass Galaxies in the Early Universe**

The following chapter is drawn from a paper currently in preparation for submission to *The Astrophysical Journal* entitled "Investigating Spectral Signatures of Outflows from Lyman- $\alpha$  Emitters in the Early Universe" by James Nianias, Jeremy Lim, Yik Lok Wong, Gordon Wong, Ishika Kaur, and Wenjun Chen. The entire paper – including all figures and writing – has been prepared by me. I also performed all data analysis, except for an early version of the spectral extraction and fitting routines, which was written by co-authors Y.L.W., G.W., I.K., and W.C. Additional explanatory figures and footnotes have been included for the purpose of this thesis.

## Abstract

Lyman- $\alpha$  emission from high- $z$  star-forming galaxies has become a key way to probe outflows in the early universe due to its resonant nature, which strongly couples the emergent line profile to gas kinematics. Typical Lyman- $\alpha$  profiles are explained in terms of idealised expanding-shell models; however, empirically-motivated interpretations of Lyman- $\alpha$  profiles that make use of other spectral features are limited. Here, we analyse the kinematics of emission/absorption lines in the spectra of 401 gravitationally-lensed Lyman- $\alpha$  sources revealed via blind spectroscopy of galaxy clusters with the Multi-Unit Spectroscopic Explorer (MUSE). Using metal emission lines to measure the systemic redshifts, we confirm that the Lyman- $\alpha$  profiles are consistent with the kinematics expected from outflowing gas. In cases where interstellar absorption lines are detected, we find their kinematics and line ratios to be consistent with clumpy outflows. We investigate the relations between Lyman- $\alpha$  line profile and emission/absorption lines, finding that double-peaked Lyman- $\alpha$  lines are associated with stronger high-ionization emission lines (suggesting more intense ionization fields), yet weaker absorption lines (suggesting more gas-poor environments) with less strongly blueshifted velocities (suggesting slower outflows) compared with single-peaked Lyman- $\alpha$  lines. We compare our results with predictions of expanding shell models, finding that the models may overestimate the impact of the intrinsic Lyman- $\alpha$  line width to the appearance of blueshifted peaks.

### 3.1 Introduction

In the hierarchical picture of structure formation, properties of massive galaxies are influenced by processes that take place in the low-mass galaxies from which they form. In particular, outflows from low-mass star-forming galaxies in the early universe may influence the subsequent galaxy luminosity function (e.g. [Kereš et al. 2009](#)), mass-metallicity relation (e.g. [Ma et al. 2016](#)), and baryon fraction of galaxies (e.g. [Papastergis et al. 2012](#)). Observations of outflows from low-mass star-forming galaxies are therefore pivotal to our understanding of cosmic evolution.

One of the most successful ways to detect and study star-forming galaxies in the early universe is via Lyman- $\alpha$  (Ly $\alpha$ ) emission. Due to the abundant Ly $\alpha$  photons produced in star forming regions via re-processing of extreme UV radiation ( $\lambda < 912 \text{ \AA}$ )

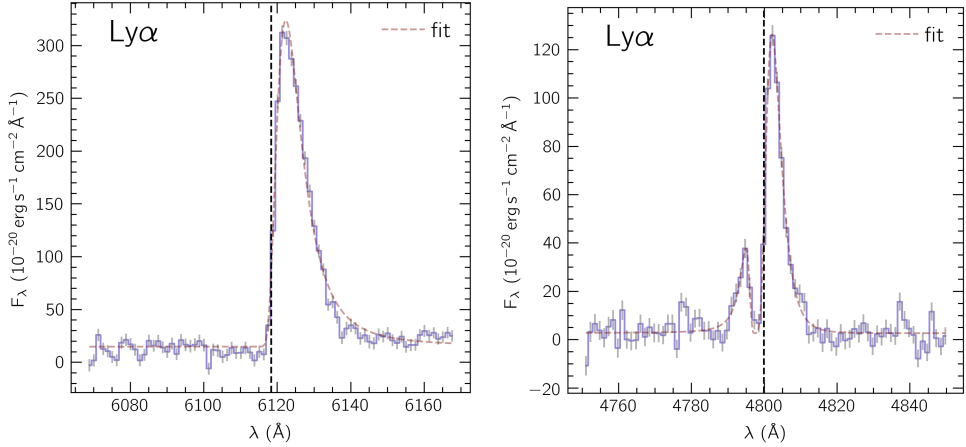


**Figure 3.1:** Some examples of Ly $\alpha$  profiles. **(a)** a single asymmetric peak with skew towards longer wavelengths. **(b)** a double-peaked profile with blueshifted peak skewed to shorter wavelengths. These profiles are typical of Ly $\alpha$  emitters at low and high redshifts, and can be explained in terms of scattering through an expanding medium (i.e. outflows).

from young stars, even low-mass galaxies that are extremely faint in the continuum can be detected via the Ly $\alpha$  line. As such, Ly $\alpha$ -emitting galaxies include some of the lowest-mass objects yet seen at early epochs ( $z \gtrsim 3$ ). When assisted by gravitational lensing by foreground galaxy clusters, observations of rest-frame UV and optical/NIR continuum with the Hubble Space Telescope (HST) and James Webb Space Telescope (JWST) find Ly $\alpha$ -emitting galaxies with masses as low as  $\sim 10^6 M_\odot$  and specific star formation rates (sSFRs) as high as  $\sim 10^{-6} \text{ yr}^{-1}$  (Iani et al., 2024), putting them in the starburst regime above the star-forming main sequence. The fact that Ly $\alpha$  is a resonant line means that the emergent line profile is strongly coupled to the kinematics of the interstellar medium (ISM). This makes the Ly $\alpha$  itself an invaluable tool with which to study processes taking place in these galaxies: outflows, inflows, and escape of Lyman continuum (LyC) into the intergalactic medium (which is believed to be a primary driver of cosmic reionization at  $z \gtrsim 6$ ).

Ly $\alpha$  emission lines from star-forming galaxies take on a range of spectral profiles, but the vast majority fall into one of two broad categories: (i) a single, asymmetric peak skewed towards longer wavelengths, or (ii) a double-peaked profile, where there is an additional weaker blueshifted peak skewed towards shorter wavelengths. Examples of each of these line profiles are shown in Figure 3.1. Henceforth, we refer to peaks skewed towards longer wavelengths as "red peaks" regardless of whether a blue peak is also present. Provided the systemic velocity of the source can be measured, such Ly $\alpha$  profiles can be explained in terms of radiative transfer through outflows: Ly $\alpha$  photons that are redshifted relative to the systemic velocity of the source are shifted out of resonance with the intervening gas, which is blueshifted, and so can escape to the observer more easily. In fact, some of the earliest observations of Ly $\alpha$ -emitting galaxies found direct evidence of outflows in the form of blueshifted metal absorption lines along with a characteristic

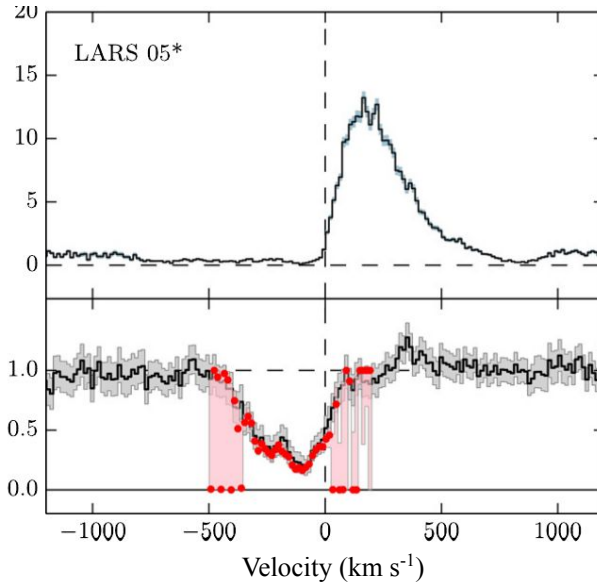


**Figure 3.2:** Comparison of Ly $\alpha$  emission line (above) with stacked low-ionization interstellar absorption lines (below, black trace) from a Ly $\alpha$ -emitting galaxy in velocity space, with systemic velocity of the host galaxy set to zero. While the Ly $\alpha$  profile is redshifted and skewed towards higher velocities (wavelengths), the absorption is blueshifted, indicative of outflowing gas. The red points in the lower panel indicate the estimated covering fraction of optically-thick neutral gas clumps. Figure reproduced from Rivera-Thorsen et al. (2015)

red-skewed Ly $\alpha$  peak (Lequeux et al., 1995) (see Figure 3.2 for a more recent example). In the ensuing years, many more such Ly $\alpha$  profiles were found thanks to the sensitivity afforded by 8-10 m class telescopes as well as HST (see review by Ouchi et al. 2020, and references therein). Blueshifted metal absorption lines indicative of outflows have also been found in more Ly $\alpha$ -emitting galaxies both at low (Chisholm et al., 2016) and high (Steidel et al., 2010) redshifts. Parallel to these observations, Monte-Carlo radiative transfer (RT) models consisting of expanding shells of gas have been developed that are able to qualitatively reproduce the observed Ly $\alpha$  profiles, thus providing solid theoretical support for outflows (e.g. Ahn 2004, Verhamme et al. 2006, Orsi et al. 2012). Subsequently, approaches have been developed to estimate outflow parameters such as expansion velocity and neutral column density by fitting observed Ly $\alpha$  spectra using grids of these RT models (Gronke et al., 2015; Orlitová et al., 2018; Gurung-López et al., 2019, 2022). When applied to, for instance, low-z Green Pea galaxies, such fitting approaches are generally able to successfully reproduce the Ly $\alpha$  profiles (Yang et al., 2016). However, they fail to do so when the expanding shell parameters are constrained based on other spectral properties: systemic redshifts and intrinsic Ly $\alpha$  line widths from optically-thin Balmer emission lines (which originate from the same gas as the Ly $\alpha$  but are not subject to the same radiative transfer effects), and expansion velocities from blueshifted UV absorption lines. Thus, while RT models universally agree that outflows are required to reproduce the Ly $\alpha$  profiles, idealised expanding shell models

may be of limited use in determining the precise properties of the outflows (Orlitová et al., 2018).

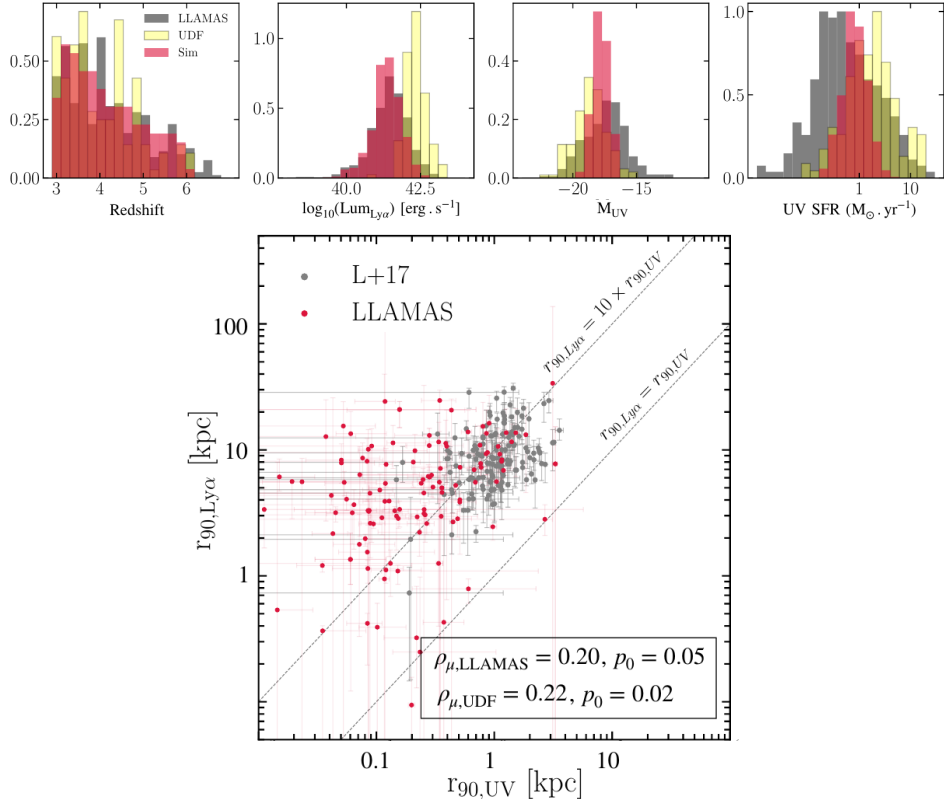


**Figure 3.3:** *Upper:* Distributions in, from left to right, redshift, intrinsic Ly $\alpha$  luminosity, intrinsic UV magnitude, and intrinsic star formation rate estimated from rest-frame UV luminosity using the Kennicutt relation (Kennicutt, 1998). Intrinsic values are corrected for the effects of gravitational lensing. The dark grey histograms represent the sample of lensed Ly $\alpha$  emitters analysed in this paper, the yellow histograms represent MUSE Hubble Ultra-Deep Field (UDF) survey sources (Bacon et al., 2017), while the red histograms represent simulated low-mass Ly $\alpha$  sources from a cosmological radiation hydrodynamic simulation. *Lower:* Circularized 90% light radii based on analytic light profiles fitted to the Ly $\alpha$  emission from MUSE versus the UV continuum emission from HST for the lensed Ly $\alpha$  sources considered here (red points, in which case the light profiles are generated in the source plane) and the UDF sample (grey points). Some of the lensed objects are extremely small after correcting for lensing magnification, just a few pc or tens of pc. Both plots are reproduced from Claeysens et al. (2022).

In this paper, we study a large sample ( $N \sim 1000$ ) of spectra from gravitationally-lensed Ly $\alpha$ -emitting galaxies observed with the Multi-Unit Spectroscopic Explorer (MUSE; Bacon et al. 2010), and catalogued by Richard et al. (2021) (R21 henceforth). Drawing on MUSE observations of 12 lensing clusters, as well as deep HST observations, R21 uncovered a large number of Ly $\alpha$ -emitting galaxies at  $2.9 < z < 6.7$ , the morphologies of which have subsequently been studied in further detail by Claeysens et al. (2022). Thanks to the magnification provided by gravitational lensing, some of these objects are among the faintest and most compact galaxies yet seen in the early

universe (see, e.g., Meštrić et al. 2022; Vanzella et al. 2017; Messa et al. 2024). Figure 3.3 shows distributions of some of the source properties of our sample from Claeysens et al. (2022). The boost in signal-to-noise ratio (SNR) provided by gravitational lensing also enables the detection of faint spectral features that may otherwise be undetected. We analyse the spectra of these objects to search for evidence of outflows by (i) using nebular metal emission lines (where detected) to trace their systemic velocities, against which the Ly $\alpha$  profiles can be compared, and (ii) searching for evidence of blueshifted absorption lines. We search for trends that might shed light on the interplay between the shape of the emergent Ly $\alpha$  profiles, the outflows, and the physical properties of the starburst regions that power them. We complement this analysis by fitting expanding shell RT models to the Ly $\alpha$  spectra, providing an alternative insight into what physical parameters may influence the shape of the Ly $\alpha$  profile, and evaluate the reliability of such models.

In Section 3.2, we provide details about the catalogues of R21, on which our analysis is based. In Section 3.3, we provide basic details of the MUSE observations, from which we extract our spectra, and provide details of the fitting routines and flagging procedures that we use to detect and verify emission/absorption lines. In Section 3.4, we present the results of our fitting, which show universal agreement with expectations based on expanding shell models. We also identify statistical trends that shed light on the relation between the Ly $\alpha$  profiles and source/outflow properties. We then go on to fit expanding shell RT models to the Ly $\alpha$  profiles. In Section 3.5, we discuss interpretations of our results, which suggest outflows that are clumpy and multiphase, and also provide insights into the difference between single- and double-peaked Ly $\alpha$  profiles. We compare these findings against the fitted expanding shell models, finding some tension between the data and the model predictions. Finally, we offer our concluding remarks in 3.6. Throughout the paper, the wavelengths of all emission lines are given in Å unless otherwise stated.

## 3.2 Catalogue

We used the spectroscopic catalogues compiled by R21 as a way to identify high- $z$  Ly $\alpha$  emitting galaxies. Here, we provide a basic overview of how these catalogues were compiled; full details can be found in R21. The sources were detected either based on continuum emission in stacked HST images using SExtractor (Bertin and Arnouts, 1996), or based on line emission seen in the MUSE cubes using MPDAF (*the MUSE Python Data Analysis Framework*, which provides a suite of tools for working with MUSE data; see Piqueras et al. 2019). The catalogues provide source positions, spectroscopic redshifts, and apparent magnitudes in HST ACS/WFC filters (F435W, F606W, F814W, F105W, F125W, F140W, and F160W) among other information. Using the segmentation maps generated by SExtractor, R21 then extract spectra for each source. In separate catalogues, R21 provide information about each spectral line in each spectrum including total flux, central wavelength, and full width at half-maximum (FWHM). They estimate

**Table 3.1:** Information about the MUSE cubes for each cluster. From left to right: cluster name, cluster redshift, J2000 coordinates at center of MUSE cube (RA,DEC), effective integration time (from R21) in hours, sensitivity for an aperture of diameter equal to  $2 \times$  FWHM, using the median per-pixel variance at 6500 Å, in  $10^{-20} \text{ erg s}^{-1} \text{ cm}^{-2} \text{ Å}^{-1}$

Cluster	$z_{clus}$	Coordinates	$T_{\text{eff}}$	$1\sigma$ sensitivity
A2744	0.308	00:14:20.702, -30:24:00.63	3.5–7	12.20
A370	0.375	02:39:53.122, -01:34:56.14	1.5–8.5	11.64
MACS0257	0.322	02:57:41.070, -22:09:17.70	8	5.63
MACS0329	0.450	03:29:41.568, -02:11:46.41	2.5	10.23
MACS0416(NE)	0.397	04:16:09.144, -24:04:02.95	17	4.75
MACS0416(S)	0.397	04:16:09.144, -24:04:02.95	11–15	8.38
BULLET	0.296	06:58:38.126, -55:57:25.87	2	8.53
MACS0940	0.335	09:40:53.698, +07:44:25.31	8	6.09
MACS1206	0.438	12:06:12.149, -08:48:03.37	4–9	8.98
RXJ1347	0.451	13:47:30.617, -11:45:09.51	2–3	7.66
SMACS2031	0.331	20:31:53.256, -40:37:30.79	10	10.07
SMACS2131	0.442	21:31:04.831, -40:19:20.92	7	4.43
MACS2214	0.502	22:14:57.292, -14:00:12.91	7	5.93

these parameters using the spectral fitting module Pyplatefit<sup>1</sup>, which fits families of lines (or templates), with all lines in each family being fitted simultaneously with the same central velocity and FWHM. In emission, the resonant doublets O viλλ1032, 1038, N vλλ1238, 1243, and C ivλλ1548, 1551 are each fitted as distinct families, while the forbidden N ivλλ1483, 1487, He iiλ1640, O iii]λλ1661, 1666, N iiiλ1750, Si iii]λλ1883, 1892, and C iii]λλ1907, 1909 lines are all fitted simultaneously. In absorption, 19 lines are fitted simultaneously, including the aforementioned resonant doublets, as well as Si iiλ1260, O iλ1302, C iiλ1334, and Si ivλλ1394, 1403. The continuum is fitted using stellar population models of Bruzual and Charlot (2003). For more information on Pyplatefit, see R21. The advantage of this approach that it can provide accurate redshifts even in cases where the SNR of individual lines is too low for them to be detectable. The downside is that any systematics affecting one or two lines can be carried forward to the rest of the template; this is especially concerning since MUSE spectra inevitably contain some residual atmospheric features, which can masquerade as emission/absorption lines. Any systematics resulting from the continuum subtraction (due to, for example, contamination by light from cluster members, or residual atmospheric continuum) may have a similar effect. For this reason, we perform independent fitting of each spectral line (or doublet) to supplement the results of R21.

<sup>1</sup><https://pyplatefit.readthedocs.io/en/latest/tutorial.html>

### 3.3 Archival Observations and Data Reduction

#### 3.3.1 MUSE/VLT Integral Field Spectroscopy

We obtained the calibrated and sky-subtracted MUSE spectral cubes used in R21<sup>2</sup>. Each cube corresponds to an observation of a different cluster, except for MACS 0416, which has two cubes (labelled NE for northeast and S for south). R21 perform sky subtraction of each cube (in addition to the sky subtraction done by the MUSE pipeline), using the Zurich Atmospheric Purge software (ZAP; Soto et al. 2016). Full details about the data reduction used to generate the cubes from the raw frames can be found in R21. We summarise the most important information about each cube in Table 3.1.

#### 3.3.2 Sample Selection and Spectrum Extraction

We selected all sources from the R21 catalogues that have reported Ly $\alpha$  SNR greater than 3.0. We then placed apertures at the corresponding locations in the MUSE data cubes and extracted 1D spectra along with uncertainties using MPDAF. This resulted in 842 spectra in total. We chose to extract spectra from apertures rather than from across the entire segmentation map of each source as in R21 in order to better confine the spectra to the brightest continuum regions of the respective sources, where features such as absorption lines and optically-thin emission lines may be more easily detected. We set the aperture diameter to be 2× the FWHM of the point-spread function (PSF) of the corresponding MUSE field at 7000 Å as listed in R21. The spectra exhibit a wide range of Ly $\alpha$  emission profiles as well as spatial morphologies (which may also be significantly distorted by strong gravitational lensing). The metal emission lines, on the other hand, generally appear to arise from more compact, often spatially-unresolved regions. This is unsurprising given that the Ly $\alpha$  halos often extend far beyond the UV continuum of the associated object (Claeyssens et al., 2022), though in some cases the apparent compactness of the metal emission regions may also be due to poor SNR. We show examples illustrating the range of Ly $\alpha$  spatial morphology and spectral profiles, as well as the compactness of the metal emission line sources in Figure 3.4.

#### 3.3.3 Initial Spectral Fitting

For each spectrum, we fitted analytic profiles to all the lines listed in the R21 catalogues using `scipy.curve_fit` with a Trust Region Reflective algorithm. For Ly $\alpha$  lines, we initially attempted a fit using two asymmetric gaussian profiles as defined in Shibuya et al. (2014):

$$f(\lambda) = A \exp\left(-\frac{(\lambda - \lambda_c)^2}{2\sigma_{\text{asym}}^2}\right) \quad (3.1)$$

where  $A$  and  $\lambda_c$  are the amplitude and peak wavelength, respectively, and  $\sigma_{\text{asym}} \equiv (a(\lambda - \lambda_c) + d)$  where  $a$  and  $d$  are, respectively, the asymmetry parameter (positive for skew towards longer wavelengths, and negative for skew towards shorter) and characteristic

---

<sup>2</sup>the data cubes are available upon request from the authors.

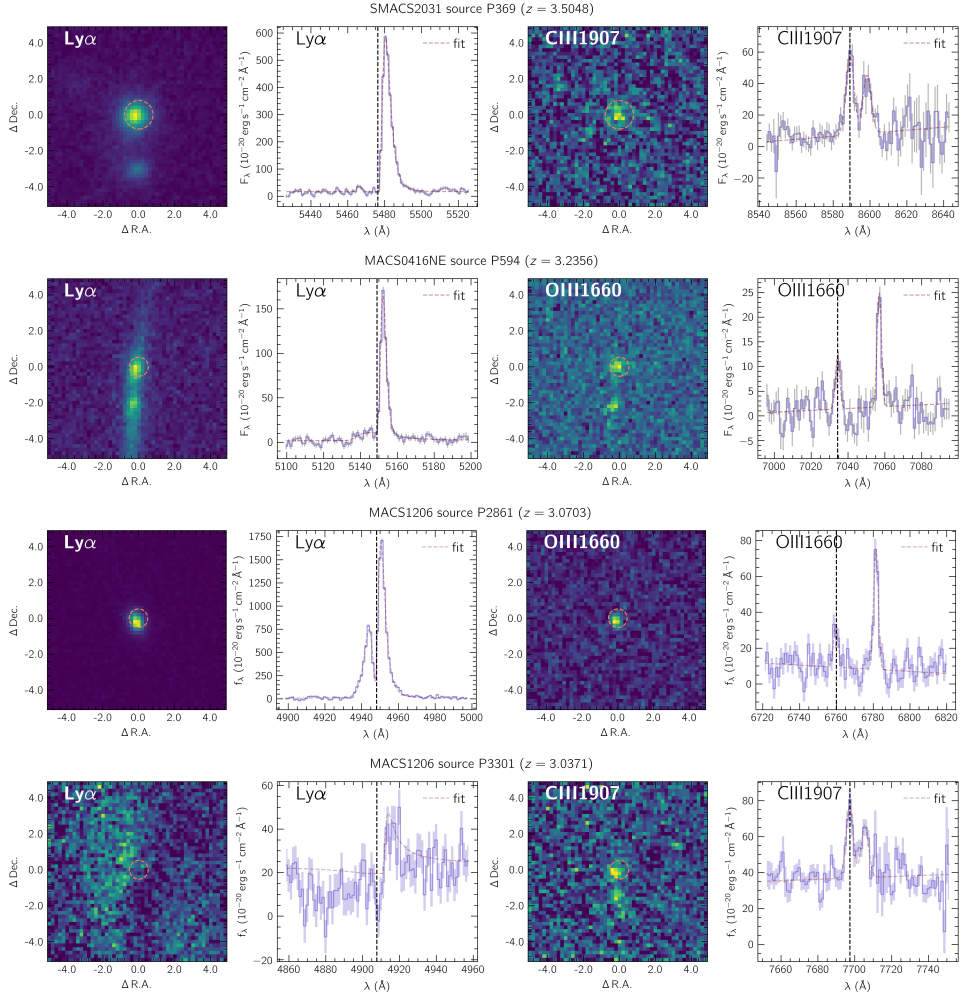


**Figure 3.4:** Some examples of Ly $\alpha$ -emitting sources. *First column:* pseudo-narrowband MUSE images, showing apertures used to extract spectra. The Ly $\alpha$  morphology can be extended (first row), distorted into an arc by gravitational lensing (second row), compact (third row) or so weak as to be only marginally detected (final row). *Second column:* Ly $\alpha$  profiles in the extracted spectra, showing a strongly singly-peaked profile (first row), a dominant red peak with a marginally-detected blue peak (second row), a clearly detected blue peak (third row), an SNR-limited profile (fourth row), and a blue-skewed single peak (fifth row). *Third column:* the same sources but now shown in pseudo-narrowband metal emission line images, showing much more compact morphology than Ly $\alpha$  in all cases. *Fourth column:* the same emission lines in the extracted spectra. In all spectra, we show the fitted line profiles that we use to derive spectral properties.

dispersion. We also included an additive constant to fit the local continuum level. Using the best-fit parameters, we calculated the total flux by integrating under the model profile. We obtained uncertainties in the fitted parameters via bootstrapping, i.e. introducing random gaussian perturbations to the spectra with standard deviations equal to the respective uncertainty in each channel, and then repeating the fitting process as well as the calculation of total flux. We took the median absolute deviation of the distribution in each parameter to be the uncertainty (this is more robust against extreme

outliers, which we found to be commonplace when fitting asymmetric gaussians).

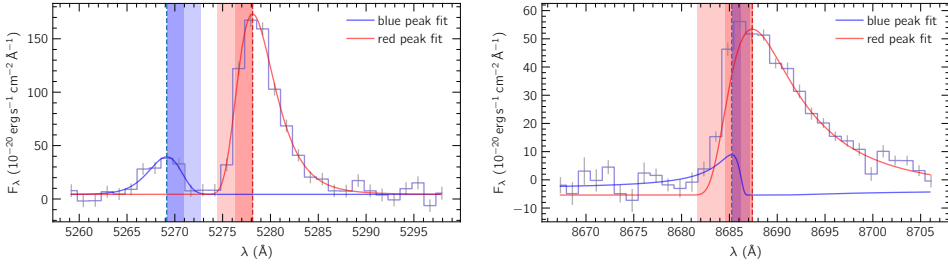


**Figure 3.5:** Ly $\alpha$  profiles demonstrating the criterion by which we consider the red and blue peaks to be resolved (left) or unresolved (right). In both cases, the lines have been fitted with two asymmetric gaussians. The peak wavelengths are shown with dashed lines, while the dark shaded bands indicate the distance between the respective peaks and the points at which the profiles obtain half of their maximum values (the light shaded bands show double this distance). For the two components to be considered resolved, neither of the shaded bands of one component may overlap with the peak wavelength of the other component. In the resolved case, the blue band does not extend to longer wavelengths than the red dashed line, nor does the red band extend to shorter wavelengths than the blue dashed line. In the unresolved case, the red band covers the blue dashed line.

We rejected any putative blue components with  $\text{SNR} < 3.0$ , as well as those that were spectrally unresolved from the red component. The definition of "spectrally resolved" for two asymmetric gaussians is not as simple as in the case of two conventional gaussians, where the Rayleigh criterion can be employed, so we instead defined two lines to be spectrally resolved when the following criterion was satisfied:  $\lambda_R - \lambda_B > \max(W_{B,r}, W_{R,l})$ , where  $W_{B,r}$  ( $W_{R,l}$ ) is 2 $\times$  the distance from the peak wavelength to the wavelength at which the asymmetric gaussian obtains half of its maximum value on the right (left) side of the peak; see Figure 3.5 for illustrative examples. In cases where no significant blue component can be found that reaches these criteria, we calculated 3 $\sigma$  upper bounds, estimating the 1 $\sigma$  uncertainty using the local standard deviation of the spectrum in the region that we searched for a blue peak.

For the other emission and absorption lines, we fitted conventional gaussian profiles along with linear functions to fit the local continuum within  $\pm 25 \text{ \AA}$  of the reported observed wavelength in the R21 catalogues. In the case of doublets such as CIII] $\lambda\lambda 1907.1909 \text{ \AA}$ , we fitted two gaussian profiles simultaneously with the same central velocity and width, though leaving the respective amplitudes as independent parameters. We constrained the central wavelengths of the gaussians to be within  $\pm 6.25 \text{ \AA}$  of the observed wavelength listed in the R21 catalogues. We also constrained the FWHM of the fitted gaussians to be at least  $2.40 \text{ \AA}$  in wavelength space and at most  $300 \text{ km s}^{-1}$  in velocity space: the lower bound was chosen to reflect the approximate spectral resolution of MUSE (which is very nearly constant with wavelength) and helps to avoid fitting to narrow features that are occasionally left after sky subtraction, while the upper bound was set so as to avoid fitting to any gradual fluctuations in the spectral baselines

that can arise due to contamination by nearby cluster members. We obtain uncertainties in all fitted parameters directly from the covariance matrix produced by the fitting module. We chose this method over the bootstrapping that we employed for the Ly $\alpha$  profiles because of its much lower computational cost (as it only required us to run the fitting routine once for each line) and the large number of emission/absorption lines in the sample ( $\sim 19\,000$ ). In cases where the SNR of any line is below 3.0, we discard the fit and calculate the upper bound for the flux to be 3 $\times$  the corresponding uncertainty.

### 3.3.4 Flagging potential contaminants

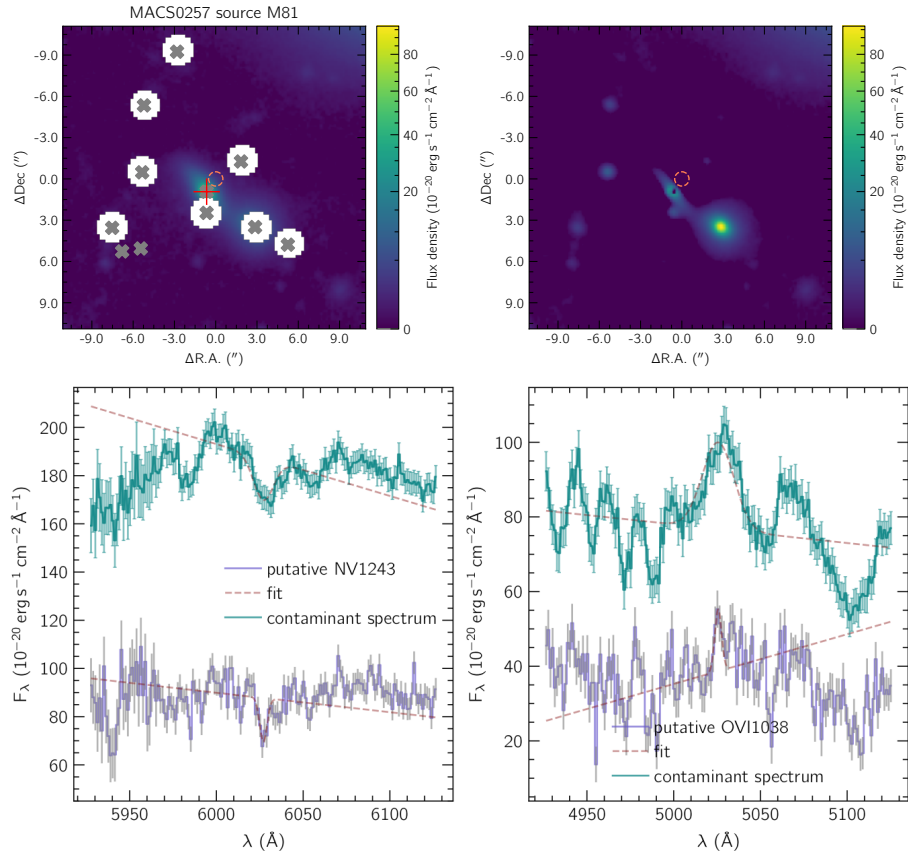


**Figure 3.6:** Example illustrating how we identify possible cases of contamination by nearby cluster members. *Upper row:* postage stamp cutout image generated from the MUSE cube by averaging together channels within the range [6900, 7100] Å before (left) and after (right) fitting and subtracting a Sersic profile from the nearest likely contaminating object (indicated with a red cross). The orange circle shows the location of the target source. White circles show the regions that are masked during the Sersic fitting. *Lower row:* putative lines that are identified as possible contaminants. The target spectrum is shown in purple, while the estimated contaminant spectrum is shown above in teal. In cases like this, the lines are flagged and excluded from our analysis.

Following fitting, we cleaned the results of potential contamination from lower-redshift objects. This can happen either due to (i) the misidentification of the

$[\text{O}\,\text{II}]\lambda\lambda 3726.3729\text{\AA}$  doublet for Ly $\alpha$  in the original catalogues of R21, or (ii) contamination of the spectrum of a genuine Ly $\alpha$  source by emission/absorption lines from foreground galaxies. To identify cases wherein the [O II] doublet masquerades as double-peaked Ly $\alpha$  emission, we first searched for putative Ly $\alpha$  profiles that are indistinguishable from [O II] both in the ratio of the central wavelengths (which is  $3728.8/3726.1 = 1.0007$  for the [O II] doublet) as well as the ratio of the red to blue peak (which can vary between 0.35 and 1.5 for the [O II] doublet, depending on the gas density). If neither of these values was more than  $3\sigma$  away from the corresponding value (or range) for the [O II] doublet, we then checked for additional spectral lines that could confirm the redshift of the source independently of the Ly $\alpha$  line. If no such lines existed, the spectrum was flagged and not included in subsequent analysis. In total we identified just four potential [O II] contaminants in this way.

To identify cases where Ly $\alpha$  emitters have their spectral fitting affected by absorption/emission features from cluster members, we first searched the R21 catalogues for foreground stars, cluster members, and/or intermediate redshift galaxies with redshifts below 2.9 (i.e. below all Ly $\alpha$  emitters in our sample) whose centroids fall within  $10.0''$  of each source. We then identified which of these sources are likely to have the largest impact on the target spectrum by comparing their flux-weighted angular separation

$$D^* \equiv \frac{D_{sky}}{\sqrt{F}} \quad (3.2)$$

where  $D_{sky}$  is the angular separation from the target in arcseconds, and  $F$  is the total flux within  $1''$  of the object's centroid. The square root is included to reflect that an object's total flux scales with area rather than linear size. For objects with centroids within  $1\times$  the PSF FWHM from the targets, while also having  $F$  with  $\text{SNR} > 10$ , we assigned  $D^* = -1$  to ensure that they are given priority over much brighter but more distant sources. We took the object with the lowest  $D^*$  value to be the most likely to contaminate the target spectrum. Having established the most likely contaminating object, we estimated the degree to which it actually contaminates the source. To do this, we generated an image of the object from the MUSE data cube by averaging together all wavelength channels within  $[6900, 7100]\text{\AA}$ , and then fitted a Sersic profile to the image. We then used the intensity of the Sersic profile at the position of the target source to estimate how much flux is contributed by the potential contaminating object within the aperture used to extract the target spectrum. We then normalised the spectrum<sup>3</sup> of the potential contaminating object by this value, while setting the spectral uncertainties equal to those of the target spectrum. Finally, to determine whether this object indeed contaminates the target spectrum, for each fitted line with  $\text{SNR} > 3$  in the target spectrum we attempted to fit the same line to the normalised contaminant spectrum, holding the central wavelength and the sign of the flux (i.e. absorption or emission) the same, but allowing amplitude and width of the fitted gaussians to vary. If statistically significant fits were found, we flagged the corresponding line in the target

---

<sup>3</sup>These spectra are obtained directly from the R21 data set available upon request from the authors.

spectrum as likely contaminated, and did not include it in any further analysis. In total, 60 putative detections of spectral lines across 30 spectra were flagged via this procedure.

### 3.3.5 Identifying and Aggregating Lensed Counterparts

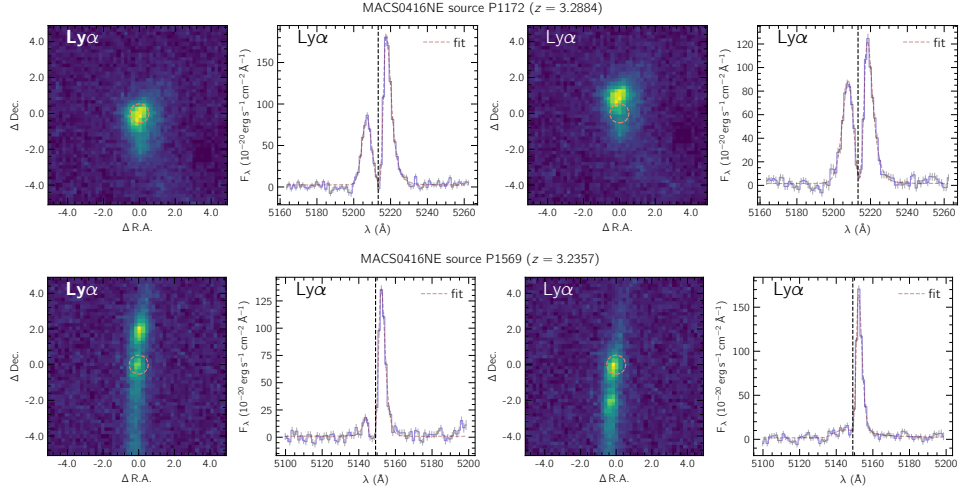


**Figure 3.7:** Examples of Ly $\alpha$  profiles that come from the same object but are sufficiently different to not be grouped together based on our criteria for identifying lensed counterparts. *Upper row*: an example in which two apertures are placed on different parts of the same lensed image, resulting in different Ly $\alpha$  profiles. *Lower row*: an example in which apertures are placed on two different lensed counterimages of the same object, but due to the differences in magnification/lensed morphology yield different Ly $\alpha$  profiles.

Due to the complex nature of the lensing potentials, some sources are lensed into several positions in the image plane. To maximise the SNR of our spectra, as well as to prevent repeated entries in our spectral catalogues, we aggregated together spectra from multiply-lensed images of the same source. We did this by comparing the Ly $\alpha$  profiles of our extracted spectra: if two or more spectra from the same cluster were found to have Ly $\alpha$  profiles that were not significantly different (i.e. having all fitted parameters including peak wavelengths, i.e. redshifts, within  $3\sigma$  of each other) then we assumed them to belong to the same source and group them together. Due to the very diverse range of Ly $\alpha$  profiles, it is unlikely that two unrelated systems could be matched by this procedure. In each matched group, we then discarded any spectra with emission or absorption lines that were previously identified as likely contaminated (see Section 3.3.4) to prevent the contamination being carried forward to the aggregated spectrum. Next, we took the sum of all the spectra in each group and re-fitted all spectral lines using the exact same procedure as described in Section 3.3.3, except now using the fitted parameters from the initial round of fitting as initial guesses for lines previously detected at  $> 3\sigma$ . We found that this averaging had a mildly positive impact on the detection rate of faint spectral features overall (as compared with simply discarding the lensed counterparts and retaining only that with the highest magnification), with 16 newly detected lines at  $5\sigma$  against 6 lost, and 5 newly detected blue Ly $\alpha$  peaks against

3 lost. After accounting for multiply-lensed images in this way, we were left with 639 spectra.

Next, we removed from our results all those spectra that could not be confidently identified as true Ly $\alpha$  emitters. This included all those spectra with low-confidence spectral redshifts according to R21 (those with redshift confidence below the highest rating of 3), that did not show statistically significant asymmetry in our fitted Ly $\alpha$  profiles (i.e the asymmetry parameter  $a$  was within  $3\sigma$  of zero), and furthermore had fewer than two high-confidence ( $> 4\sigma$ ) detections of other spectral lines. This left us with 524 spectra in total.

Inevitably, there are a few cases of multiple spectra that come from the same object but are not grouped together by this procedure. This can happen when a single lensed image is highly spatially extended and/or clumpy, in which case there can be multiple catalogue entries from R21 pointing to different parts of the same lensed image. Alternatively, the apertures placed on different lensed images of the same source may cover different parts of the target due to differences in the lensed morphologies/magnifications of each image. When there is sufficient variation in Ly $\alpha$  profiles across the source, the resulting fitted Ly $\alpha$  profiles can have statistically significant differences. Examples of both of these issues are shown in Figure 3.7. After aggregating our spectra, we cleared any such remaining repeated entries by simply removing spectra from the same cluster with Ly $\alpha$  red peak wavelengths within  $300 \text{ km s}^{-1}$  of one another (retaining whichever spectrum has the higher total SNR in emission plus absorption lines, or, if none are detected, the higher SNR in Ly $\alpha$ ). This left us with 339 spectra in total.

### 3.3.6 Atmospheric Residuals

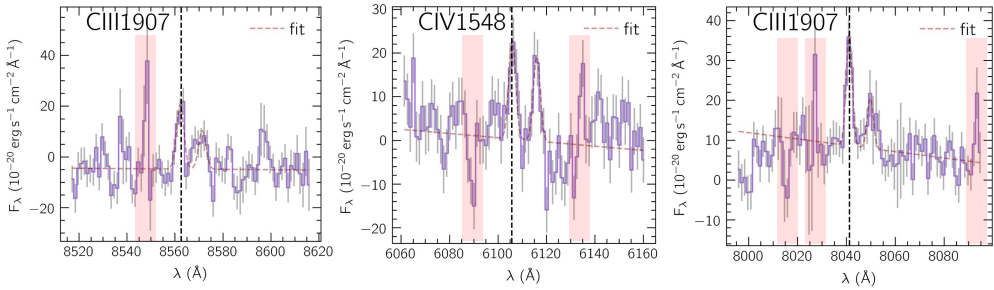


**Figure 3.8:** Examples of probable residual atmospheric features seen in the target spectra (highlighted red), in these cases seen next to genuine emission lines from the targets. The atmospheric lines are generally narrower than the genuine lines, a fact that we exploit to flag potentially spurious fits.

Though ZAP generally removes atmospheric lines to high precision, when inspecting the fits visually we noted some cases wherein significant residual features could be seen either directly coinciding with, or immediately adjacent to, strong atmospheric lines. We show a few examples of these in Figure 3.8. Statistically significant residual

features caused by skylines are, in the overwhelming majority of cases that we visually inspected, narrow when compared with genuine absorption and emission lines, consisting of just one or at most two adjacent channels significantly above/below the local continuum level. We therefore flagged all fitted lines with FWHM equal to or close to the minimum value allowed by our fitting procedure ( $2.40 \text{ \AA}$  -  $2.41 \text{ \AA}$ , see Section 3.3.3). We also flagged any lines in which the SNR of the line peak was greater than the SNR of the total integrated flux of the line, as this indicates that these lines are dominated by just a single channel. Since it is unlikely to have two false detections with precisely the right separation in wavelength to masquerade as a doublet, we removed any flags from doublets in cases where both lines were detected with  $\text{SNR} > 3.0$ .

### 3.3.7 Final Sample

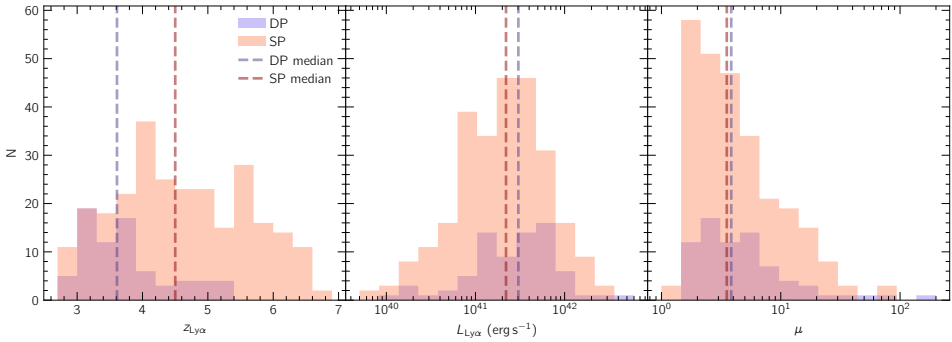


**Figure 3.9:** Left: redshifts of the peaks of the fitted Ly $\alpha$  profiles (in cases where the Ly $\alpha$  is double-peaked, we use the peak wavelength of the redshifted peak). Middle: Ly $\alpha$  luminosities (summing both peaks in double-peaked cases) adjusted for lensing magnification based on the lens models of R21. Right: Magnifications from the R21 lens models.

In Figure 3.9, we show distributions in redshift, Ly $\alpha$  luminosity, and lensing magnifications (from the lens models of R21) for our final sample of 339 Ly $\alpha$ -emitting sources. Though the number of spectra is much reduced by the selection and stacking processes outlined above, almost the full redshift range of is still included in the sample, with the lowest redshift being 2.91, and the highest being 6.62.

## 3.4 Results and Analysis

### 3.4.1 Ly $\alpha$ profiles

Consistent with other studies, we find a diverse range of Ly $\alpha$  profiles, ranging from extreme single-peaks to double-peaks of almost equal height. The overwhelming majority of single-peaked Ly $\alpha$  profiles show a positive asymmetry parameter,  $a$ , (i.e. skewed to longer wavelengths, as in the first row of Figure 3.1) with just 21 profiles (i.e. 8.1%) showing statistically significant negative asymmetry (i.e. skewed to shorter wavelengths). Out of 339 total spectra, we find statistically significant ( $3\sigma$ ) secondary blue peaks in 81

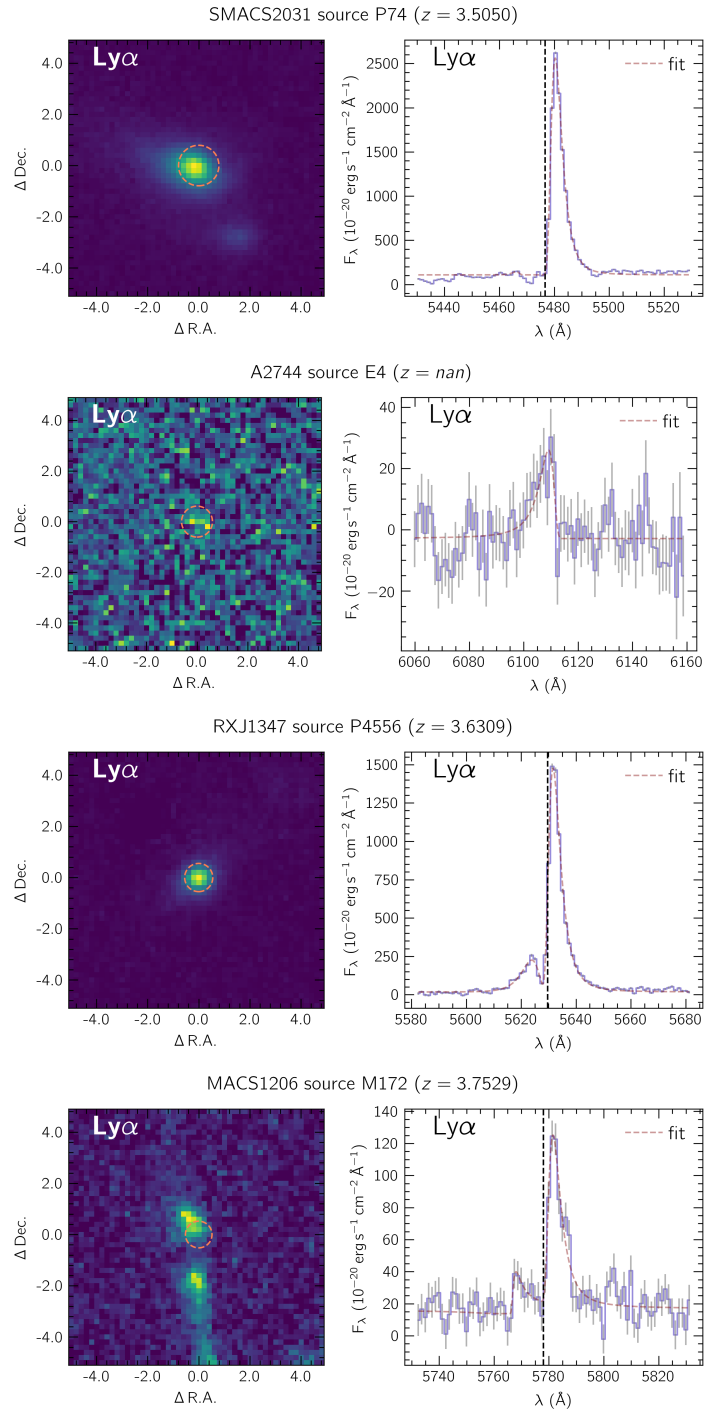


**Figure 3.10:** Examples of Ly $\alpha$  profiles with different skewness. *From top to bottom:* a single-peaked red-skewed profile, a single-peaked blue-skewed profile, a double-peaked profile with blue-skewed blue component and red-skewed red component, and a double-peaked profile where both components are red-skewed (there are no cases where both components are blue-skewed). When metal emission lines are detected, the systemic redshift is indicated with a vertical dashed line.

(i.e. 24%). Among these double-peaked Ly $\alpha$  profiles, none shows negative asymmetry in the red peak (i.e. the more redshifted of the two), and all have stronger red than blue peaks. Henceforth, we refer to all primary red-skewed peaks as "red peaks" regardless of whether the Ly $\alpha$  profile has one or two components. By contrast with red peaks, blue peaks are far more likely to be negatively skewed, with 26 (33%) of blue peaks showing statistically significant negative asymmetry, and 18 (22%) showing statistically significant positive asymmetry. In Figure 3.10, we show examples of all these profiles: single peaks with red-skewed profiles, single peaks with blue-skewed profiles, double peaks with blue-skewed blue components and red-skewed red components, and double-peaked profiles where both components are red-skewed.

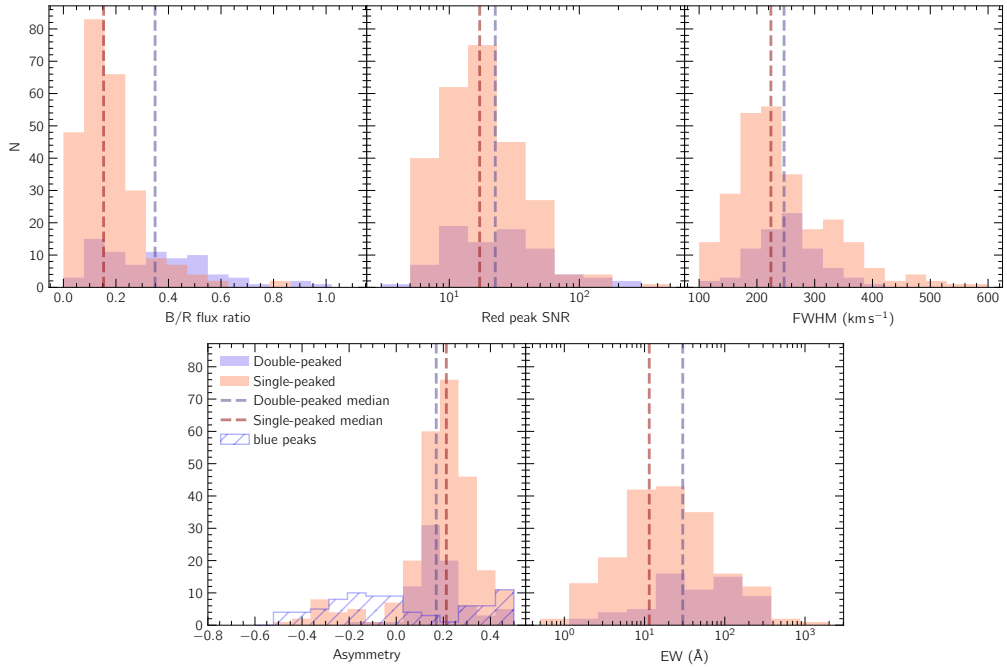


**Figure 3.11:** From left to right: (i) B/R ratios of fitted Ly $\alpha$  spectral profiles with double peaks compared with upper bounds for single peaks; (ii) Ly $\alpha$  SNR in the red peaks; (iii) width of red peaks for single- vs double-peaked Ly $\alpha$  profiles; (iv): Asymmetry of red peaks for single- vs double-peaked Ly $\alpha$  profiles; (v) total Ly $\alpha$  equivalent width.

In Figure 3.11, we compare distributions of selected parameters in single- and double-peaked cases. As shown in the leftmost panel, the ratio of flux in the blue peak to the red peak (B/R ratio) spans a wide range, from < 0.01 in some extreme single-peaked cases (in which case the ratios are upper bounds), to  $\sim 1.0$  in extreme double-peaked cases. Moreover, whether or not a blue peak is detected is not determined solely by the SNR of the spectrum, as the median  $3\sigma$  upper bound for the ratio of flux in the blue peak to the red peak (B/R ratio) is substantially lower than the median B/R ratio in spectra where blue peaks are detected. This is also reflected in the range of SNRs of the Ly $\alpha$  profiles (second panel from left in Figure 3.11), which is approximately the same for single and double-peaked profiles. When we compare the shape of the single-peaked

$\text{Ly}\alpha$  profiles with that of the red peaks in the double-peaked profiles, we find them to be generally slightly narrower and with greater asymmetry, as shown in the middle and second-from-right panels of Figure 3.11. These differences are qualitatively consistent with expanding shell RT models in which single-peaked  $\text{Ly}\alpha$  profiles are associated with faster expansion, which leads to greater asymmetry in the red peak and lower FWHM when the outflow velocity is very high (Verhamme et al., 2006); we discuss this issue in more detail in Section 3.5. Also shown is the distribution of asymmetry parameters among blue peaks in double-peaked cases, demonstrating a much stronger tendency towards negative asymmetry when compared with red peaks, again consistent with expanding shell models. Finally, in the rightmost panel, we compare the  $\text{Ly}\alpha$  equivalent width (EW) in single- and double-peaked profiles, where  $\text{EW} = F_{\text{Ly}\alpha}/f_\lambda(\text{cont.})$ , with  $F_{\text{Ly}\alpha}$  being the integrated flux under the  $\text{Ly}\alpha$  line and  $f_\lambda(\text{cont.})$  being the rest-frame flux density of the continuum. Here, we have used the continuum level of the  $\text{Si III}\lambda 1260$  line rather than the continuum level fitted to the  $\text{Ly}\alpha$  profiles themselves to mitigate the effects of broad  $\text{Ly}\alpha$  absorption troughs that sometimes surround the emission line. We find a tendency for double-peaked profiles to have greater EW, possibly indicating greater  $\text{Ly}\alpha$  escape fractions, harder ionization fields, or both (see Section 3.5 for discussion).

### 3.4.2 Other emission/absorption lines

The fitting procedure described above detected tentative emission (absorption) lines other than  $\text{Ly}\alpha$  at  $\text{SNR} \geq 4\sigma$  that passed the flagging stages described in Sections 3.3.4 and 3.3.6 in 63 (27) spectra. We adopted a more conservative detection threshold of  $4\sigma$  due to the large number of putative detections between  $3\sigma$  and  $4\sigma$  with clear systematic fluctuations in their vicinity with amplitude comparable to the line itself, which makes identification of genuine lines difficult if not impossible. Even for the lines with  $\text{SNR} > 4\sigma$ , it was necessary to manually inspect each spectrum to check for such systematic fluctuations. After manual inspection, we ended up with 39 spectra with highly certain detections of emission lines (i.e. just 12% of sources), and 11 with absorption lines (i.e. just 3% of sources).

#### Emission lines

The most commonly detected metal emission lines are the  $\text{C IV}\lambda\lambda 1548, 1551$ ,  $\text{O III]}\lambda\lambda 1660, 1666$ , and  $\text{C III]}\lambda\lambda 1907, 1909$  doublets, as well as the  $\text{He II}\lambda 1640$ <sup>4</sup> line. Due to their high ionization potentials, all of these lines, especially the  $\text{C IV}\lambda\lambda 1548, 1551$  doublet and  $\text{He II}\lambda 1640$  line, are associated with extreme ionization conditions and low metallicities not seen in typical H II regions in the local universe (see, e.g., Berg et al. 2021).

We find confirmed metal emission lines in  $21/80 = 26\%$  of double-peaked  $\text{Ly}\alpha$  profiles. The yield is much lower in spectra with single-peaked  $\text{Ly}\alpha$  profiles, where

<sup>4</sup>Though He is not strictly classified as a metal, we use the term "metal" lines loosely here to refer to everything except for H lines.

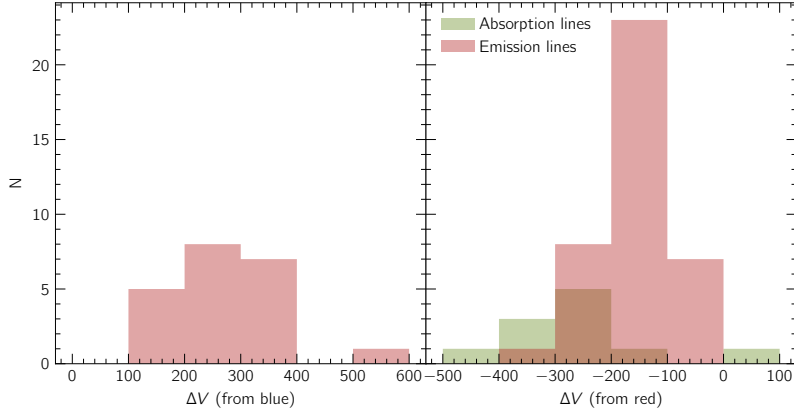


**Figure 3.12:** Velocity offsets of emission and absorption lines relative to the blue Ly $\alpha$  peak, where present, (left) and red Ly $\alpha$  peak (right).

only  $18/258 = 7\%$  have confirmed metal lines. For those spectra where metal emission lines are detected, we estimate the systemic redshift as the average redshift of all the lines detected with  $\text{SNR} > 4\sigma$ , weighted by the square of the respective SNRs. As shown in Figure 3.12(a), comparing these redshifts with those of the Ly $\alpha$  lines (in velocity space), we find that in all cases, the metal emission is blueshifted relative to the red Ly $\alpha$  peak. Conversely, in cases where two Ly $\alpha$  peaks are detected, the emission lines are always redshifted relative to the blue Ly $\alpha$  peak, so as to always fall between the two peaks, as shown in Figure 3.12(b). These trends agree with previous work by Kulas et al. (2012) that measured the systemic velocity of Ly $\alpha$  emitters at  $z = 2\text{--}3$ . Moreover, these results fit qualitatively with expanding shell RT models, and hence provide a compelling case for outflows from these objects.

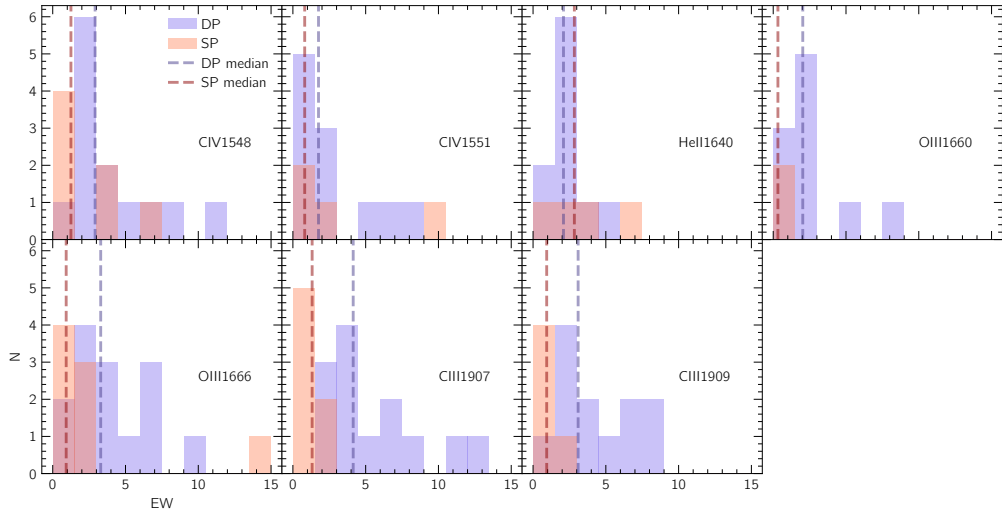


**Figure 3.13:** Equivalent width of selected emission lines in single- vs double-peaked Ly $\alpha$  sources, showing a clear preference for higher EWs in double-peaked sources.

Comparing the equivalent width (EW) of all metal emission lines in single- vs double-peaked Ly $\alpha$  spectra, we find evidence of a positive association between double-peaked Ly $\alpha$  emitters and EW in emission lines, as shown in the histograms in Figure 3.13. As these emission lines are from high-ionization species, the higher EWs suggest more extreme ionization conditions in sources with double-peaked Ly $\alpha$  profiles.

### Absorption lines

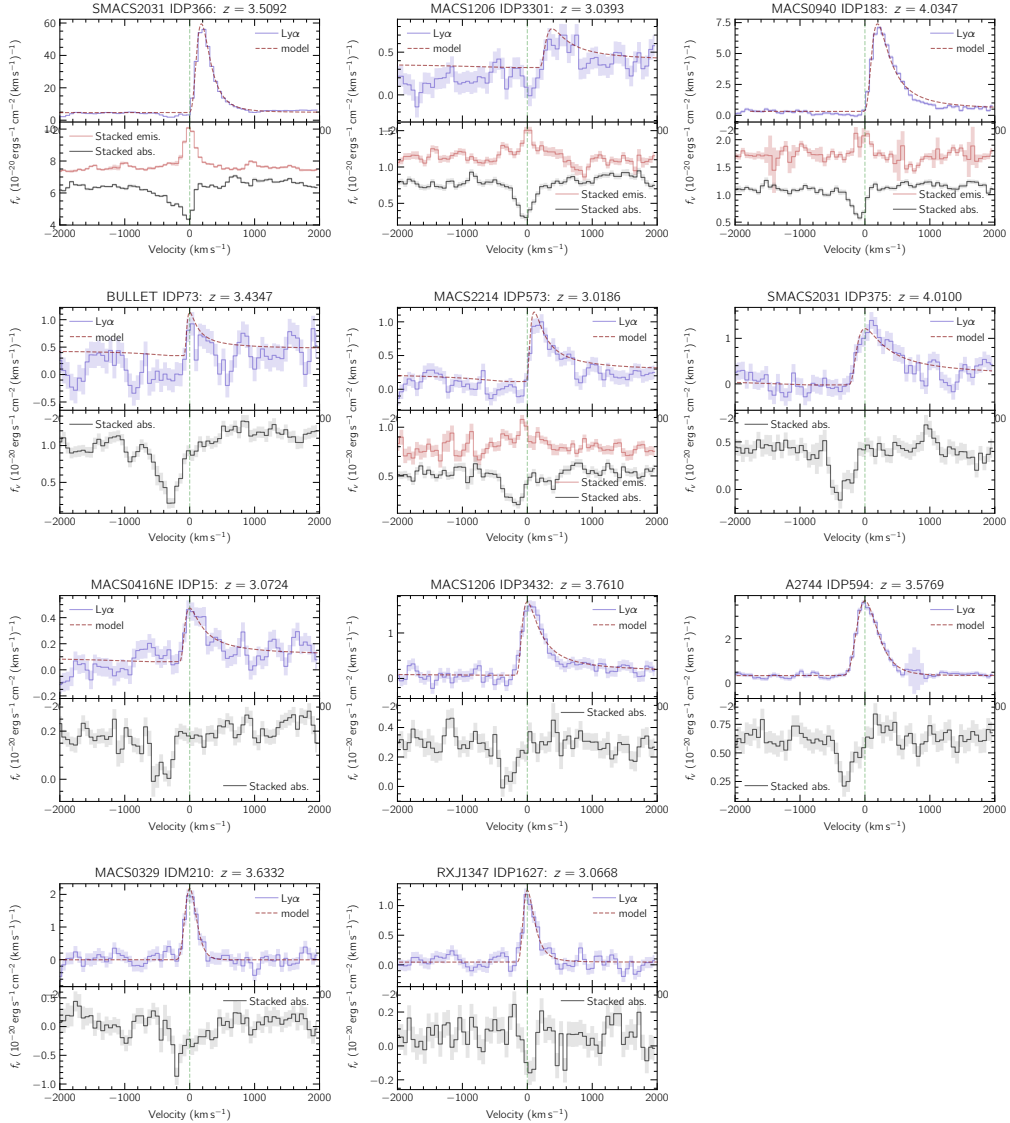


**Figure 3.14:** Comparison in velocity space of Ly $\alpha$  profiles with averaged absorption profiles (weighted by square of respective SNRs). Where emission lines are confidently detected, the stacked emission profile is shown in red, and the zero point of the velocity axis is centered on the systemic velocity. Otherwise, we simply set the zero point to be the peak of the Ly $\alpha$  profile (i.e. most likely not the true systemic velocity).

The most commonly detected absorption lines are the low-ionization lines Si II $\lambda$ 1260

and  $\text{C II}\lambda 1334$ , and the high-ionization  $\text{Si IV}\lambda\lambda 1394, 1403$  doublet. Due to their lower ionization potentials,  $\text{Si II}$  and  $\text{C II}$  are associated with predominantly neutral gas, while  $\text{Si IV}$  traces the ionized phase with temperatures  $T > 10^4 \text{ K}$ . In all spectra where more than one absorption line is detected (six out of 11), both low- and high-ionization species are found, suggesting that the gas is multiphase. Full results showing individual absorption lines are shown in Figures A.1 and A.2. Among the 11 confirmed absorption spectra, all the  $\text{Ly}\alpha$  profiles are all singly-peaked, including some with extremely high SNR ( $> 100$ ), indicating that the lack of detected blue peaks is not merely due to low SNR. In Figure 3.14, we compare the  $\text{Ly}\alpha$ , averaged absorption, and averaged emission profiles for each of these sources. Similarly to how we treated emission lines, we estimate the redshift of the absorption lines in each spectrum by taking the SNR-weighted average of all the absorption lines. In all but one case, we find the absorption lines to be blueshifted relative to the  $\text{Ly}\alpha$  peak, as can be seen in Figure 3.12. In the single case where the absorption is redshifted relative to  $\text{Ly}\alpha$ , there is only one line detected (c.f. a median of 3 for the other absorption spectra), and moreover in the  $\text{O III}\lambda 1660$  line, which is not seen in absorption in any other spectrum. On the basis of these considerations, we do not consider it to be genuine. In four of the absorption spectra, we also detect emission lines: comparing the central velocities of the absorption and emission lines, we find the absorption lines to be blueshifted relative to the emission lines in all cases, with an average blueshift of  $103 \text{ km s}^{-1}$ . We note, however, that the maximum blueshifted velocity may reach as high as  $\sim 1000 \text{ km s}^{-1}$  as can be seen in the far blueshifted wing in the upper left panel of Figure 3.14. Overall, the absorption kinematics are indicative of outflows containing both neutral and ionized gas from these objects.

### 3.4.3 Averaged line profiles

Our fitting procedures did not detect any highly significant absorption lines in spectra with double-peaked  $\text{Ly}\alpha$  profiles. Therefore, to determine whether absorption is present at all in double-peaked sources, as well as to compare outflow kinematics in single- and double-peaked cases, we stacked absorption lines. We performed this stacking in two stages. First, we combined multiple lines within each spectrum, stacking the low-ionization  $\text{Si II}\lambda 1260$ ,  $\text{Si II}\lambda 1527$ , and  $\text{C II}\lambda 1334$  lines. We found that the inclusion of the  $\text{Si II}\lambda 1527$  had a positive impact on the SNR of the resulting spectra, although this line is not included in the R21 catalogues on which we based our initial fitting<sup>5</sup>. In the resulting stacks, we found eight additional tentative cases of absorption in spectra where the systemic redshift can be measured with emission lines, including six with double-peaked  $\text{Ly}\alpha$  profiles. The eight tentative cases are shown in Figure 3.15, plotted against velocity offset from the systemic. While the absorption in these spectra is weak, it appears blueshifted relative to the systemic in all but one case, source P1154 from MACS0416NE (upper left panel), where it is centered at the systemic velocity. These

<sup>5</sup>It is not explained why R21 did not include the  $\text{Si II}\lambda 1527$  line in their spectral templates, but it is reported among other low-ionization lines in the spectra of  $\text{Ly}\alpha$ -emitting galaxies by other authors, e.g., Berry et al. (2012).

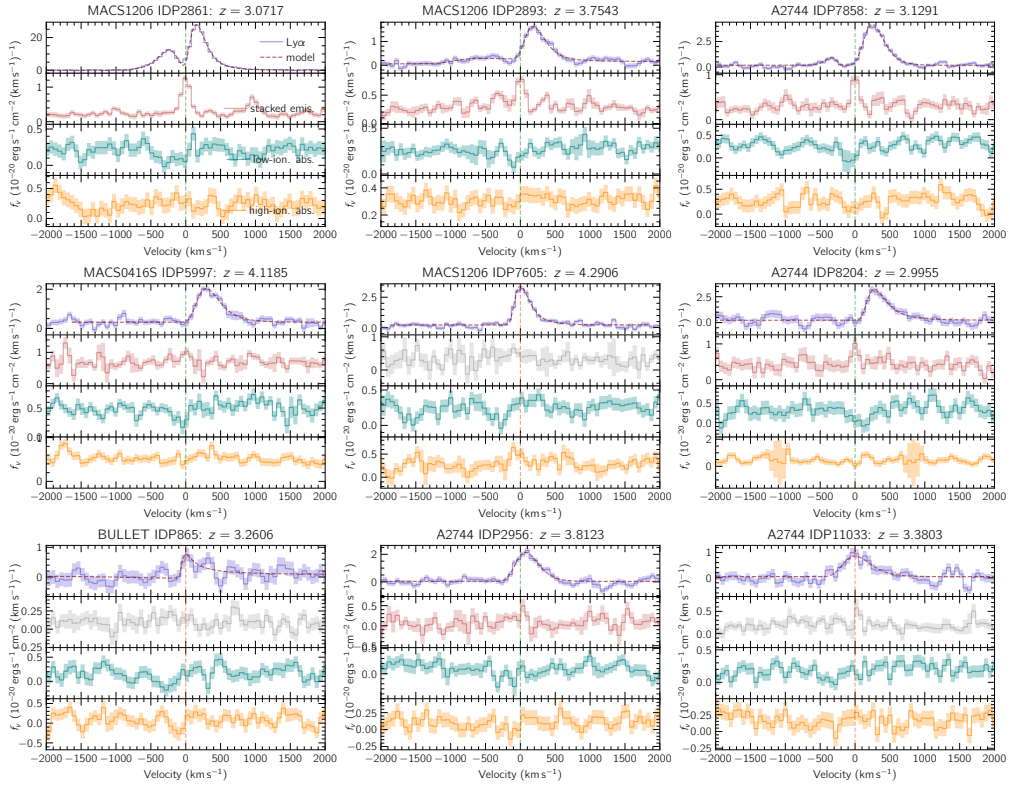


**Figure 3.15:** Some examples of weak stacked absorption ( $\text{C II}\lambda 1334 + \text{Si II}\lambda 1260 + \text{Si II}\lambda 1527$ ), including six seen in double-peaked sources.

absorption profiles suggest that outflows are present in double-peaked Ly $\alpha$  sources as well as single-peaked ones, though the outflow signatures are weak, possibly due to lower column density. Next, we generated representative absorption profiles for single- and double-peaked sources by stacking together absorption profiles from each subsample, weighting each spectrum by its inverse median spectral uncertainty. In this step, we stacked only those spectra where the systemic redshifts had been measured with metal emission lines, as without these measurements it is impossible to align the spectra in velocity space and obtain meaningful kinematic results. The resulting stacked profiles are shown in the left panel of Figure 3.16. Furthermore, we used only the Si II $\lambda 1260$  and Si II $\lambda 1527$  lines here (omitting C II $\lambda 1334$ ) as we found this maximized the SNR (though leaving the absorption profiles qualitatively the same). There is highly significant blueshifted absorption in the single-peaked stack, in contrast to the double-peaked stack in which a weaker, though still significant, dip can be seen bluewards of the average systemic velocity. This suggests higher gas column densities in single-peaked spectra. Furthermore, the absorption trough in the double-peaked stack is much narrower than that of the single-peaked stack, consistent with expanding shell RT models of Ly $\alpha$ , which ascribe the presence of blueshifted peaks to lower expansion velocity. To verify that these differences are statistically significant, we performed a Monte-Carlo procedure in which random perturbations to each spectral channel were

introduced, following a Gaussian distribution with standard deviation equal to the  $1\sigma$  uncertainty. We performed 3000 such iterations, re-fitting the absorption lines each time, and comparing the line EWs and widths (FWHM). We thus constructed 95% confidence intervals for the ratios in EW and line width, finding that the ratios are inconsistent with unity (as an even more stringent test, we found they are also inconsistent with unity at the 99.7% confidence level). We performed the same experiment with the stacked high-ionization Si IV  $\lambda\lambda 1394, 1403$  lines, as shown in the right panel of Figure 3.16, but the double-peaked stacked absorption is not statistically significant.

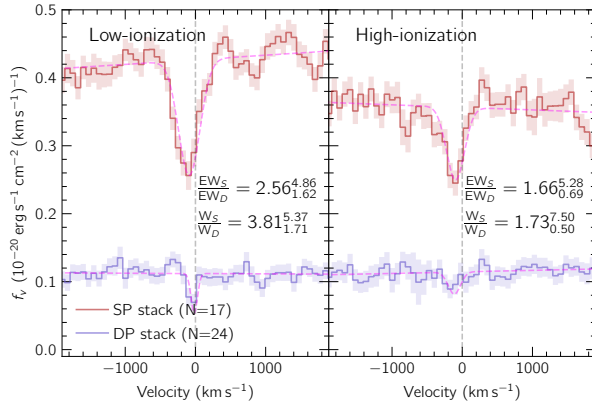


**Figure 3.16:** Stacked absorption lines for single- and double-peaked sources, respectively. *Left:* stacked low-ionization absorption from Si II $\lambda$ 1260 + Si II $\lambda$ 1527. *Right:* stacked high-ionization absorption from Si IV $\lambda\lambda$ 1394, 1403 (both lines combined). The low-ionization is significantly narrower in the double-peaked stack, and also has a lower EW, as shown by the ratios (along with 95% confidence intervals). The high-ionization absorption is not statistically significant in the double-peaked stack.

We also generate stacked spectra for individual absorption lines across spectra with single- and double-peaked Ly $\alpha$  profiles, shown in Figure 3.17 (again stacking only spectra with systemic velocities measured with high-confidence emission lines). Fitting gaussian profiles to each of these lines, we find that the EWs of the absorption lines in the single-peaked stacks are systematically greater than those in the double-peaked stacks by a factor of  $\sim 2$ – $3$ , again suggesting greater column density in single-peaked sources. Though the SNR of each individual DP stack is low, the fact that all four show reduced EW and width relative to the SP stack suggests that the difference is genuine. We show the corresponding EW ratios in each panel of Figure 3.17. Interestingly, we find the same tentative trend in both low-ionization (Si II $\lambda$ 1260, Si II $\lambda$ 1527, and C II $\lambda$ 1334) and high-ionization (Si IV $\lambda\lambda$ 1394, 1403) absorption lines. This suggests that the column density in both neutral and ionized gas may be greater in single-peaked sources, in contrast with some studies that suggest that double-peaked sources simply have a greater fraction of ionized gas (see, e.g., Erb 2015). When we compare the widths of the fitted line profiles, we find the absorption lines in the single-peaked stacks to be systematically wider than those of the double-peaked stacks, by a factor of 2–3, consistent with the overall stacked profiles in Figure 3.16 and suggesting greater outflow velocity in single-peaked

sources<sup>6</sup>.

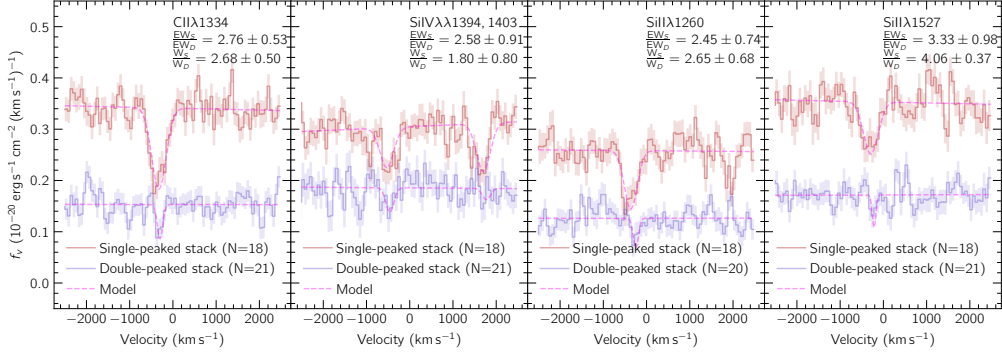


**Figure 3.17:** Stacked  $\text{C II}\lambda 1334$ ,  $\text{Si IV}\lambda\lambda 1394, 1403$ ,  $\text{Si II}\lambda 1260$ , and  $\text{Si II}\lambda 1527$  absorption lines for single- and double-peaked sources. Fitted gaussian models are indicated with magenta dashed lines. Stronger absorption can be seen in both high- and low-ionization lines in the single-peaked stacks.

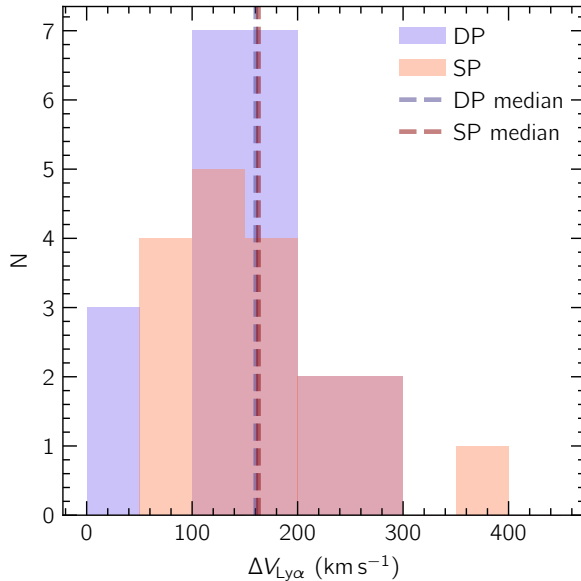


**Figure 3.18:** Velocity offsets of the  $\text{Ly}\alpha$  peaks relative to the systemic velocity as measured by metal emission lines (high-confidence detections only). The median offsets (shown with dashed vertical lines) are almost identical for single- and double-peaked  $\text{Ly}\alpha$  profiles.

We performed a similar stacking procedure with the following emission lines:  $\text{C III}\lambda\lambda 1907, 1909$ ,  $\text{C IV}\lambda\lambda 1548, 1551$ ,  $\text{O III}\lambda\lambda 1661, 1666$ ,  $\text{He II}\lambda 1640$ ,  $\text{Si III}\lambda\lambda 1883, 1892$ , and  $\text{N V}\lambda\lambda 1238, 1243$ . Here, we stacked all spectra with highly significant  $\text{Ly}\alpha$  detections ( $\text{Ly}\alpha$  SNR > 20), regardless of whether the systemic velocity could be measured with metal emission lines, using instead the redshift of the  $\text{Ly}\alpha$  peak as a proxy for

<sup>6</sup>Note that the line width ratios in Figure 3.17 do not take into account the effect of MUSE's LSF, though in the fitting procedure we set a lower bound on the allowed line widths approximately the same as the LSF ( $\sim 2$  channels, or  $100 \text{ km s}^{-1}$  at this velocity scale).

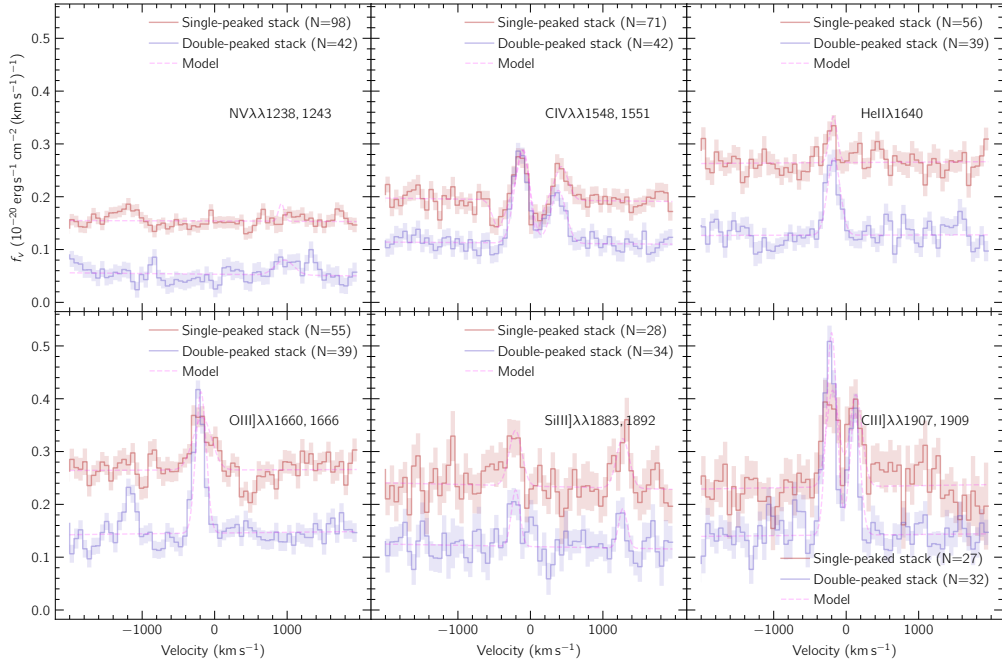


**Figure 3.19:** Stacked  $\text{N V}\lambda\lambda 1238, 1243$ ,  $\text{C IV}\lambda\lambda 1548, 1551$ ,  $\text{He II}\lambda 1640$ ,  $\text{O III]}\lambda\lambda 1661, 1666$ ,  $\text{Si III]}\lambda\lambda 1883, 1892$ , and  $\text{C III]}\lambda\lambda 1907, 1909$  emission lines for single- and double-peaked sources. Fitted gaussian models are indicated with magenta dashed lines. The EW of all detected emission lines is clearly enhanced in sources with double-peaked Ly $\alpha$ .

the systemic. Because the offset of the Ly $\alpha$  relative to the systemic varies, the metal emission lines are imperfectly aligned, or scattered, when stacked. To characterise the extent of this scattering effect, we checked the velocity offsets of the Ly $\alpha$  lines in the 39 spectra with high-confidence metal emission lines. Figure 3.18 shows the distribution in offsets, which ranges between  $\sim 0$  and  $\sim 300 \text{ km s}^{-1}$ , and shows no difference for single- and double-peaked profiles. While this scatter affects the shape of the stacked lines – making them wider – the integrated emission line flux still reflects the average for each subsample, allowing us to compare them. The stacked emission line profiles are shown in Figure 3.19, clearly demonstrating a significantly enhanced emission line EW in double-peaked Ly $\alpha$  spectra compared to single-peaked in  $\text{C III]}\lambda\lambda 1907, 1909$ ,  $\text{C IV}\lambda\lambda 1548, 1551$ ,  $\text{O III]}\lambda\lambda 1661, 1666$ , and  $\text{He II}\lambda 1640$ , in agreement with Figure 3.13, again suggesting a harder ionization field in double-peaked sources. Perhaps the greatest contrast is in the  $\text{He II}\lambda 1640$  line, which is very prominent in the double-peaked stack, but almost undetected in the single-peaked stack. This is particularly telling, as the  $\text{He II}\lambda 1640$  line has the highest ionization potential of all these lines, and thus is associated with very extreme ionization conditions (Nanayakkara et al., 2019). Another notable feature of these spectra is that the  $\text{C IV}\lambda\lambda 1548, 1551$  doublet in the single-peaked stack presents a P Cygni profile with blueshifted absorption. We fit gaussians to each line to extract representative line fluxes (P Cygni profiles consisting of one gaussian in emission and one in absorption to the single-peaked  $\text{C IV}\lambda\lambda 1548, 1551$  stack). We do not

detect any significant N v $\lambda\lambda$ 1238, 1243 emission in either the single- or double-peaked stacks. We compare the EWs of these lines in the single- and double-peaked cases to photoionization models in Section 3.5.

### 3.4.4 Fitting Expanding Shell Models

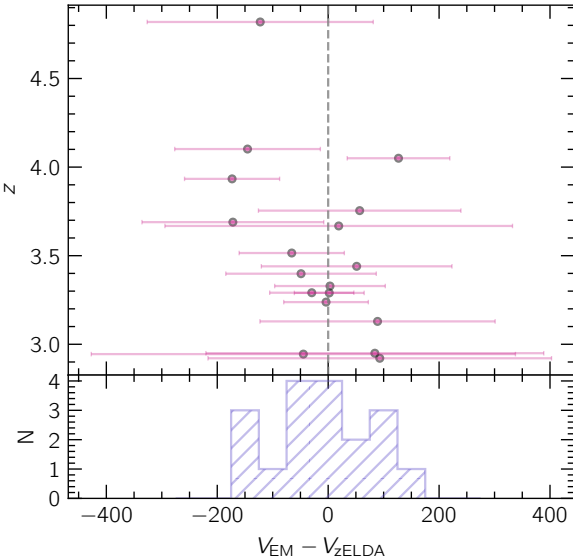


**Figure 3.20:** Comparison of zELDA estimated systemic velocity with that measured using metal emission lines. Uncertainties are shown at the  $3\sigma$  level, indicating generally good agreement between the zELDA predicted and measured systemic redshifts at lower redshifts ( $\lesssim 4$ ).

We make use of the machine-learning-based radiative transfer (RT) modelling code zELDA (Gurung-López et al., 2022, 2019), which is designed to quickly fit expanding-shell RT models to Ly $\alpha$  profiles. zELDA’s neural network is trained on a grid of models that were generated using LyaRT (Orsi et al., 2012), which uses full Monte-Carlo Markov Chain (MCMC) RT fitting to obtain estimates for shell expansion velocity, neutral column density, and dust optical depth. zELDA is much faster than performing MCMC directly and therefore well-suited to analyzing a large number of Ly $\alpha$  profiles as in our sample. For each Ly $\alpha$  profile, we input to zELDA a sub-spectrum of width 100 Å centered on the Ly $\alpha$  peak. We adopt a homogeneous thin (expanding) shell geometry, fitting for systemic redshift  $z_{\text{sys}}$ , expansion velocity  $V_{\text{exp}}$ , H $\text{i}$  column density  $N_{\text{H}}$ , and dust optical depth  $\tau_a$ , as well as the intrinsic line profile, a gaussian of FWHM  $W_{\text{in}}$  and equivalent width  $EW_{\text{in}}$ . We run the neural network 3000 times for each spectrum, each time adding random gaussian noise to each channel scaled to match the uncertainties; we take the “best-fit” value to be the median, and calculate the  $\pm 1\sigma$  uncertainties from the 84<sup>th</sup> and 16<sup>th</sup> percentiles. In many cases, we find good agreement between the models fitted by zELDA and the observed spectra. In other cases, however, there is a large divergence between the zELDA model and the observations. This is especially common among sources with  $z > 4$ , which is unsurprising given that zELDA is trained only on spectra

up to  $z = 4$  due to increasing effects of IGM beyond this redshift. We identify bad cases by looking for differences between the peak wavelength of the zELDA models and our fitted analytic Ly $\alpha$  profiles larger than  $3\times$  the uncertainty in the analytic profiles' peak wavelengths, or zELDA models with reduced  $\chi^2 > 3.0$ . In such cases (274 out of 524) we discard the zELDA fit altogether.

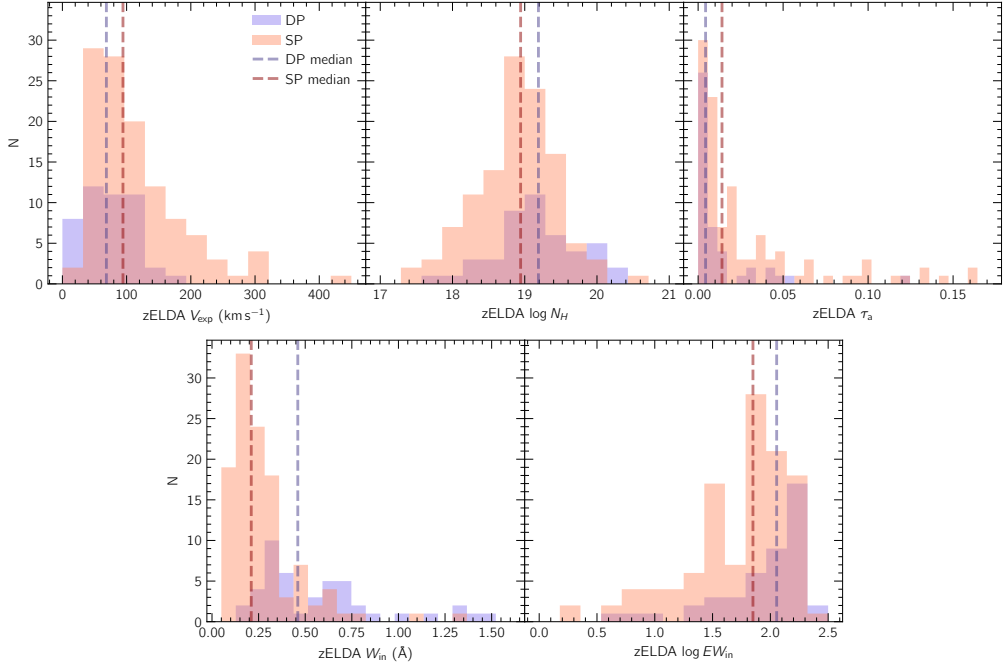


**Figure 3.21:** Comparison of zELDA expanding shell RT model parameters for single- vs double-peaked Ly $\alpha$  profiles.

We checked the accuracy of the zELDA estimates of  $z_{\text{sys}}$  by comparing them against the systemic redshift as measured using optically-thin emission lines. To perform this check, we selected only those systems with detections of at least one (unflagged) emission line at  $4\sigma$ . Figure 3.20 compares the redshift estimated from these emission lines,  $z_{\text{em}}$ , with that from zELDA in velocity space. In general, the differences between the two values are within  $3\sigma$  of zero; however, the higher-redshift sources tend towards less agreement, likely reflecting the limited redshift range over which the neural network was trained.

The zELDA models reveal how expanding-shell RT models might explain intrinsic differences between single- and double-peaked Ly $\alpha$  profiles. In Figure 3.21, we show a comparison of the zELDA model parameters in single- vs double-peaked cases. The most significant differences are in the dust optical depth,  $\tau_a$ , which is generally lower for double-peaked profiles, and the intrinsic Ly $\alpha$  width,  $W_{\text{in}}$ , which is generally higher. Less prominent, though still notable, differences can be seen in the expansion velocity,  $V_{\text{exp}}$ , which tends to be lower in double-peaked spectra, and the intrinsic Ly $\alpha$  equivalent width,  $EW_{\text{in}}$ , which tends to be somewhat higher. There is no clear difference in the neutral column density,  $N_H$ , suggesting that zELDA's neural network prefers low  $V_{\text{exp}}$

to explain the appearance of blue peaks rather than low  $N_H$ . We find no qualitative differences in these trends even when we exclude all sources with  $z > 4.0$  (i.e. those beyond the training range of the neural network). These trends show that simple expanding-shell RT models favor slower outflows with low dust content, as well as intrinsically broad and strong Ly $\alpha$  emission lines, to explain the appearance of blue Ly $\alpha$  peaks. This agrees at least partially with our spectral analysis, which suggests that blue peaks arise when outflows are slow and ionization is more intense. On the other hand, the expanding-shell models fail to reproduce the higher column densities in single-peaked sources suggested by the absorption profiles in Figures 3.16 and 3.17. We discuss this discrepancy further in Section 3.5.4.

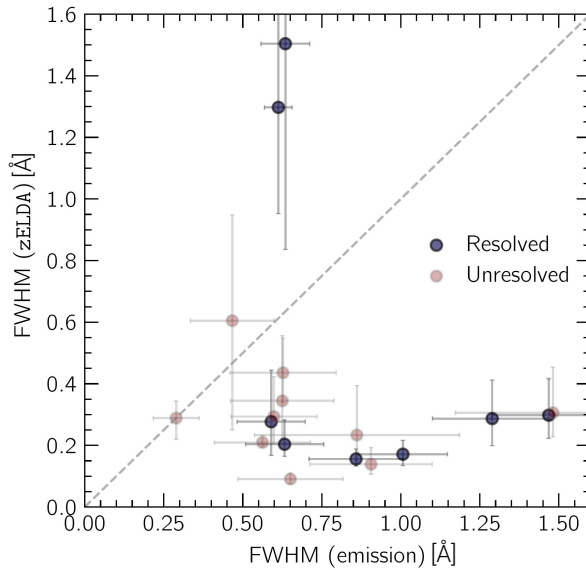


**Figure 3.22:** Comparison of zELDA estimated FWHM with that measured by emission lines.

To further assess the accuracy of the zELDA models, we compared the predicted intrinsic Ly $\alpha$  line widths against the (SNR-weighted) FWHM of emission lines from spectra where statistically significant emission was found as described in Section 3.4.2. Since the Ly $\alpha$  and metal emission lines originate from the same star-forming regions, their widths are likely closely related – if not the same – prior to radiative transfer effects through the surrounding ISM/CGM. Figure 3.22 shows a scatter plot of zELDA predicted intrinsic Ly $\alpha$  widths against measured metal emission line widths. Here, we have corrected for instrumental dispersion by obtaining the FWHM of the MUSE LSF at the observed wavelength using MPDAF’s built-in LSF models, and then computing the intrinsic width as  $W_{\text{int}} = \sqrt{W_{\text{obs}}^2 - W_{\text{LSF}}^2}$ . We find no statistically significant correlation between the zELDA predictions and the measured line widths; this may, in part, be due to the fact that some of the emission lines are poorly resolved; however, several of the emission line widths are comfortably in excess of the width of the MUSE LSF (i.e. by  $> 3\sigma$ ), and yet still show no relation with the widths predicted by zELDA. As a further

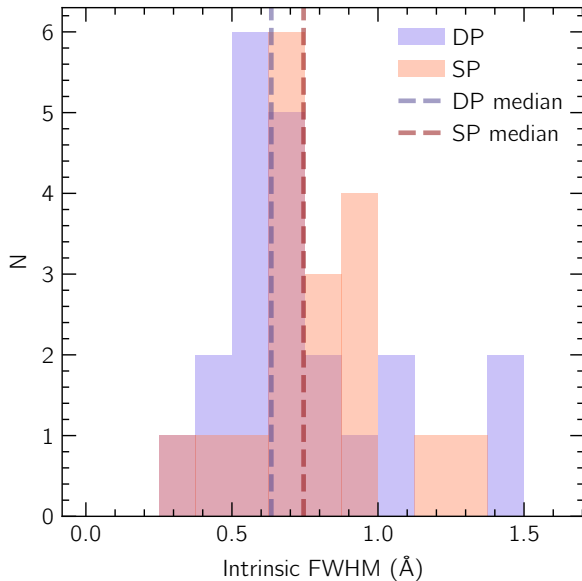


**Figure 3.23:** Comparison of estimated intrinsic emission line widths for single and double-peaked Ly $\alpha$  spectra, showing no clear difference in the distributions or, if anything, lower widths in double-peaked spectra.

check, we compared the distributions of intrinsic emission line widths for spectra with single- and double-peaked Ly $\alpha$  profiles, as shown in Figure 3.23, finding no evidence of larger line widths in double-peaked sources as predicted by zELDA. Taking the zELDA results at face value, this could argue against a common origin for the Ly $\alpha$  and other emission lines; however, we have seen in Section 3.4.2 that there is a clear relationship between the shape of the Ly $\alpha$  line and the strength of the emission lines. Instead, the disparity between the intrinsic line widths and zELDA’s predictions may reflect limitations inherent to the idealised expanding shell models on which zELDA’s neural network is trained.

## 3.5 Discussion

### 3.5.1 Origin of Emission Lines

The detection of emission lines from species with high ionization potentials (He II, C III, C IV, O III, Si III) points to extreme ionization conditions in these objects. To assess whether such emission lines can arise from H II regions, we compared our results with the photoionization models of Gutkin et al. (2016). These model grids cover a wide range in parameter space, including metallicities as low as  $\sim 0.07 Z_{\odot}$ , as well as various ionization parameters, dust-to-metal mass ratios, gas densities, C/O abundance ratios, and upper mass cutoffs of the stellar initial mass function (IMF). The incident ionizing spectra are single stellar population models from Bruzual and Charlot (2003)

**Table 3.2:** Representative emission line flux ratios. Rows correspond to dividends and columns to divisors. Each entry lists the corresponding ratio for the single-peaked stack above and the double-peaked stack below. Upper bounds, denoted <sup>u</sup>, are given for the N v $\lambda\lambda$ 1238, 1243 doublet, where there is no significant detection in the dividend flux, computed using 3 $\times$  its associated uncertainty.

	C IV	He II	O III	Si III	C III
N v	0.19 <sup>u</sup>	0.91 <sup>u</sup>	0.33 <sup>u</sup>	0.22 <sup>u</sup>	0.12 <sup>u</sup>
	0.24 <sup>u</sup>	0.63 <sup>u</sup>	0.48 <sup>u</sup>	0.77 <sup>u</sup>	0.20 <sup>u</sup>
C IV	–	4.70 $\pm$ 1.13	1.75 $\pm$ 0.34	1.13 $\pm$ 0.26	0.64 $\pm$ 0.12
	–	2.54 $\pm$ 0.20	1.96 $\pm$ 0.11	2.89 $\pm$ 0.42	0.82 $\pm$ 0.05
He II	0.21 $\pm$ 0.05	–	0.37 $\pm$ 0.07	0.24 $\pm$ 0.05	0.14 $\pm$ 0.02
	0.39 $\pm$ 0.03	–	0.77 $\pm$ 0.06	1.14 $\pm$ 0.18	0.33 $\pm$ 0.02
O III	0.57 $\pm$ 0.11	2.69 $\pm$ 0.49	–	0.65 $\pm$ 0.11	0.37 $\pm$ 0.04
	0.51 $\pm$ 0.03	1.30 $\pm$ 0.10	–	1.48 $\pm$ 0.22	0.42 $\pm$ 0.02
Si III	0.89 $\pm$ 0.21	4.16 $\pm$ 0.94	1.55 $\pm$ 0.27	–	0.57 $\pm$ 0.10
	0.35 $\pm$ 0.05	0.88 $\pm$ 0.14	0.68 $\pm$ 0.10	–	0.29 $\pm$ 0.04
C III	1.55 $\pm$ 0.30	7.30 $\pm$ 1.32	2.71 $\pm$ 0.30	1.75 $\pm$ 0.30	–
	1.21 $\pm$ 0.07	3.07 $\pm$ 0.23	2.37 $\pm$ 0.13	3.50 $\pm$ 0.51	–

with a range of ages and metallicities (assumed to be the same as the ISM metallicity). These models include intensities for all of the most prominent emission lines that we find: C III $\lambda\lambda$ 1907, 1909, C IV $\lambda\lambda$ 1548, 1551, Si III $\lambda\lambda$ 1883, 1892, He II $\lambda$ 1640, and O III $\lambda$ 1666, as well as the N v $\lambda\lambda$ 1238, 1243 line. We fit gaussian profiles to the stacked emission lines shown in Figure 3.19, and compute representative emission line ratios to compare against the photoionization model grids. We show these representative ratios in Table 3.2. In Figure 3.24, we compare a selection of line ratios against the photoionization models of Gutkin et al. (2016) as well as AGN Narrow Line Region (NLR) models produced by Feltre et al. (2016). The line ratios show a clear preference for stellar photoionization over AGN NLR, implying that the emission is dominated by H II regions. Moreover, the ratios of C III $\lambda\lambda$ 1907, 1909 to O III $\lambda$ 1666, and of Si III $\lambda\lambda$ 1883, 1892 to C III $\lambda\lambda$ 1907, 1909 are similar to measurements from H II regions in nearby metal-poor dwarf galaxies found by Garnett et al. (1995).

We also consider the possibility of more exotic mechanisms powering the emission lines, namely AGN and stellar winds from Very Massive Stars (VMSs) and Wolf-Rayet (WR) stars. Both of these can contribute broad line components to, especially, the He II $\lambda$ 1640 line (Martins et al., 2023; Feltre et al., 2016; Mingozi et al., 2024). For instance, Vanzella et al. (2020) argue for WR stars in the Sunburst Arc<sup>7</sup> on the basis of broad He II $\lambda$ 1640 emission ( $\text{FWHM} > 400 \text{ km s}^{-1}$ ) that is much broader than the C III $\lambda\lambda$ 1907, 1909, C IV $\lambda\lambda$ 1548, 1551, and O III $\lambda\lambda$ 1661, 1666 lines ( $\text{FWHM} < 50 \text{ km s}^{-1}$ ). We find no such extreme differences in line widths in our own sample, with the broadest He II $\lambda$ 1640 lines with  $\text{SNR} > 4$  having  $\text{FWHM} < 200 \text{ km s}^{-1}$  (i.e. well below the upper

<sup>7</sup>a highly magnified star-forming galaxy at  $z = 2.4$  that exhibits direct Ly $\alpha$  escape.

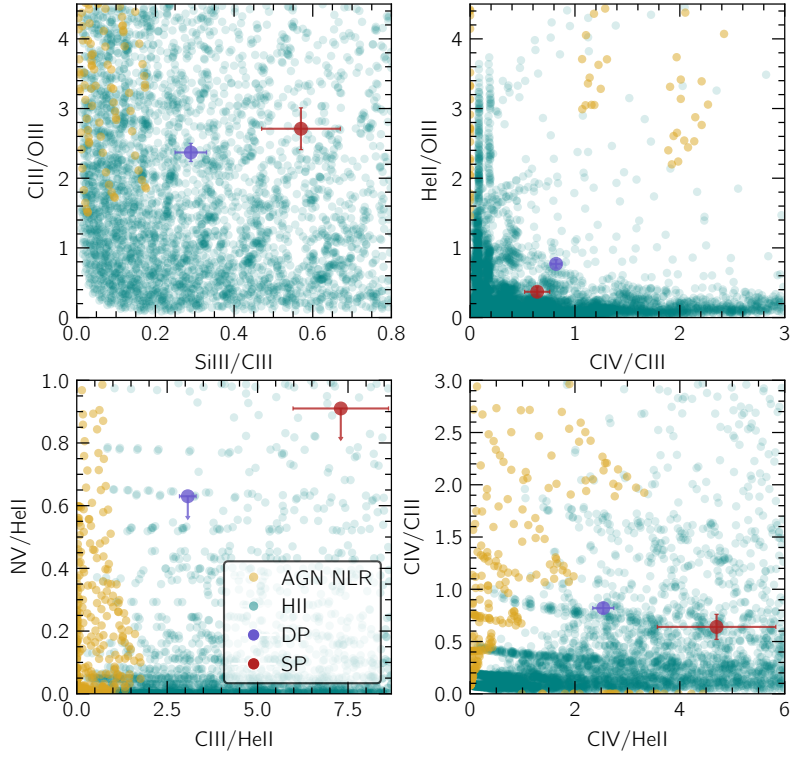


**Figure 3.24:** Measured stacked emission line ratios compared against stellar photoionization models (Gutkin et al., 2016) and AGN Narrow Line Region emission models (Feltre et al., 2016). The observed ratios show a clear preference for the stellar photoionization models, with no need to invoke AGN.

bound that we set for emission and absorption lines when fitting models as described in Section 3.3.3). On this basis, as well as the consistency with aforementioned photoionization models, we do not consider AGN or stellar winds from VMSs or WR stars necessary to explain the stacked spectra. However, this does not allow us to rule out significant contributions of AGN, VMSs or WR stars to the spectra of individual objects.

### 3.5.2 Origin of Absorption Lines

The low-ionization absorption lines that we include in our stacked absorption spectra shown in Figure 3.16 ( $\text{Si II}\lambda 1260$  and  $\text{C II}\lambda 1334$ ) are usually associated with predominantly neutral gas ( $< 10^4$  K) owing to their similar ionization potential to  $\text{H I}$  (see, e.g., Shapley et al. 2003, Chisholm et al. 2016, Berry et al. 2012). Studies of Lyman break galaxies (LBGs) have shown such lines to be weaker in less massive, more compact galaxies with higher  $\text{Ly}\alpha$  EW (Shapley et al., 2003; Jones et al., 2012). This is consistent with one of the trends that we find in our sample, namely that absorption is weaker in double-peaked systems, which in turn tend to have higher  $\text{Ly}\alpha$  EW. In addition to the low-ionization absorption lines, we also find absorption from high-ionization species:  $\text{Si IV}$  and  $\text{C IV}$  (the latter in P Cygni profiles alongside emission in stacked spectra from

single-peaked sources; see Figure 3.19).

Ratios between absorption lines of the same ionic species can be used to probe the structure of the outflowing gas. If the gas is optically thin, then the line ratios reflect the oscillator strengths of the respective lines; on the other hand, if the gas is optically thick but with limited covering fraction (i.e. clumpy), then the lines are saturated and the line ratios approach unity. Using this method, Berry et al. (2012) find evidence that high-ionization absorption lines in LBGs are optically thin, based on line ratios of the Si IV  $\lambda\lambda 1394, 1403$  doublet,  $\text{EW}(\text{SiIV}1394)/\text{EW}(\text{SiIV}1403) \sim 2.0$ , which is approximately the same as the ratio of oscillator strengths. This contrasts with the low-ionization lines which are generally found to be optically thick (Shapley et al., 2003; Berry et al., 2012; Jones et al., 2012). In our own stacked spectrum from single-peaked Ly $\alpha$  emitters, shown in Figure 3.17, by fitting gaussian profiles we find a ratio between the Si IV  $\lambda\lambda 1394, 1403$  doublet of  $0.87 \pm 0.18$ , i.e. consistent with the optically thick rather than optically thin regime (for the double-peaked stacks, the absorption lines are too weak to make any precise assessment of the optical thickness of the absorption). This ratio suggests that the high-ionization absorption may arise from optically thick clumps. We find a similar result for the Si II  $\lambda 1260$  and Si II  $\lambda 1527$  lines in the single-peaked stack, with the ratio in equivalent widths being:  $\text{EW}(\text{SiII}1260)/\text{EW}(\text{SiII}1527) = 1.40 \pm 0.27$ . These results paint a picture of clumpy multiphase outflows, with the clumps occupying a range of ionization states.

### 3.5.3 Origins of blue Ly $\alpha$ peaks

The comparative weakness of the blueshifted interstellar absorption lines in spectra with blue Ly $\alpha$  peaks has been suggested to arise from lower neutral covering fractions due to more powerful feedback creating ionized channels in the surrounding ISM (see Erb 2015 and references therein). In our own spectra, we find the same result to hold for low-ionization absorption lines, but also find that it holds for high-ionization species, suggesting that the appearance of blue Ly $\alpha$  peaks is associated with more gas-poor environments in general, as opposed to merely a higher ionization state. On the other hand, we note that the maximum depth of the stacked absorption lines in Figure 3.17 (as a fraction of continuum) is generally consistent between the single- and double-peaked stacks. The major difference instead appears to be the greater widths of the lines in the single-peaked stacks, which are systematically higher by a factor of  $\sim 3$ . This difference in line width can be seen even more clearly in the stacked low-ionization lines in Figure 3.16. If the absorption is optically thick, in which case the fractional absorption depth reflects the neutral covering fraction, then the appearance of blue Ly $\alpha$  peaks may be due to lower covering fractions *specifically at highly blueshifted velocities*, rather than lower neutral covering fractions across all velocities as suggested in Erb (2015). The simplest explanation for this is that systems with blue Ly $\alpha$  peaks host slower outflows, consistent with the RT models of, for instance, Verhamme et al. (2006).

We find a clear association between double-peaks and emission line EW, suggesting that whatever conditions favor strong emission lines also favor the appearance of blue Ly $\alpha$  peaks. Assuming these emission lines originate predominantly from H II regions as discussed in Section 3.5.1, this suggests a more intense ionization field in galaxies with blue Ly $\alpha$  peaks. Thus we arrive at the seemingly paradoxical conclusion that double-peaked sources have more intense ionization fields, yet drive slower outflows. A possible resolution of this paradox is that double-peaked Ly $\alpha$  profiles may arise from less massive systems with lower metallicity (two properties that are well known to be correlated; see, e.g., Curti et al. 2020). Low-mass, metal-poor systems may experience overall less powerful stellar feedback (driving slower outflows), be associated with less gas-rich environments (thus having weaker absorption), and yet also host a greater fraction of very massive stars and thus have stronger ionization fields (i.e. they may have top-heavy IMFs due to their low metallicity, see Li et al. 2023).

### 3.5.4 Comparison with expanding shell models

In light of the discussion of the emission and absorption features presented in Sections 3.5.1 and 3.5.2, the expanding shell models produced by zELDA appear to have met with mixed success. On the one hand, as discussed in Section 3.5.4, the best-fit intrinsic line widths found by zELDA do not appear to match the measured widths of the emission lines, nor even to scale with them in any discernable way (though the sample size is small), as shown in Figure 3.22. Moreover, we do not find that double-peaked Ly $\alpha$  lines tend to have higher intrinsic emission line widths than single-peaked ones as predicted by the expanding shell models as shown in Figure 3.21. Furthermore, the greater EW of low-ionization absorption lines in single-peaked spectra suggests higher (velocity-integrated) neutral covering fractions, which is not reflected in the integrated H I column densities of the expanding shell models. On the other hand, we find evidence that single-peaked Ly $\alpha$  lines may be associated with faster outflows, as inferred from comparatively broad low- and high-ionization absorption lines. This trend is in qualitative agreement with the trend in expansion velocities inferred by zELDA, shown in Figure 3.21.

The major problem faced by these expanding shell RT models may be clumpiness, which is not currently included in the grids used by zELDA. As discussed in Section 3.5.2, the absorption lines in both high- and low-ionization species are consistent with absorption in optically thick clumps rather than the homogeneous medium used in the zELDA model grids. Moreover, Duval et al. (2014) show that clumpy outflows may facilitate the escape of blueshifted Ly $\alpha$  photons. This may be why zELDA tends to predict extreme intrinsic Ly $\alpha$  line widths for double-peaked profiles, despite there being no evidence for such increased line widths based on metal emission lines. Incorporating clumpiness into model grids may be crucial to inferring outflow properties using tools such as zELDA.

### 3.6 Summary and Conclusion

We analysed the spectra of gravitationally-lensed Ly $\alpha$  emitters spectroscopically identified by R21. We fitted analytic profiles to the Ly $\alpha$  lines as well as a number of rest-frame UV metal emission and absorption lines from both high- and low-ionization species. We then generated stacks of these emission and absorption lines from spectra with and without detected blue Ly $\alpha$  peaks. We find that

- These Ly $\alpha$ -emitting sources show spectral signatures that are consistent with expectations of expanding shell models and hence outflows. Ly $\alpha$  peaks are red-shifted relative to the systemic velocity as measured using metal emission lines, or, when there is also a blue peak, the two peaks straddle the systemic.
- Both low- and high-ionization absorption lines may be saturated, suggesting that the outflows consist of optically thick clumps.
- Sources with double-peaked Ly $\alpha$  lines have weaker low- and high-ionization absorption lines relative to those with single-peaks, suggesting they are associated with more gas-poor environments both in the neutral and ionized phases.
- Stacked spectra of double-peaked sources show systematically smaller line widths than those of single-peaked sources, suggesting that the latter drive faster outflows, in agreement with radiative transfer expanding shell models.
- Double-peaked sources tend to have higher EW in high-ionization emission lines, suggesting harder ionization fields. This is consistent with a picture in which low-mass metal poor systems with top-heavy IMFs experience less powerful feedback.
- Though the qualitative agreement with expanding shell RT models is good, these models may over-state the importance of the intrinsic Ly $\alpha$  line width on the appearance of blue peaks. This suggests that results from fitting such simple models should be taken with a grain of salt without independent measurements of the intrinsic line widths from optically thin nebular emission lines.

### 3.7 Acknowledgments

J.L. and J.N. acknowledge support from the Research Grants Council of Hong Kong for conducting this work under the General Research Fund 17312122.

### 3.8 APPENDIX

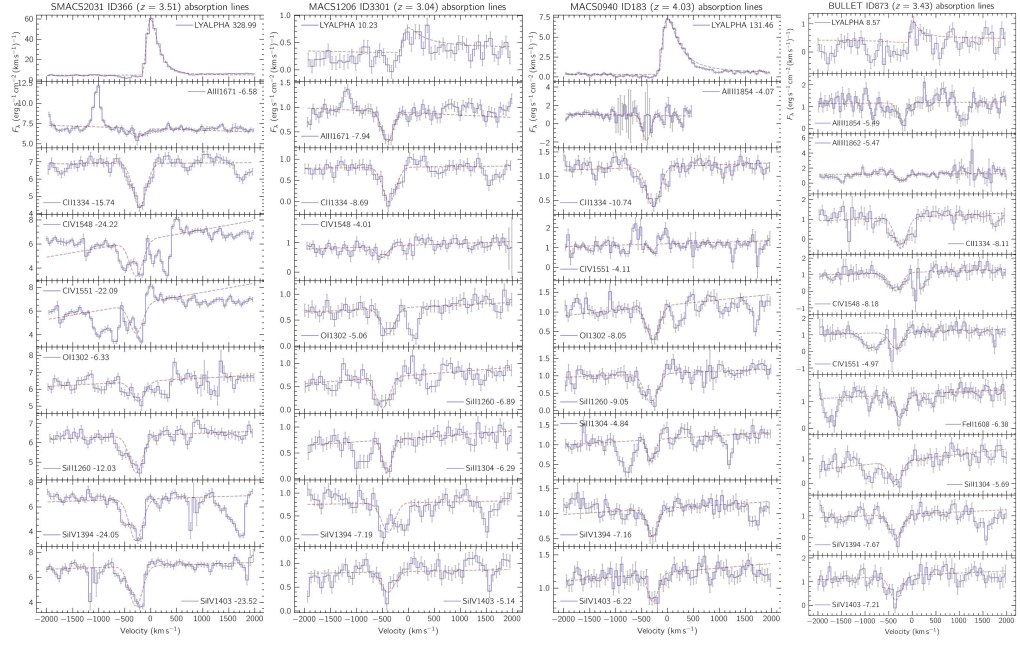


**Figure A.1:** Spectra with unambiguous absorption lines (part 1 of 2)

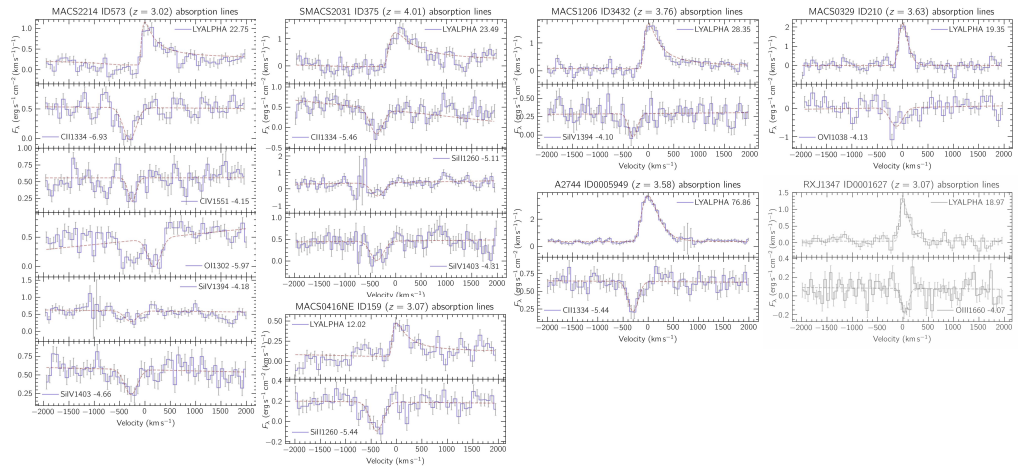


**Figure A.2:** Spectra with unambiguous absorption lines (part 2 of 2)



## Chapter 4

# **Star Formation History of a Faint Lyman- $\alpha$ Source**

The following chapter is drawn from a paper currently in preparation for submission to *The Astrophysical Journal* entitled "Rejuvenation of an isolated compact galaxy in the early universe" by James Nianias, Jeremy Lim, and Sung Kei Li. The entire paper – including all figures and writing – has been prepared by me. I also performed all data analysis, except for generating the lensing critical curve shown in Figure 4.2, which was performed by S.K.L.. Additional explanatory figures and footnotes have been included for the purpose of this thesis.

## Abstract

Lyman- $\alpha$ -emitting galaxies in the early universe are characterised by low to intermediate stellar masses ( $\sim 10^6 - 10^9 M_\odot$ ) and high specific star formation rates (above the main sequence). Studies of gravitationally-lensed LAEs, primarily utilizing rest-frame UV imaging, have found some of these objects to be extremely compact, with sizes constrained to as small as a few tens of pc or less, and young, with ages as low as just a few Myr. Are we witnessing initial bursts of star formation as gas accretes into a parent halo (primeval galaxies) or are they established galaxies undergoing rejuvenation, similar to LAEs in the local universe? Here, we utilise JWST NIRCam imaging to investigate the spatially-resolved star formation history of one of the most highly magnified ( $\mu \approx 70$ ) young (age  $< 10$  Myr), and UV-compact LAEs behind the Hubble Frontier Fields galaxy cluster MACS J0416.1-2403. Comparing short- and long-wavelength stacked HST/JWST images, we show that the morphology in rest-frame NIR is significantly different to rest-frame UV, suggesting differences in the stellar populations in different parts of the source. We then extract multiple spatially-resolved SEDs from across the lensed image of the source, and perform stellar population modelling. In addition to the previously known young stellar population, we find evidence for a hitherto undetected older stellar population in this source, with an age possibly as old as  $\sim 1$  Gyr. We consider a simple mechanism of rejuvenation in which metal-enriched gas is accreted from the CGM to fuel the young stellar population.

### 4.1 Introduction

In the standard cold dark matter (CDM) paradigm, massive galaxies grow in large part hierarchically, that is, by mergers of less massive galaxies over the course of cosmic history (e.g. [Santistevan et al. 2020](#)). Consequently, understanding star formation in low-mass galaxies at early epochs is crucial to understanding galaxy evolution as a whole. One of the most effective ways to detect low-mass star-forming galaxies in the early universe is via Lyman- $\alpha$  (Ly $\alpha$ ) emission. As Ly $\alpha$  photons are produced in great abundance in H II regions surrounding young stars, the emergent Ly $\alpha$  line can have equivalent width  $> 100$  Å, making it easily detectable with blind spectroscopy ([Feltre et al., 2020](#); [Claeyssens et al., 2022](#)) and narrowband imaging ([Ouchi et al., 2010](#)) even for galaxies that are too faint to be detected by their stellar continuum. Furthermore, Ly $\alpha$  is easily identifiable via spectroscopy due to its characteristic asymmetric shape, which

arises from scattering of Ly $\alpha$  photons from outflowing (or, more rarely, inflowing) gas (Ahn, 2004; Verhamme et al., 2006; Orsi et al., 2012; Blaizot et al., 2023). When Ly $\alpha$ -emitting galaxies (LAEs) are sufficiently luminous in the continuum, it is also possible to study their stellar properties via broadband photometry. Studies that fit models to the spectral energy distributions (SEDs) of LAEs at high  $z$  generally find them to be well characterised by low-to-intermediate masses ( $10^7 M_\odot - 10^{10} M_\odot$ ), low dust extinction, subsolar metallicity and, unsurprisingly, ongoing star formation (Finkelstein et al., 2009; Hagen et al., 2014; Iani et al., 2024). On the other hand, the same studies find that LAEs fall into two categories in terms of the maximum ages of their stellar populations: either they are composed entirely of young stars, with ages  $\lesssim 10$  Myr, or they include much older stars (in addition to the young stars powering the Ly $\alpha$  emission) with ages  $\gtrsim 100$  Myr. This bimodality has led some to suggest that some LAEs may be primaeval galaxies experiencing their first episodes of significant star formation, while others may be older objects experiencing rejuvenation (e.g. Shimizu and Umemura 2010; Rosani et al. 2020; Iani et al. 2024).

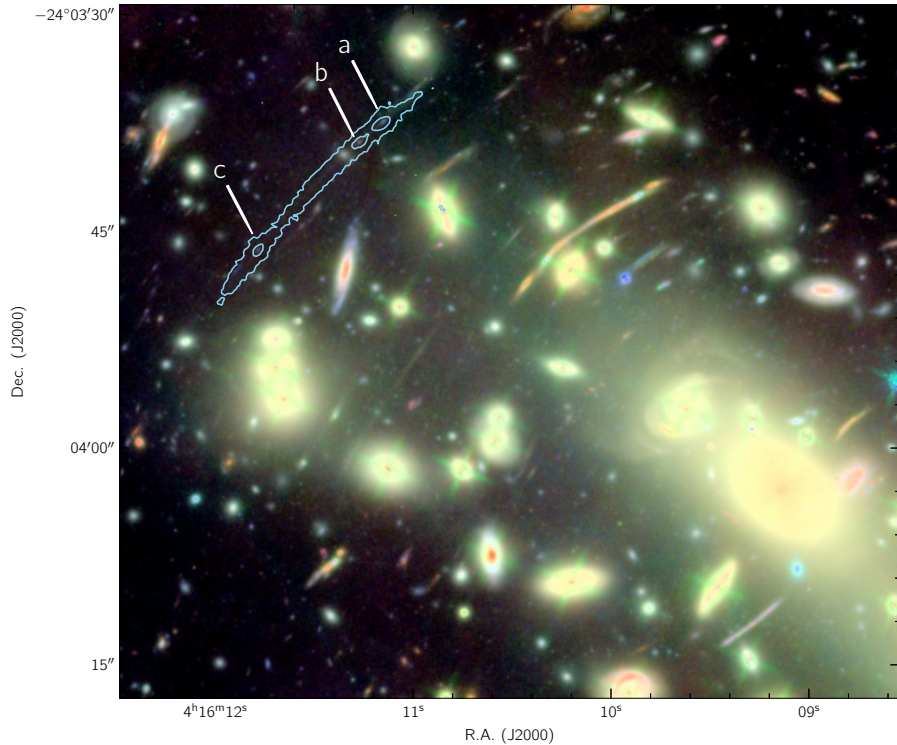


**Figure 4.1:** RGB image of MACS0416 composed of HST ACS/WFC and JWST NIRCam images, overlaid with the MUSE Ly $\alpha$  contours of LAE3.24 (light blue). Three lensed counterimages – labelled **a**, **b**, and **c**, in descending order of relative brightness – are visible as both Ly $\alpha$  and continuum peaks.

When LAEs are magnified by gravitational lensing by foreground galaxy clusters, it becomes possible to study in detail those that would otherwise be detected only marginally or not at all, as well as to spatially resolve their structure. Hundreds of

such lensed LAEs at  $2.9 < z < 6.7$  have been found via integral field spectroscopy with the Multi-Unit Spectroscopic Explorer (Richard et al., 2021). Studies of these objects – which can be magnified by up to a factor of  $\sim 100$  – in rest-frame UV using the Hubble Space Telescope (HST) find that in some cases the UV continuum counterparts are extremely compact, on the order of 10 pc – 100 pc (Claeyssens et al., 2022), while stellar masses can be as low as just  $\sim 10^5 M_\odot$  (Meštrić et al., 2022). Are these compact sources primaeval single stellar populations, or are they rejuvenated objects that play host to multiple generations of stars? Thanks to the enhanced wavelength coverage provided by the James Webb Space Telescope (JWST), it is now possible to shed light on this question by performing stellar population synthesis modelling encompassing rest-frame optical/near-infrared (NIR). Here, we perform spatially-resolved SED fitting of an extremely magnified ( $\mu \sim 70$ ) LAE at  $z = 3.236$  (LAE3.24 henceforth) behind the lensing galaxy cluster MACS J0416.1-2403 (MACS0416 henceforth) using JWST in conjunction with HST imaging. This source was included in a previous study by Vanzella et al. (2017), who estimated a stellar mass of  $\sim 10^6 M_\odot$  and effective radius between  $\sim 45$  pc and  $\sim 80$  pc using HST observations (in conjunction with NIR observations in three bands, though these had much lower signal-to-noise ratios).

In Section 4.2 we describe the observations that we use, as well as our alignment and PSF-matching routines. Next, we discuss differences in the source morphology as it appears in rest-frame NIR versus UV in Section 4.3.1. We describe the process of extracting SEDs from across the source in Section 4.3.2, and the SED fitting and results in Section 4.3.3, which show evidence for an underlying old stellar population. In Section 4.4, we discuss the implications of this older stellar population for the evolution of LAE3.24, as well as for the star formation histories of compact high- $z$  galaxies generally.

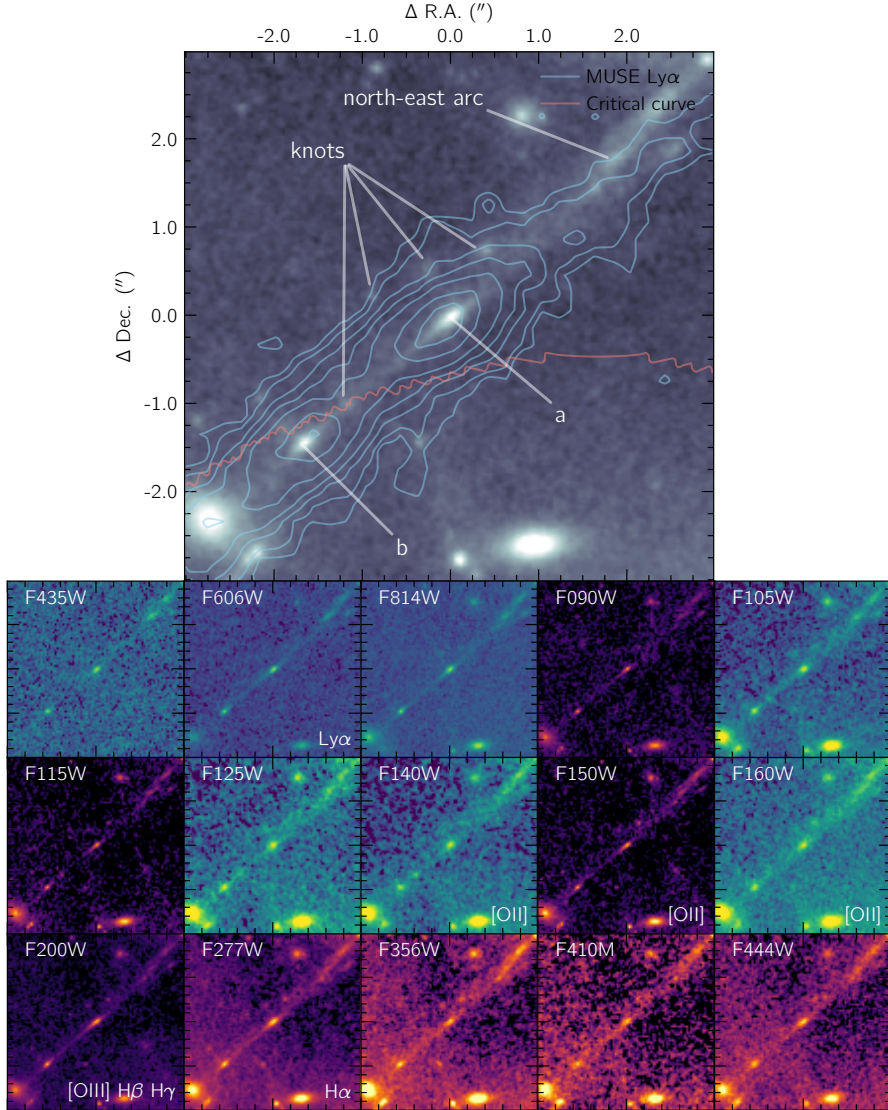
This work adopts a flat  $\Lambda$ CDM cosmology with  $H_0 = 68 \text{ km s}^{-1} \text{ Mpc}^{-1}$  and  $\Omega_M = 0.31$  (Planck Collaboration et al., 2014).

## 4.2 Archival Observations and Data Reduction

We obtained JWST NIRCam images of MACS0416 from the *Prime Extragalactic Areas for Reionization and Lensing Science* (PEARLS) collaboration (Windhorst et al., 2023). NIRCam provides wavelength coverage from rest-frame UV in the shortest-wavelength filter (F090W, extending down to  $\sim 1900 \text{ \AA}$  at the redshift of the target) to rest-frame NIR in the longest wavelength filter (F444W, extending up to  $\sim 11800 \text{ \AA}$ ). We combined these images with archival HST ACS and WFC3 images from the Hubble Frontier Fields (HFF) program<sup>1</sup> (Lotz et al., 2017), with the ACS filters providing rest-frame UV coverage down to  $\sim 900 \text{ \AA}$  and the WFC3 filters providing rest-frame UV/optical coverage up to  $\sim 4000 \text{ \AA}$ . Table 4.1 provides a list of filters along with exposure times,  $1\sigma$  sensitivities, and effective wavelengths in the rest frame of the target. In Figure 4.2, we show cutout images in each HST and JWST filter of LAE3.24 at native angular

<sup>1</sup>Obtained from <https://archive.stsci.edu/prepds/frontier/macs0416.html>

MACS0416 source P594: coord = (64.046462, -24.060399).  $z = 3.2356$ .  $\mu = 73.81$ .

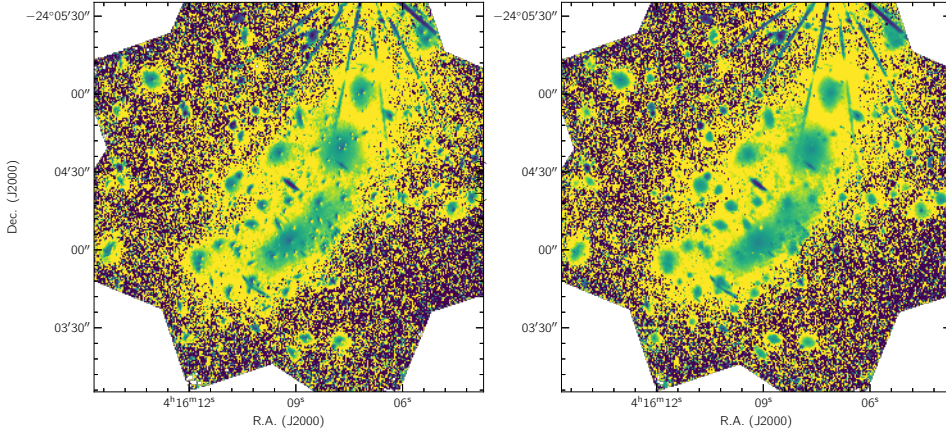


**Figure 4.2:**  $6'' \times 6''$  HST and JWST postage stamp images of the lensed arc LAE3.24. *Above:* Stacked image after PSF matching of all filters to a common resolution (slightly worse than the HST F125W filter), with MUSE Ly $\alpha$  contours in light blue, and lensing critical curve from Rihtaršič et al. (2024) in orange. The two knots visible along the arc, labelled **a** and **b**, are multiply-lensed counterimages of LAE3.24, with counterimage **a** having the greater brightness and size and therefore magnification. *Remaining panels:* HST (blue/yellow) and JWST (pink/orange) images at native angular resolution. Potentially strong emission lines are indicated for the relevant filters in the lower right of each panel.

resolution (lower panels) along with a stacked image using all filters after convolution to a common angular resolution (upper panel).

**Table 4.1:** Filters Used to Image the Target

Filter	Instrument	Program	$T$ (min)	Sensitivity (MJy)	$\lambda_{\text{eff}}^{\text{rest}}$ ( $\text{\AA}$ )
F435W	HST/ACS	HFF	909	$6.74 \times 10^{-16}$	1024
F606W	HST/ACS	HFF	558	$8.45 \times 10^{-16}$	1406
F814W	HST/ACS	HFF	2166	$7.65 \times 10^{-16}$	1905
F090W	JWST/NIRCam	PEARLS	100	$1.26 \times 10^{-15}$	2134
F105W	HST/WFC3	HFF	1122	$1.43 \times 10^{-15}$	2498
F115W	JWST/NIRCam	PEARLS	100	$1.40 \times 10^{-15}$	2730
F125W	HST/WFC3	HFF	551	$1.47 \times 10^{-15}$	2953
F140W	HST/WFC3	HFF	459	$1.37 \times 10^{-15}$	3296
F150W	JWST/NIRCam	PEARLS	100	$1.15 \times 10^{-15}$	3549
F160W	HST/WFC3	HFF	1102	$1.72 \times 10^{-15}$	3632
F200W	JWST/NIRCam	PEARLS	100	$1.48 \times 10^{-15}$	4701
F277W	JWST/NIRCam	PEARLS	100	$1.28 \times 10^{-15}$	6571
F356W	JWST/NIRCam	PEARLS	100	$9.70 \times 10^{-16}$	8433
F410M	JWST/NIRCam	PEARLS	100	$1.50 \times 10^{-15}$	9641
F444W	JWST/NIRCam	PEARLS	100	$1.35 \times 10^{-15}$	10414

**Figure 4.3:** Ratio of the HST F814W and JWST F444W images made before (left) and after (right) manual sub-pixel alignment (see text). The image on the left shows clear asymmetrical profiles around each bright source, all of which are oriented similarly, while the right shows no such pattern, indicating good alignment.

### 4.2.1 Alignment and PSF Matching

We aligned the HST and JWST images using `AstroAlign` (Beroiz et al., 2020), which uses 3-point asterisms common to two images to derive the coordinate transformation between them. Inspection of the resulting aligned images revealed excellent agreement between frames taken with the same instrument, but small residual offsets between images taken with different instruments (i.e. JWST/NIRCam, HST/ACS, and HST/WFC3), possibly due to their differing point-spread functions (PSFs). We eliminated these residual offsets by manually introducing sub-pixel corrections to the transformations produced by `AstroAlign`. We judged the quality of the alignment by taking the ratio of the two images being aligned. In Figure 4.3, we show an example of such a

ratio image made before and after sub-pixel alignment.

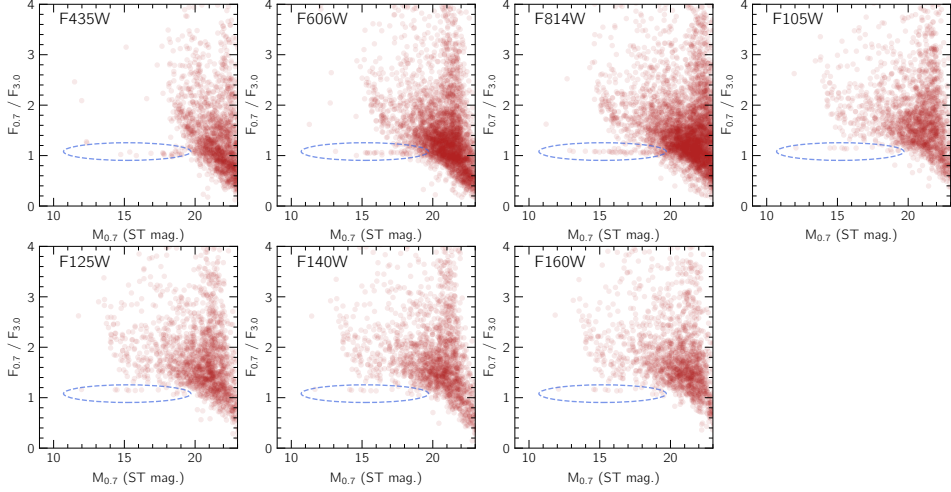


**Figure 4.4:** Ratios between total flux in small ( $0.7''$ ) and large ( $3.0''$ ) apertures for sources detected by SExtractor. Bright sources with flux ratios near unity, indicated with blue ellipses, are suitable candidates for stacking to generate empirical PSFs.

Following alignment, we performed PSF-matching of all images using empirical PSFs generated by stacking point-like sources in the images. Following Whitaker et al. (2019), we identified candidate point-like sources in the HST and JWST fields by running SExtractor (Bertin and Arnouts, 1996) twice, once with a small aperture of diameter  $0.7''$  and once with a larger aperture of diameter  $3.0''$ . We then identified point-like objects by looking for bright sources with flux ratios between the  $0.7''$  and  $3.0''$  apertures close to unity, as shown in the circled regions in Figure 4.4. We then generated  $5'' \times 5''$  postage stamp cutouts of these sources, and selected by eye those that were free of nearby contaminating objects, were unsaturated, and showed no obvious ellipticity. We up-sampled each postage stamp by a factor of 10, and then re-centered them on the same grid by fitting Moffat profiles to the inner part of each source to find their respective centers. We then took the median of these re-centered postage stamps (rather than the mean, which tends to result in a "noisy" PSF due to nearby contaminating sources), and then performed a background subtraction by fitting a 2D polynomial of degree one to the background of each PSF image after aggressively sigma-clipping to exclude the PSF core, wings, and diffraction spikes from the fit. We show the resulting PSFs in Figure 4.5.

We estimated the spatial resolution of each filter by fitting Moffat functions to the core of each of our empirical PSFs, finding the largest FWHM to be that of the HST WFC3 F125W filter. We then utilised the PSF-matching routines in the photutils Python library (Bradley et al., 2022) to generate convolution kernels to match each filter to the resolution of the F125W filter. photutils generates matching kernels using the ratio of Fourier transforms of the desired and original PSFs, which requires the use of a low-pass filter to remove high-frequency noise (see Aniano et al. 2011 for details). The

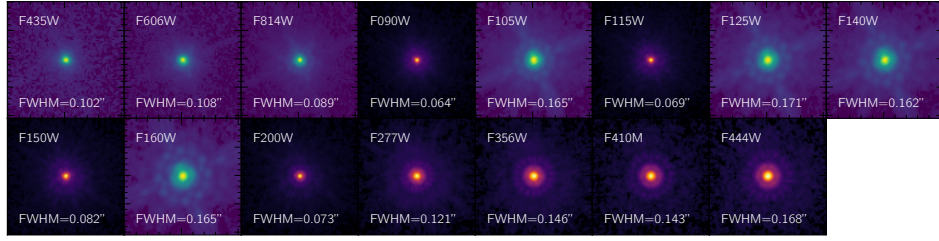


**Figure 4.5:** Empirical PSFs extracted from each image along with FWHM of Moffat profiles fitted to the PSF cores. The worst angular resolution belongs to the HST WFC3 filter F125W.

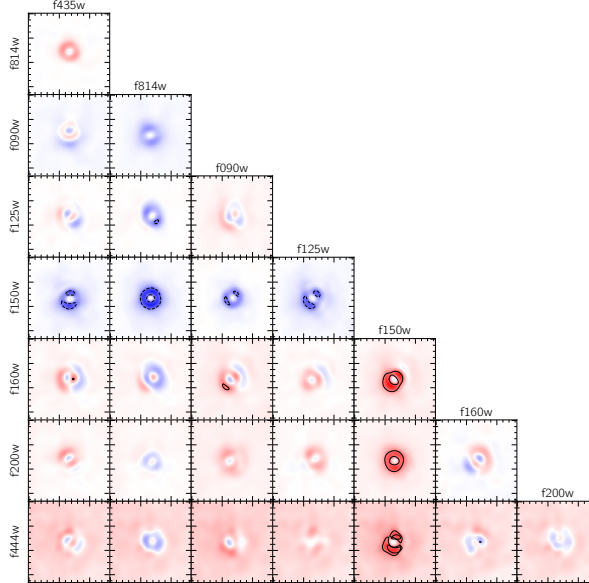


**Figure 4.6:** PSF residuals in selected filters. The  $(i, j)^{\text{th}}$  entry shows the result of subtracting the image of a bright star in the  $j^{\text{th}}$  from the  $i^{\text{th}}$  filter. Contours are at the  $\pm 1.5\%$ ,  $\pm 3\%$ , and  $\pm 5\%$  level of peak flux (no 5% contours are shown, indicating a good match between the PSFs).

drawback of this is that the low-pass filters can increase the FWHM of the resulting matched PSF. We experimented with a variety of different filters, finding that the best case left us with a final PSF free from artifacts and with a FWHM of  $\sim 0.24''$ . Though this is slightly worse than the resolution of the F125W filter ( $0.17''$ ), it does not compromise our ability to resolve the various features visible in the target source, as shown in the stacked PSF-matched image in Figure 4.2. Following convolution, we checked the final angular resolution of each image by scaling and subtracting images of the same bright star in different filters, finding the residuals to be no greater than  $\sim 2\%$  of peak flux in the worst cases, and no greater than 1% in the best cases, as shown in Figure 4.6. As an additional check, we also fitted Moffat profiles to the same test star and compared the FWHM, finding them to be very close (within 3%) in all cases.

## 4.3 Results and Analysis

### 4.3.1 Source morphology

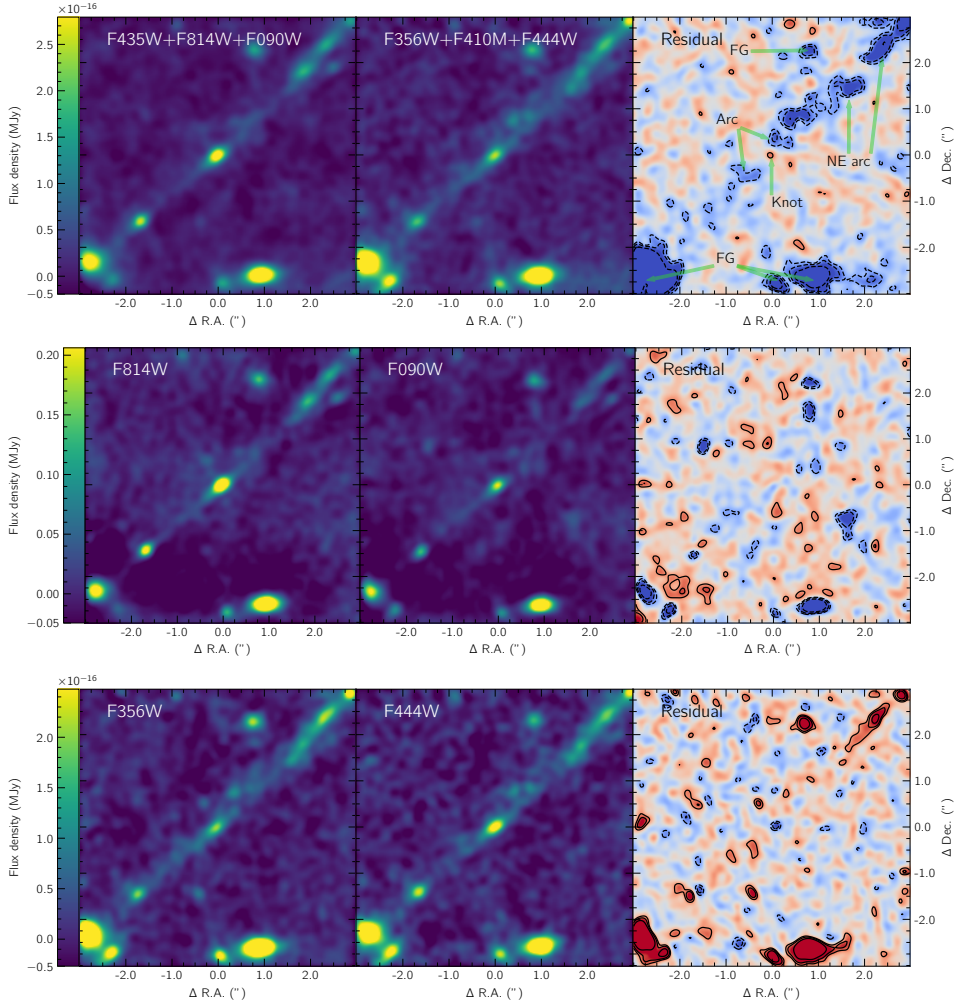


**Figure 4.7:** *Upper:* Comparison of rest-frame UV (left) and optical/NIR (middle) images of the target, along with residual image after scaling and subtracting the optical/NIR from the UV (right). Contours in the residual image are shown at the  $\pm 2\sigma$ ,  $\pm 3\sigma$ , and  $\pm 5$  levels. Clearly visible are over-subtracted regions along the arc either side of the bright knot. Also visible are deeper over-subtracted regions along the arc to the north-east of the bright central knot. FG denotes foreground objects. *Middle/Lower:* The same plots, now comparing adjacent filters: F814W - F090W (both rest-frame UV) and F356W - F444W (both rest-frame optical/NIR). Both cases show no significant residuals, showing that systematics are unlikely cause the residual features seen in the UV - optical/NIR image above.

As shown in Figure 4.2, the image of LAE3.24 is distorted into an arc-like shape due to strong gravitational lensing by the foreground galaxy cluster. To better understand qualitatively the geometry of a lensed source, it is helpful to compare against a model of the lensing potential of the foreground cluster, also known as a lens model. To do

this, we used one of the most recent lens models for MACS0416, that of Rihtaršić et al. (2024), which uses 303 multiply-lensed images from 111 sources with high-confidence spectroscopic redshifts, including images **a**, **b**, and **c** of LAE3.24. We checked the suitability of this model for understanding images **a** and **b** of LAE3.24 by plotting the critical curve (CC), the locus of points in the image plane for which the magnification approaches infinity for a background point source. For sources that are lensed into multiple counterimages, the CC is also the line about which pairs of counterimages can be seen: one counterpart outside the CC, and one inverted counterpart within the CC. This can be clearly seen in the case of LAE3.24 as shown in the upper panel of Figure 4.2: the brighter counterpart, counterimage **a**, lies outside the CC, while the dimmer, counterimage **b**, lies within it. The inversion of the inner counterpart means that the arc pointing away from counterimage **b** towards the CC (to the North-East) corresponds to the arc pointing away from counterimage **a** towards the CC (to the South-West). While this lens model serves as a useful way to qualitatively understand the appearance of the lensed images of LAE3.24, the precise locus of the CC it provides is likely not accurate, as it shows counterimage **b** closer to the CC than counterimage **a**, which would ordinarily imply that **b** had the greater magnification. This conflicts with the observed relative brightnesses and sizes of the two counterimages, which clearly show that **a** has the greater magnification. For this reason, we use the model of Rihtaršić et al. (2024) purely for illustrative purposes.

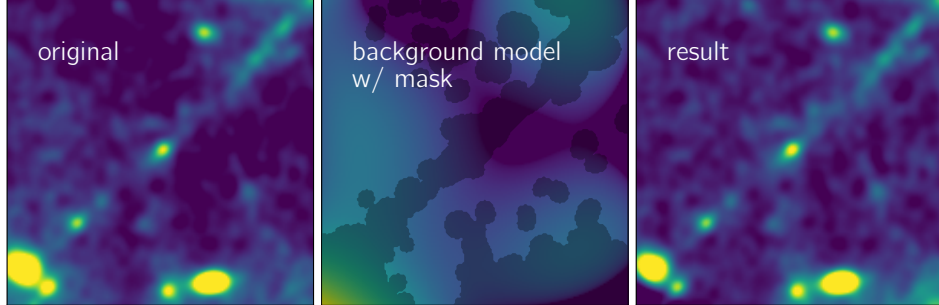


**Figure 4.8:** Example of polynomial background subtraction applied to the JWST F115W filter. *Left:* Original image with no background subtraction. *Center:* Fitted 2D polynomial (of degree five) including the mask used to avoid sources (generated using four rounds of sigma clipping at the 2.2 sigma level). *Right:* background-subtracted image, showing much flatter background around the target.

Aside from the main lensed arc, a number of other features can be seen. These include three compact knots just north of the bright knot of counterimage **a**, indicated in Figure 4.2. These are most noticeable in filters F150W – F356W, corresponding to the rest-frame optical at the redshift of LAE3.24. A similar knot-like feature can be seen along the arc between counterimage **b** and **a**, most noticeable in the F140W filter. As we show in Section 4.3.3, these knots are likely associated with MACS0416 and not LAE3.24. Finally, there is a clumpy extended structure that appears to be an extension of the main arc to the North-East of the main knot of counterimage **a**. This is labelled

*NE arc* in Figure 4.2. This structure has been spectroscopically identified as a lensed intermediate-redshift object at  $z = 2.41$  by Vanzella et al. (2023). We show in Section 4.3.3 that the faint diffuse emission running between counterimage **a** and the NE arc is more likely to be associated with the latter system.

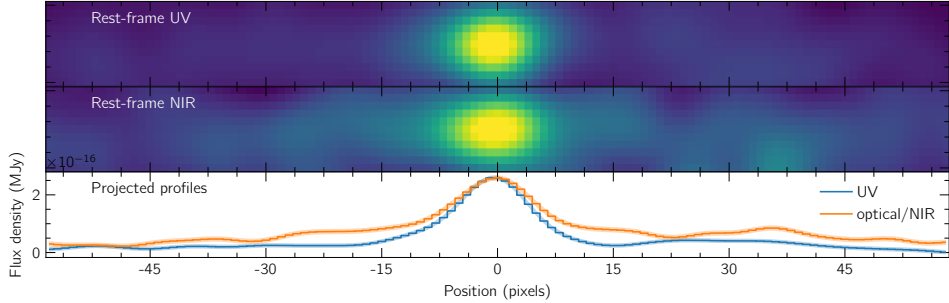


**Figure 4.9:** Comparison of cuts taken along the arc. *Upper*: the arc in rest-frame UV. *Middle*: the arc in rest-frame NIR. *Lower*: 1D projected profiles normalised to the same peak level. The region to the left of the bright knot between  $-45$  and  $+30$  is free from contaminating objects, yet shows a clear elevation in the rest-frame NIR relative to the UV, suggestive of a genuine morphological difference.

As an initial test to search for signs of an older stellar population, we look for differences between the rest-frame UV and optical/NIR morphology. Figure 4.7 shows a comparison between a composite rest-frame UV image made by stacking the HST/ACS F435W and F814W filters with the JWST/NIRCam F090W filter (left panel), and a rest-frame optical/NIR image made with the JWST/NIRCam F356W, F410M, and F444W filters (centre panel). In this case, all images have been convolved to the resolution of the JWST/NIRCam F444W filter (which has the worst angular resolution of this set of filters) prior to stacking following the same PSF-matching procedure outlined in Section 4.2.1. These filters were selected to avoid the brightest emission lines that may affect the surface brightness distribution of the lensed image: Ly $\alpha$ , [O II] $\lambda\lambda 3726, 3729$ , H $\delta$ , H $\gamma$ , H $\beta$ , [O III] $\lambda\lambda 4959, 5007$ , and H $\alpha$ . We subtracted the backgrounds of each image by masking the target and foreground galaxies using sigma-clipping and then fitting and subtracting a 2D polynomial of degree five; we show a representative example of this in Figure 4.8. We then normalised the optical/NIR image to match the UV image using a least-squares fitting routine to find the optimal scaling factor within a circular region of radius  $0.6''$  centered on the bright central knot of the image. In the right panel of Figure 4.7, we show the residual image after subtracting the scaled optical/NIR image from the UV. Significant residual features can be seen along the arc either side of the bright central knot (as well as further along the arc to the North-East). We experimented by manually adjusting the scaling factor as well as the background levels in the images, finding that no combination of these factors resulted in a subtracted image in which the knot and adjacent arc were free from significant residuals, suggesting a genuine difference in morphology. Specifically, the source appears to be more concentrated at the bright knot in the UV, while in the optical/NIR it is more evenly distributed along the arc. This is more easily visualised by taking cuts along the arc and comparing

the rest-frame UV and NIR, as shown in Figure 4.9. To check whether such residual features could be caused by systematics associated with the alignment, PSF matching, or background subtraction, we also performed the same subtraction on adjacent filters (F184W - F090W and F356W - F444W). As shown in the middle and lower rows of Figure 4.7, no significant residuals can be seen in either of these cases, showing that the difference between the UV and optical/NIR morphology is likely genuine.

### 4.3.2 SED Extraction

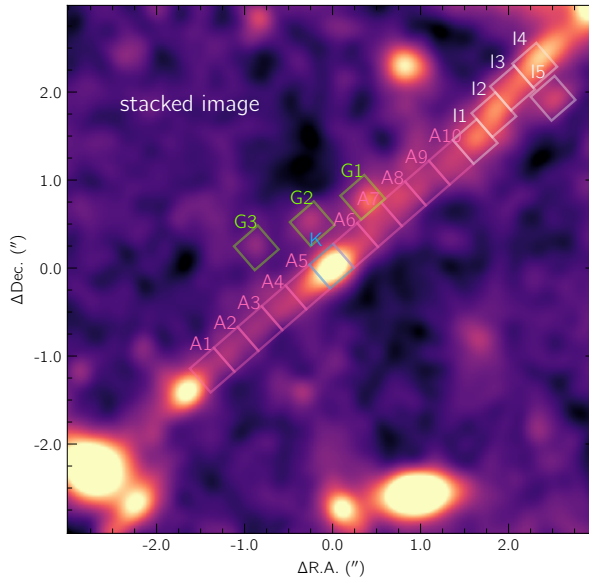


**Figure 4.10:** Apertures used to extract SEDs.

To understand what differences in stellar properties, star formation histories, nebular emission, and/or dust extinction could give rise to the differences observed between the UV and NIR morphology of LAE3.24, we conducted spatially-resolved stellar population modelling. We placed 19 apertures of size  $0.36'' \times 0.36''$  at various positions across the source as shown in Figure 4.10. We color-code these apertures based on the feature or features they pick out: blue (aperture K) for the bright knot, pink (apertures A1 – A10) for the main arc, and green (apertures G1 – G3) for three knots offset from the main arc that are especially bright in the rest-frame optical (see F150W, F200W, and F277W filters in Figure 4.2). We also placed apertures on the NE arc, which are shown in white (apertures I1 – I5). Although the NE arc has been identified as not associated with LAE3.24, these apertures serve as useful control cases by which we determine whether other features (especially those covered by apertures A6 – A10) are also part of, or affected by, the NE arc. When extracting the flux in each filter, we included a local background subtraction, where the background was estimated using rectangular boxes of size  $1.2'' \times 0.72''$  adjacent to each aperture and oriented parallel to the arc, an example of which is shown in Figure 4.11. We used a mask based on sigma-clipping to avoid contamination of the background estimate by the target or other nearby objects,

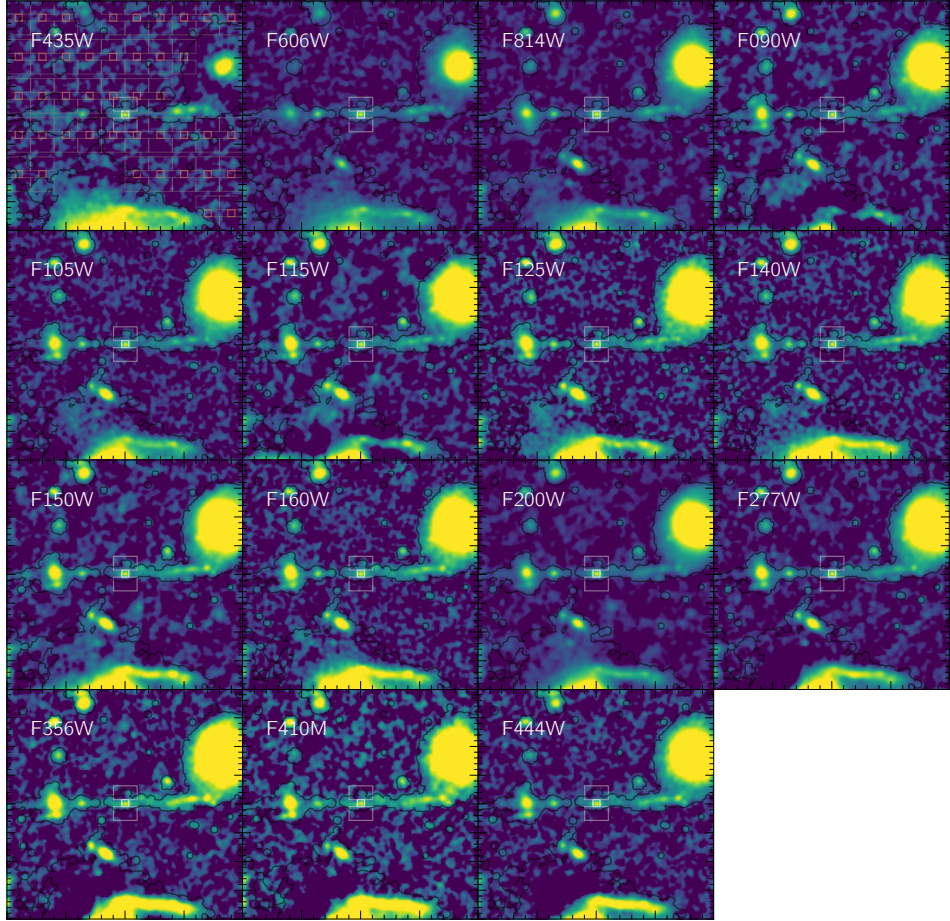


**Figure 4.11:** Aperture used to extract the SED from the central knot and rectangular boxes used for the local background estimation (white boxes in the center of each image), along with the mask used to exclude any contamination of the background estimates (black contour surrounding bright sources). Also shown in the first image (F435W) is the grid of identical apertures and background boxes used to derive uncertainties (red square apertures with grey background boxes). Note that the images have been rotated to align the arc along the horizontal axis for easier processing.

similar to the masks used when generating model backgrounds (see Section 4.3.1). We also generated uncertainties for each data point in the SEDs by placing 45 identical apertures and background boxes in a grid covering a  $12'' \times 12''$  region centered on the target, avoiding sources by rejecting any apertures for which more than 50% of pixels in the aperture or associated background boxes fall within the masked regions shown in Figure 4.11. In the left columns of Figures 4.12 and 4.13, we show all of the extracted SEDs along with best fit model spectra (see Section 4.3.3).

### 4.3.3 SED Fitting

We fitted the resulting SEDs using the Bayesian stellar population synthesis code `Bagpipes` (Carnall et al., 2018). We performed several rounds of fitting with models of

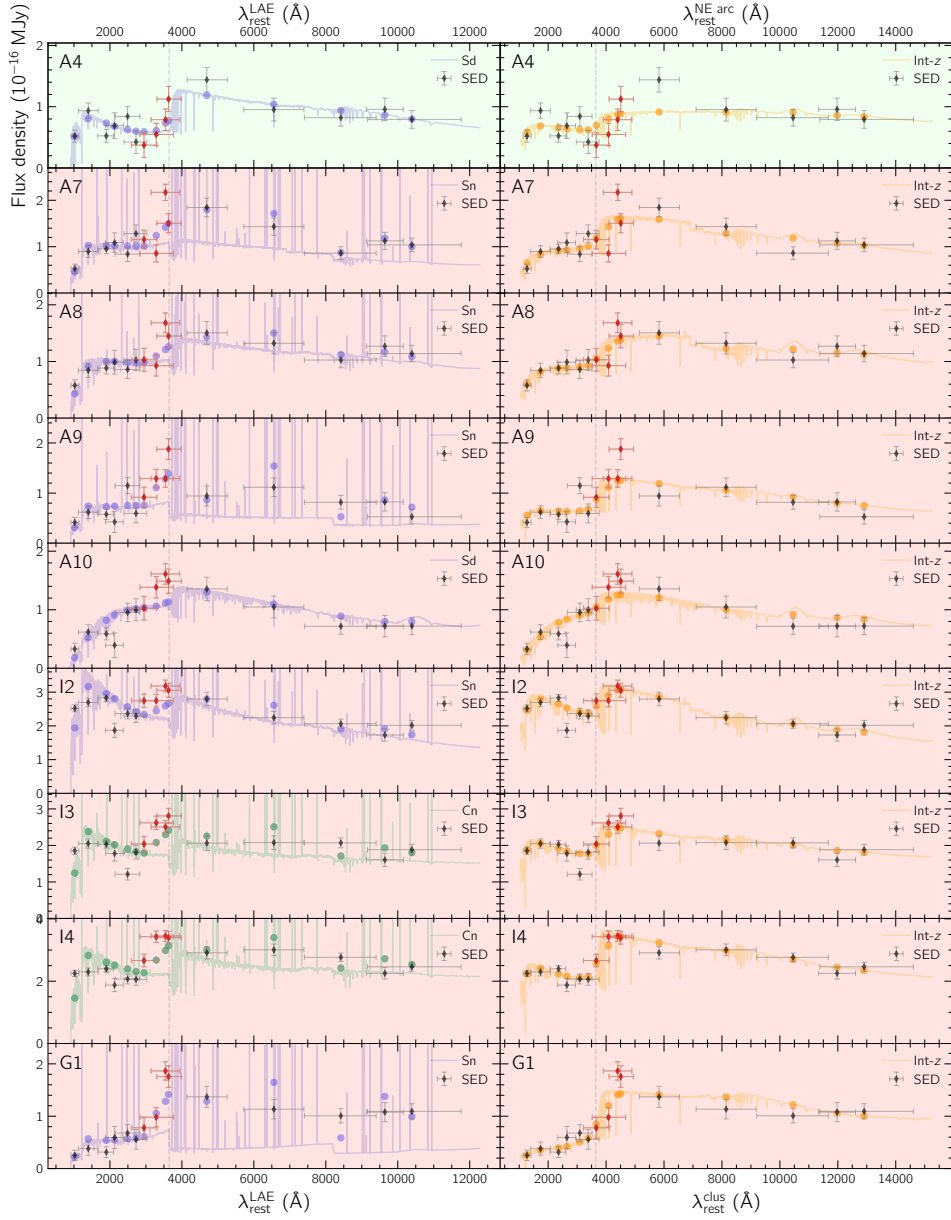


**Figure 4.12:** Comparison of the best-fitting intermediate- $z$  models (right column) with the best fitting high- $z$  models (left column). Rows shaded red indicate SEDs where the intermediate- $z$  solution is either preferred to or on par with the high- $z$  model in terms of the BIC, while rows shaded green show cases where the high- $z$  solution is preferred. The points highlighted in red lie shortwards of the Balmer break in the high- $z$  solution, but longwards of it in the intermediate- $z$  solution. Filled circles show the model spectrum convolved with the filter responses (i.e. the model's predicted SED). The vertical lines in some spectra are strong emission lines which extend upward beyond the plotted range.

increasing complexity:

Sd: a single burst allowing dust but no nebular emission

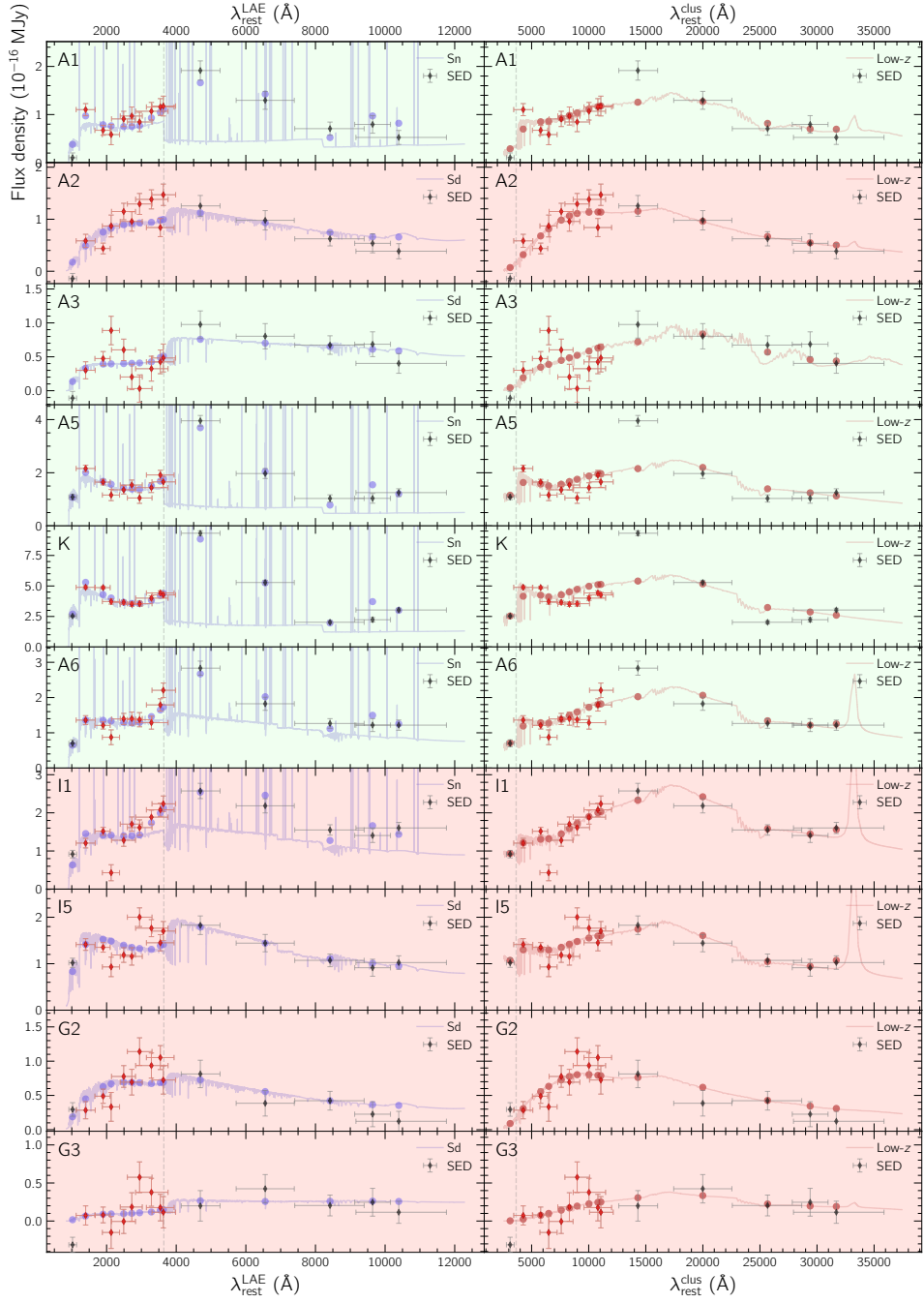


**Figure 4.13:** Comparison of the best-fitting low- $z$  models (right column) with the best fitting high- $z$  models (left column). Rows shaded red indicate SEDs where the low- $z$  solution is either preferred to or on par with the high- $z$  model in terms of the BIC, while rows shaded green show cases where the high- $z$  solution is preferred. The points highlighted in red lie shortwards of the Balmer break in the high- $z$  solution, but longwards of it in the low- $z$  solution. Filled circles show the model spectrum convolved with the filter responses (i.e. the model's predicted SED).

Sn: a single burst allowing both dust and nebular emission

Cd: a constant SFH allowing dust but no nebular emission

Cn: a constant SFH allowing both dust and nebular emission

In all these models, we fixed the redshift to 3.236, the systemic redshift of LAE3.24 found from optically-thin nebular emission lines. For models Sd and Sn, we set uniform priors on the age of the bursts between 0 and the age of the universe at  $z = 3.236$ , 2 Gyr. In all models, we use the dust attenuation law of [Calzetti et al. \(2000\)](#) assuming a single-component dust model, and set a uniform prior on dust extinction in V band,  $A_V$ , between 0 and 3.0 magnitudes. Where nebular emission is included, we set a uniform prior on the logarithm of the ionization parameter,  $\log U$ , between  $-5.0$  and  $-2.0$  (the maximum allowed value with Bagpipes' default photoionization models). In models Cd and Cn we set a uniform prior on the onset of star formation,  $\text{Age}_{\text{max}}$ , as well as the age at which star formation ceases,  $\text{Age}_{\text{min}}$ , between 0 and 2 Gyr. In all cases, we set uniform priors on the metallicity between  $0 Z_\odot$  and  $2.5 Z_\odot$ , and on the stellar mass between 0 and  $10^{13} M_\odot$ . We also adopt the default stellar initial mass function (IMF) for Bagpipes, a Kroupa IMF ([Kroupa, 2001](#)), and the standard model stellar spectra of [Bruzual and Charlot \(2003\)](#).

### Identifying low- $z$ interlopers

We also used Bagpipes to check which of the features from which we extract SEDs could be associated with (i) the intermediate-redshift NE arc or (ii) low-redshift interlopers from MACS0416 itself. Checking for low-redshift interlopers is a vital step generally when performing SED fitting of objects in cluster fields, as objects such as intracluster globular clusters (ICGCs) or stellar streams may masquerade as knots or arcs associated with the target. To explore these possibilities, we fitted two additional single-burst models, with redshifts fixed to that of the NE arc ( $z = 2.41$ ) and that of MACS0416 ( $z = 0.398$ ) respectively. We set uniform priors on age between 0 and the age of the universe at the respective redshifts, and metallicity between  $0 Z_\odot$  and  $2.5 Z_\odot$ . The prior on mass was the same as the high- $z$  single-burst models. We evaluated the goodness of fit of the low- $z$  model relative to the high- $z$  models for each SED via the Bayesian Information Criterion (BIC; [Schwarz 1978](#)). The BIC is defined as  $\text{BIC} = k \ln(n) - 2 \ln(\hat{L})$ , where  $k$  is the number of free parameters in the model,  $n$  is the number of observed data points, and  $\hat{L}$  is the maximum likelihood of the model. Similarly to other measures of goodness of fit such as reduced- $\chi^2$ , the BIC obtains a lower value for models that fit the observed data more closely, yet also incurs a penalty for models that use more free parameters. We consider differences  $\Delta \text{BIC} > 2$  to indicate a preference of the model with the lower BIC over that with the higher BIC, and differences  $\Delta \text{BIC} > 10$  to constitute strong evidence in favor of the model with the lower BIC (following [Kass and Raftery 1995](#)). Figure 4.14 shows the BIC of all the models relative to the minimum BIC for each SED, with the intermediate- $z$  solution (set to  $z = 2.41$ , the redshift of the NE arc) shown with orange inverted triangles, and the low- $z$  solution (set to  $z = 0.389$ , the redshift

of MACS0416) shown with red inverted triangles. We found that high- $z$  models are clearly preferred for SEDs A5 – A6 and K, and more weakly preferred for A1, A3, and A4 (which is unsurprising given their lower signal-to-noise ratios). On the other hand, A7 is ambiguous, with both high- and low- $z$  solutions being equally plausible, possibly indicating an overlap between LAE3.24 and the NE arc. The remaining SEDs show a preference for either the intermediate- $z$  solution or the low- $z$  solutions. As expected, most of the SEDs extracted from the NE arc (I2 – I4) show an extremely strong preference for the intermediate- $z$  solution, except for I1, where the low- $z$  solution is preferred (albeit not extremely strongly), and I5, where the low- and intermediate- $z$  solutions are on equal footing.

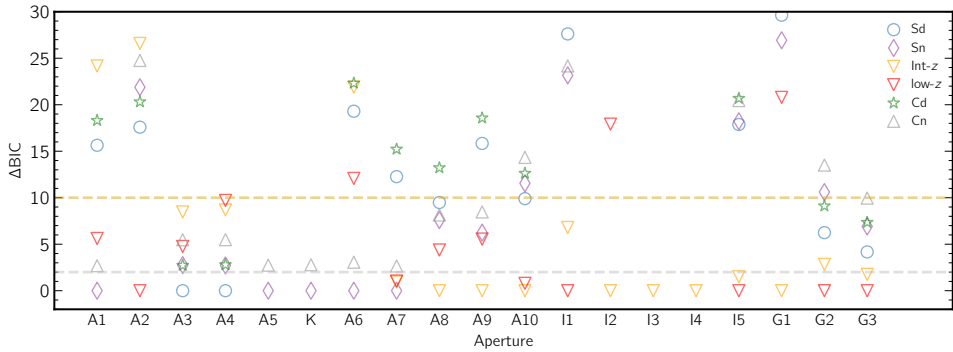


**Figure 4.14:** BIC values for each model type and each SED. Lower values indicate a better goodness of fit. Symbols that are not shown are off the scale of this figure, e.g. the low- $z$  models for SEDs A5 and K, and the high- $z$  models for SEDs A12 – A14.

To better understand what features in the SEDs determine whether the low-/intermediate-, or high- $z$  models are more successful, we compared the respective maximum-likelihood models produced by Bagpipes. We show these comparisons in Figures 4.12 and 4.13. Here, the left columns show the most successful high- $z$  model for each SED, while the right columns show the most successful (in terms of BIC) alternative redshift solutions: intermediate- $z$  in Figure 4.12 and low- $z$  in Figure 4.13. Figure 4.12 reveals a key feature that determines whether the intermediate- $z$  model is preferred over the high- $z$  model. In SEDs I2 – I4, which come from a bright part of the NE arc, the red points are elevated relative to those at shorter wavelengths, suggesting they lie longwards of the Balmer break. On the other hand, in SED A4, where the high- $z$  solution is preferred, the same points have comparable flux density to those at shorter wavelengths, suggesting they lie shortwards of the Balmer break. Where the intermediate- $z$  models are preferred, they are consistent with young stellar populations of age  $\lesssim 10$  Myr, low metallicity  $Z \lesssim 0.1 Z_{\odot}$ , and moderate dust attenuation ( $A_V \sim 0.5$ ). Similarly, Figure 4.13 shows how the Balmer break can also be used to favor the high- $z$  over the low- $z$  model. In cases where the high- $z$  model is preferred, there is a clear sharp decrement which is identified with the Balmer limit, while in cases where the low- $z$  model is preferred, there is a smooth decline towards shorter wavelengths. This shape can be explained by evolved stellar populations of age several Gyr with low dust

attenuation ( $A_V < 0.5$ ) and low metallicity ( $Z < 0.5 Z_\odot$ ).

On the basis of these results, we ascribe the features covered by apertures A7 – A10, I2 – I4, and G1 to be at least contaminated by, if not solely due to, the NE arc at  $z = 2.41$ . On the other hand, apertures A2, I1, I5, G2, and G3 are better characterised by models set to the redshift of MACS0416, and which feature older stellar populations up to several Gyr old. Most of these apertures cover point-like features (note that although SED A2 is extracted from the arc, it also covers such a knot indicated in Figure 4.2), suggesting that these may be ICGCs.

Satisfied that the low- and intermediate- $z$  solutions are reasonable, we flag SEDs A2, A7 – A10, I1 – I5, and G1 – G3 as likely interlopers and exclude them from further analysis. Furthermore, aperture A1 simply covers the same part of the source as apertures A3 – A5, but with lower magnification and hence lower spatial resolution and signal-to-noise ratio. Therefore, we do not include it in our analysis of the arc, though we check that the results are consistent with those of the other apertures.

### Comparing SEDs along the arc

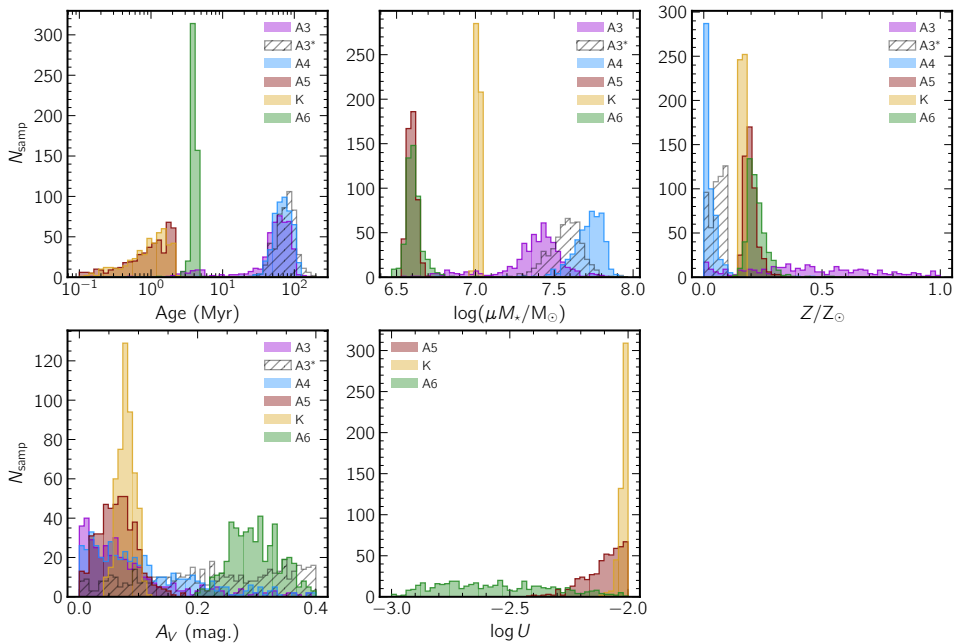


**Figure 4.15:** Comparison of posteriors obtained for single-burst models fitted to SEDs A3 – A6 and K. Note that mass is given in units of  $M_\odot \mu^{-1}$ , where  $\mu$  is the lensing magnification, which varies across the arc.

We show a comparison of the posteriors produced by Bagpipes for SEDs A3 – A6 and K with single-burst star formation histories in Figure 4.15. For the sake of clarity, we exclude the results from SED A1, which covers approximately the same region of the source as apertures A3 – A5 but in counterimage **b**, which has lower magnification and therefore spatial resolution than the other SEDs (we find the fitting

results to be consistent with those found for the highly-magnified counterpart **a**). SEDs K and A5 – extracted from the knot and adjacent south-western arc – are characterised by very young stellar populations (age  $\lesssim 2$  Myr), sub-solar metallicity ( $Z/Z_{\odot} \sim 0.2$ ), and low dust extinction ( $A_V \lesssim 0.1$ ), and strong nebular emission ( $\log U$  approaching the maximum value of  $-2.0$ ). SED A6 – extracted from the north-eastern arc adjacent to the knot – is characterised by a slightly older stellar population (age  $\sim 4$  Myr) but consistent metallicity with A5 and K. Though the difference in age is only a few Myr, the age posterior of A6 has almost no overlap with those of A5 and K. SED A6 is also characterised by a dustier solution than A5 and K ( $A_V \sim 0.3$ ), and possibly with weaker nebular emission ( $\log U$  as low as  $\sim -3.0$ ), though the overlap in the  $\log U$  posterior with those of A5 and K is non-negligible. On the other hand, SEDs A3 and A4 – extracted from the south-western end of the arc – present a very different picture, with a significantly older stellar population of age 10 Myr–100 Myr, with low dust extinction ( $A_V \lesssim 0.3$ ) and no significant nebular emission (since the BIC of the models with no line emission is significantly better than those with line emission for these SEDs, and nebular emission is very weak in the models where it is allowed). The metallicity attributed to A4 is extremely low ( $Z/Z_{\odot} \lesssim 0.1$ ), likely driven by the steep UV slope of A4 – the data points short of the Balmer break show increasing trend towards shorter wavelengths in the second row of Figure 4.16. Though such a trend cannot be seen in A3, this may be attributed to a worse signal-to-noise ratio, as is reflected in the poorly constrained metallicity shown in Figure 4.15.

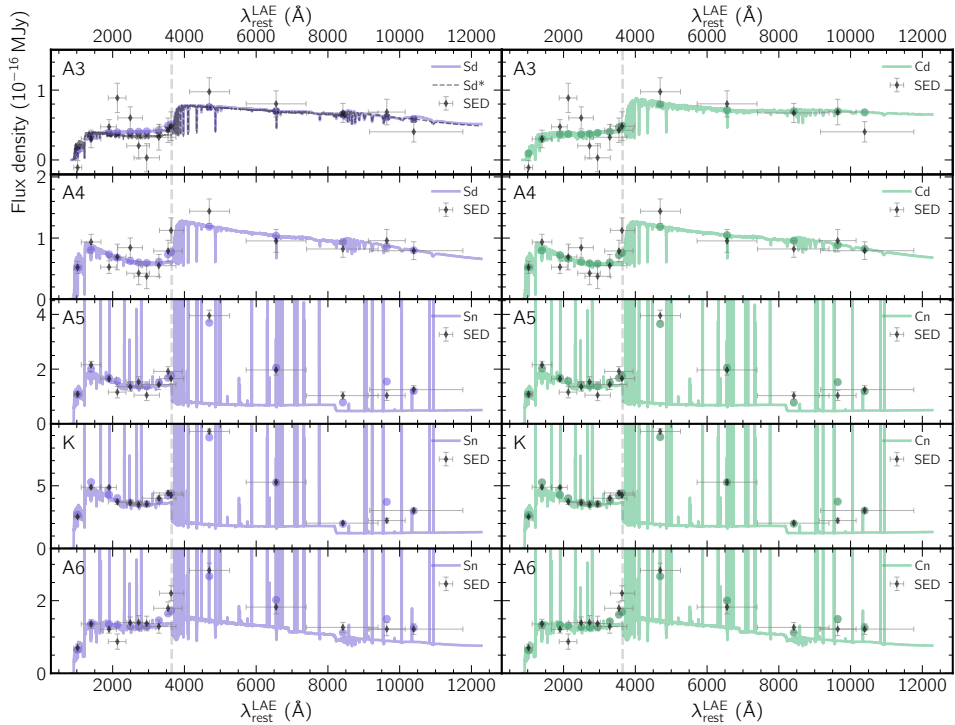


**Figure 4.16:** Comparison of the maximum-likelihood model spectra fitted to SEDs A3, A4, K, and A6 using single-burst (left) and constant (right) star formation histories.

Figure 4.16 shows the maximum-likelihood single-burst models fitted to the SEDs (left column). The plotted models illuminate some of the key differences in the SEDs that give rise to the different posteriors. Firstly, SEDs A3 and A4 are much flatter than the others, particularly longwards of the Balmer break, where the effects of nebular emission lines are strongest. This suggests weaker nebular ionization consistent with a somewhat older stellar population. A6 is also slightly flatter than A5 and K beyond the Balmer break, as well as having a flatter UV slope, suggesting greater dust attenuation.

To check for consistency between A3 and A4, we fitted a burst model to SED A3 this time setting a uniform prior on the metallicity from 0 to  $0.1 Z_{\odot}$  and on the dust extinction from 0 to 0.2 magnitudes (i.e. forcing these parameters to the approximate ranges encompassed by the posteriors of A4). The resulting fit only slightly worse than the original in terms of the BIC ( $\Delta\text{BIC} = +4$ ), but the age posterior is consistent with that of A4 as shown in Figure 4.15 (hatched black histograms). We show the maximum-likelihood model resulting from this round of fitting in Figure 4.16.

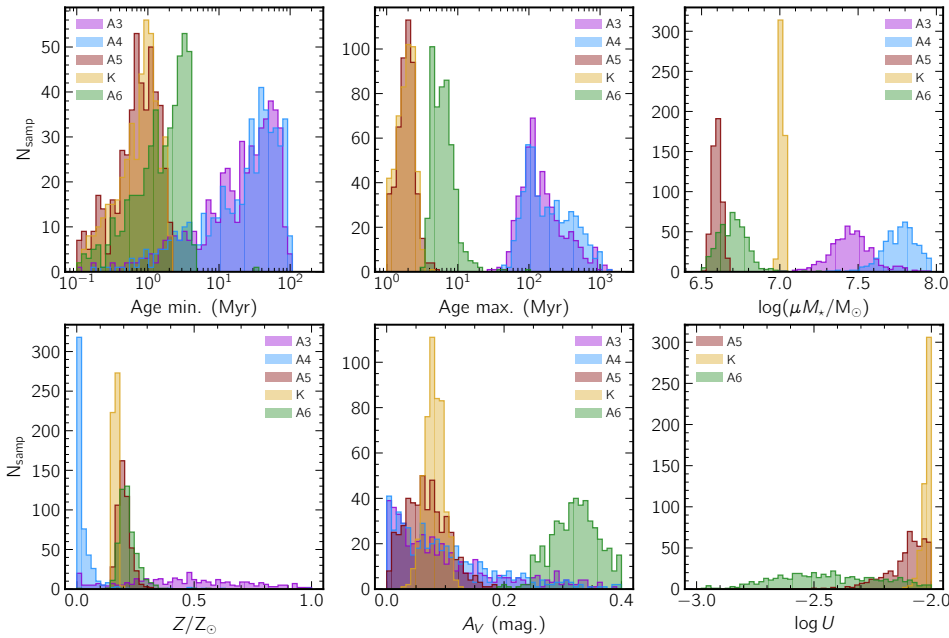


**Figure 4.17:** Comparison of posteriors obtained for constant SFH models fitted to SEDs A3 – A6 and K. For SED A3 we show the maximum-likelihood model with the same priors as the other SEDs as well as the maximum-likelihood model with low metallicity and dust extinction that we use to check for consistency with A4 (black dashed trace).

In Figure 4.16 (right column), we show the maximum-likelihood constant SFH models, which show the same trends as those of the single-burst models. In terms of BIC, the single burst models are very weakly preferred to the constant SFH models, with  $\Delta\text{BIC}$  between 2 and 3 for all SEDs, as shown in Figure 4.14. Figure 4.17 shows the posteriors for constant SFHs. Similarly to the burst models, the age posteriors suggest a very young stellar population for SEDs A5 and K, an intermediate-aged population for SED A6, and a significantly older stellar population for SEDs A3 and A4. The posteriors

in maximum (the onset of star formation) show the greatest difference between SEDs A3 and A4 and the rest, suggesting a minimum age of 30 Myr in these apertures versus a maximum age of 10 Myr for A6 and 3 Myr for A5 and K. The posteriors in the remaining parameters are consistent with the burst models.

## 4.4 Discussion

### 4.4.1 LAE3.24 as a rejuvenated LAE

Our SED fitting suggests that, rather than being homogeneously comprised of a single young stellar population, LAE3.24 may host multiple generations of stars. Apertures K and A5 are dominated by the most recent burst of star formation, which has an age of just  $\sim 1$  Myr. Moving away from the central knot along the arc to the North-East, aperture A6 covers a region with a slightly older stellar population, no more than  $\sim 10$  Myr old. In the far South-West of the arc, in apertures A3 and A4 the age increases dramatically to at least 10 Myr, possibly as old as 1 Gyr. As well as being characterised by an older stellar population, SED A4 is also characterised by a significantly lower metallicity than A5, A6, and K (due to poor signal-to-noise ratio, the metallicity of A3 is poorly constrained, though consistent with that of A4 as discussed in Section 4.3.3). A very low metallicity of less than  $0.1 Z_{\odot}$  is obtained for A4 for both single-burst and constant SFH models as shown in Figures 4.15 and 4.17 respectively in contrast to A5, A6, and K which all are characterised by metallicities between  $0.15 Z_{\odot}$  and  $0.3 Z_{\odot}$ . This comparatively high metallicity is difficult to explain if LAE3.24 is experiencing its first burst of star formation, but is naturally explained by the presence of an older stellar population which could chemically enrich the ISM/CGM.

Feedback from star formation is thought to be more effective at removing gas from low-mass galaxies via outflows (Mitchell et al., 2020), inhibiting further star formation as well as removing metal-enriched gas (which is invoked to explain the galaxy mass-metallicity relation; see Hopkins et al. 2014; Curti et al. 2020). The presence of multiple generations of stars in LAE3.24, with the earlier generation possibly chemically enriching the later one, suggests that feedback from the first generation of stars does not entirely preclude future star formation. This raises the question of how LAE3.24 may have become rejuvenated. A morphology consisting of multiple clumps might suggest a merger, but as we discuss below, there is no sign of such substructure in LAE3.24. Another possibility is cold accretion from the CGM, which simulations of a  $10^9 M_{\odot}$  LAE by Blaizot et al. (2023) suggest may be possible. These simulations show that an isolated LAE can go through a sequence of inflows and outflows, with the inflow-dominated phases being halted by bursts of star formation, which then trigger outflow-dominated phases, with a period of order  $\sim 100$  Myr. This scenario naturally explains the apparent metal enrichment of the young generation of stars, if they form from previously expelled metal-enriched gas from the CGM, as well as the age difference between the

generations of  $\sim 100$  Myr. It remains to be seen whether significant cold accretion of this kind is possible in a lower-mass object such as LAE3.24 ( $M_\star \sim 10^6 M_\odot$ ).

#### 4.4.2 Source plane morphology

The lensed images of LAE3.24 in Figure 4.2 show no sign of substructure (i.e. clumps). This stands in contrast to studies of similar objects, such as Meštrić et al. (2022), which find them typically to comprise multiple distinct star-forming clumps. Vanzella et al. (2017) estimate the total magnification of LAE3.24 to be between 37 and 110<sup>2</sup>. When decomposed into tangential (i.e. approximately parallel to the arc) and radial (i.e. perpendicular to the arc) components, Vanzella et al. (2017) estimate the tangential magnification to be between  $\sim 20$  and  $\sim 30$ . At this magnification, it should be possible to resolve structures as small as  $\sim 17$  pc to  $\sim 25$  pc along the arc in the JWST F090W, F115W, and F150W filters (which all have PSF FWHM of  $\sim 0.06''$ ). Thus, the lack of observed substructure in LAE3.24 is unlikely to be explained by low lensing magnification, implying that the source-plane morphology may be as simple as a single spheroid (or possibly an ellipsoid). This makes LAE3.24 unusual compared to similar low-mass LAEs from the same sample, which almost always show a morphology consisting of multiple clumps when magnified this strongly (Meštrić et al., 2022).

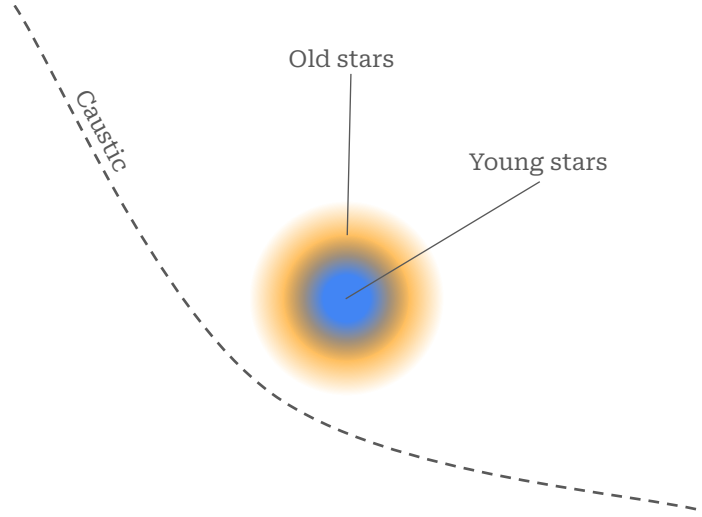


**Figure 4.18:** Cartoon illustrating the kind of source-plane geometry that could give rise to the lensed morphology of LAE3.24, where we find an older stellar population in the part of the lensed arc closest to the CC (closest to the caustic in the source plane as illustrated here).

As can be seen in Figure 4.2, the part of the lensed arc in which we detect an older stellar population is closer to the lensing CC (and hence the lensing caustic in the source plane) than the young star-forming region covered by apertures A5 and

<sup>2</sup>Vanzella et al. (2017) arrive at this range by taking the flux ratio between counterimages a and c to find the relative magnification, and multiplying this by the magnification predicted for counterimage c. Since this counterimage is further from the critical curve, its magnification is less sensitive to changes in the lensing potential and hence has lower systematic uncertainty.

K. Consequently, the magnification – which increases closer to the CC – is greater in apertures A3 and A4. A simple hypothetical source plane geometry that could give rise to the observed change in age along the arc, is that of a diffuse older stellar component extending to a larger radius in the source plane than the young star-forming region. Figure 4.18 shows a cartoon illustration of what this configuration may look like. Here, the higher magnification in the side of the source closest to the caustic allows us to spatially resolve the regions dominated by old and young stars, explaining why the older stellar population can be detected in apertures A3 and A4. On the opposite side of the source to the caustic (aperture A6), the magnification is too low to resolve the parts dominated by young and old stars, so the young stellar population outshines the old. Meanwhile, at the center of the source where the young population is brightest (apertures A5 and K), it entirely outshines the older population.

If the above picture is correct, then in the inner region the young stellar population overlaps with the old, raising the question of whether the two stellar populations can be detected simultaneously in the SEDs extracted from apertures A5, K, and A6. To see if this is the case, we fitted double-burst stellar population models to these SEDs. We set uniform priors on the age of the younger burst between 0 and 10 Myr, and on the older burst between 10 Myr and the age of the universe at  $z = 3.236$ . All other priors we set to be the same as in the single-burst model (Sn), except for the metallicity of the older stellar population, which we constrained to be sub-solar. Figure 4.19 shows the resulting posteriors for the older stellar populations – those of the young stellar populations are essentially identical to those from the single-burst models shown in Figure 4.15. Though these results show no evidence for an older underlying stellar population in SEDs A5, K, and A6, nor do they place strict upper limits on the mass of old stars. For SEDs A5 and A6, the upper limit is  $\sim 10^8 M_\odot/\mu$ , which is consistent with the mass in old stars found in aperture A4 (see posteriors in  $\mu M_\star$  in 4.15). For SED K the upper bound is stricter, at just  $\sim 10^7 M_\odot/\mu$ , compared with a mass of  $\gtrsim 10^{7.5} M_\odot/\mu$  in A4; however, the magnification in aperture K is likely lower than in A4, mitigating the tension in this result. That no clear sign of the old stellar population is found in SEDs A5, K, and A6 is not surprising given the well-documented phenomenon of outshining, wherein the bright continuum from young stellar populations overwhelms the much fainter old stars (see Narayanan et al. 2024 for a recent discussion of this effect). Given these considerations, we consider the basic picture shown in Figure 4.18 to be plausible, though detailed lens modelling will help to shed light on the actual magnifications as well as intrinsic source morphology (size, brightness profile, and ellipticity; see Chapter 5).

## 4.5 Summary and Conclusion

We performed spatially-resolved stellar population modelling of an isolated, compact, star-forming clump in the early universe, LAE3.24. Based on SED modelling, we presented evidence of a hitherto undetected older underlying stellar population in this

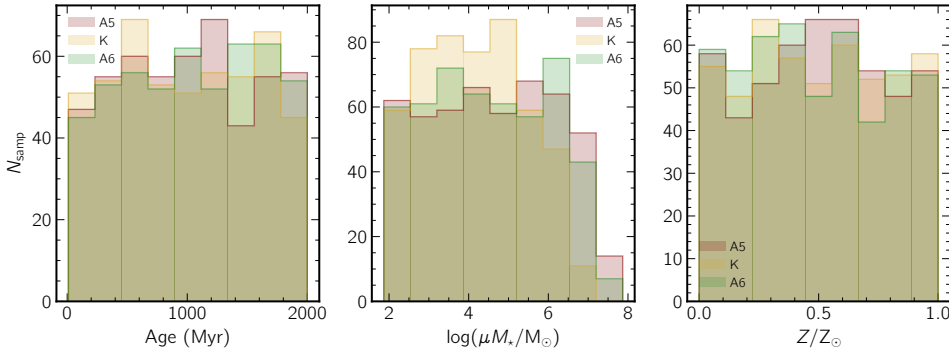


**Figure 4.19:** Posterior distributions of parameters obtained for old stellar populations in double-burst models fitted to SEDs A5, K, and A6. Note that mass is given in units of  $M_{\odot}\mu^{-1}$ , where  $\mu$  is the lensing magnification, which varies across the arc. The posteriors show no preference in terms of age and metallicity, and show only upper bounds in mass of old stars.

object (besides the already-known young stellar population). To our knowledge, this is the first time that evidence for an underlying old stellar population in a star-forming object of this size and mass in the early universe has been found. The old stellar population is detected only in the outskirts of the object, suggesting that it is outshone elsewhere, highlighting the difficulty of detecting older stars in spatially-unresolved studies. We suggest that the rejuvenation of this object is consistent with accretion of metal-enriched cool gas from the CGM previously expelled in an outflow. We find the observed morphology to be consistent with simple spheroidal or ellipsoidal profile which the old stars extend to a larger radius than the young, but are outshone by them so as to be undetected in SEDs extracted from the inner region. We intend to perform detailed lens modelling to better constrain the actual source plane morphology.

## 4.6 Acknowledgments

J.L. and J.N. acknowledge support from the Research Grants Council of Hong Kong for conducting this work under the General Research Fund 17312122. We also thank Rogier Windhorst and the rest of the PEARLS collaboration for providing us with early access to the JWST images of MACS0416. This research made use of `photutils`, an Astropy package for detection and photometry of astronomical sources (Bradley et al., 2022).

## Chapter 5

# Conclusions and Future Work

## 5.1 Conclusions

In this thesis, I studied outflows of molecular and ionized/atomic outflows in the early universe and their host systems. Together, the results presented herein paint a picture of abundant outflows from star-forming objects in the early universe in ionized, atomic, and molecular gas. These objects include star-forming disc galaxies that are the progenitors of massive spiral galaxies seen in the present-day universe, as well as compact, low-mass objects that are the building blocks from which more massive galaxies form. The multiphase nature of the outflows demonstrate the ability of outflows to regulate star formation by entraining cooler gas, including the molecular phase that comprises the direct fuel for star formation.

In my study of molecular outflow signatures from dusty star forming galaxies in the early universe, presented in Chapter 2, I searched for signatures of molecular outflows in gravitationally-lensed DSFGs. I compared OH absorption due to molecular gas with [C II] emission from atomic gas in the ISM both in spatially-integrated spectra and spatially-resolved channel maps. I found that

- 1.1 Outflow signatures found by Spilker et al. (2018) and Spilker et al. (2020b) comparing spatially-integrated OH absorption with [C II] emission spectra are not statistically significant in four of five cases studied. Furthermore, spatially-integrated spectra alone may be unreliable indicators of outflows.
- 1.2 DSFGs in the early universe ubiquitously show distinct spatio-kinematic patterns in OH absorption compared with [C II] emission, where the latter traces gas in the rotating discs. These patterns are consistent with what may be expected from outflows, which should be kinematically de-coupled from the disc of the host galaxy.

I then presented two studies of low-mass Ly $\alpha$ -emitting galaxies in the early universe. The study of these objects is facilitated by lensing by foreground galaxy clusters, which provides a boost in signal-to-noise as well as sometimes greatly enhanced spatial resolution. In the first of these studies, I presented a spectral analysis of outflow signatures seen in the Ly $\alpha$  line profiles. I found that

- 2.1 When systemic redshifts can be measured with metal emission lines, Ly $\alpha$  emitters in the early universe ( $2.9 \lesssim z \lesssim 6.7$ ) ubiquitously show consistency between their Ly $\alpha$  emission profiles and expanding shell RT models, suggesting outflows. Furthermore, in cases where interstellar absorption lines are also detected, they are blueshifted relative to the systemic, providing firmer evidence of outflows.
- 2.2 The shape of the emergent Ly $\alpha$  line depends at least in part on the intensity of the ionization field in the source, with double-peaked Ly $\alpha$  profiles being associated with stronger nebular emission lines relative to the continuum.
- 2.3 Single-peaked Ly $\alpha$  profiles are preferentially associated with spectra in which high- and low-ionization absorption lines can be seen, suggesting more gas-rich

environments, and may be associated with more strongly blueshifted absorption lines, suggesting faster outflows. This is consistent with expectations from expanding shell RT models, in which faster expansion and/or higher neutral column density results in single-peaked Ly $\alpha$ .

- 2.4 Where absorption line doublet ratios can be measured, they suggest that the absorption arises in optically thick clumps both in tracers of high- and low-ionization gas.
- 2.5 Attempts to determine outflow parameters using grids of expanding shell RT models may be of limited use: while they agree qualitatively with our results in terms of shell expansion velocity and neutral column density, they appear to over-emphasize the importance of the intrinsic Ly $\alpha$  line profile prior to RT effects. This may be due to these models not taking clumpiness into account.

In the second study focusing on Ly $\alpha$ -emitting galaxies, I presented evidence for rejuvenation of a highly magnified, compact source at  $z = 3.24$  (LAE3.24) via spatially-resolved stellar population modelling. This object has an effective radius  $< 100$  pc and a stellar mass of just  $\sim 10^6 M_\odot$ , yet is resolved thanks to extreme magnification by gravitational lensing ( $\mu \sim 70$ ). I found that

- 3.1 LAE3.24 hosts an older underlying stellar population in addition to the newly-formed stars powering the Ly $\alpha$  emission. The metallicity of this older population may be much lower than that of the young stellar population, suggesting that the former may have chemically enriched the latter. This is consistent with a simple picture in which the metal-enriched gas ejected into the CGM by the first generation of stars cools and is accreted back to fuel the present starburst.
- 3.2 LAE3.24 appears to be an isolated object, in stark contrast to other high- $z$  star forming galaxies which are found to be composed of multiple clumps when magnified this strongly.
- 3.3 The older stars in LAE3.24 may be outshone by the young stars in the parts of the source where the two populations overlap, highlighting the difficulty of determining the true ages (i.e. the ages of the oldest stars) of this source and others like it.

## 5.2 Ongoing/future work

### 5.2.1 SED modelling of Ly $\alpha$ emitters

Building upon the work in Chapters 3 and 4, I have begun a photometric study of star formation histories and stellar properties of the lensed Ly $\alpha$  sources from the R21 catalogues using JWST and HST. Much of the data reduction for this project has already been completed: I have extracted SEDs from all the Lyman- $\alpha$  sources from MACS0416 and A2744 (the only clusters that have JWST data as of the writing of this thesis).

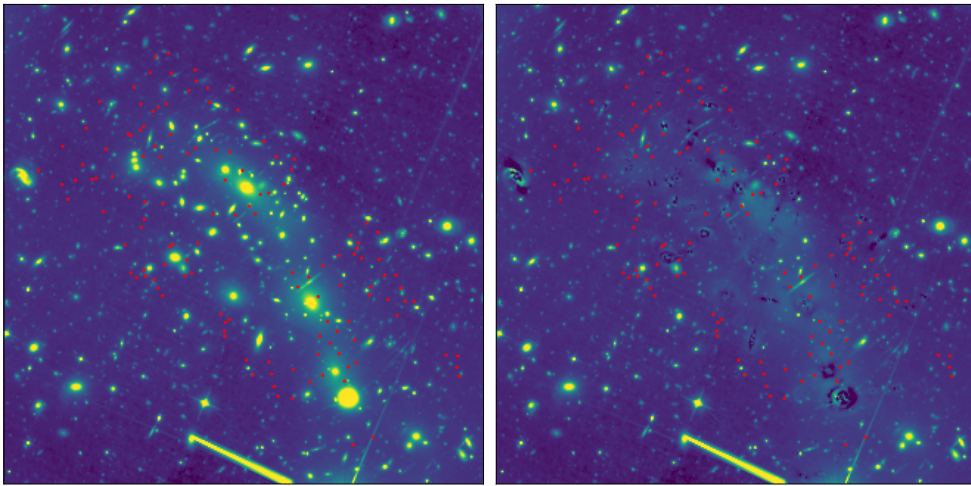


**Figure 5.1:** HST F814W image of MACS0416 before (left) and after (right) modelling and subtraction of cluster member light profiles. The red points indicate the locations of LAEs from the R21 catalogues.

This is a challenging process due to the faintness of the target sources relative to the bright foreground galaxies. For this reason, an approach often taken in the literature is to fit light profiles to the cluster members and subtract them before extracting the SEDs from the faint background sources. Indeed, this is the approach taken by the *Ultradeep NIRSpec and NIRCam Observations before the Epoch of Reionization* (UNCOVER) collaboration, who provide a catalogue of high- $z$  lensed galaxies behind A2744. I use the images provided in the UNCOVER data release<sup>1</sup> from which the cluster members have been subtracted to generate the SEDs. For MACS0416, I perform the cluster member subtraction myself, fitting analytic profiles to the brightest 100 cluster members and then subtracting them. Figure 5.1 shows an example image (F814W HST filter) of MACS0416 before and after cluster member subtraction. I then perform aperture photometry on the subtracted and PSF-matched images of A2744 and MACS0416. I generate errors via a Monte-Carlo procedure, randomly placing apertures in areas free from sources close to each target (similarly to how I generated errors for the SEDs in Chapter 4). I generate SEDs from 177 lensed images in this way. Figure 5.2 shows example SEDs from A2744 and MACS0416.

I have performed preliminary fitting of the SEDs using `Bagpipes`, but a number of outstanding issues still remain before the analysis is complete. These include:

- (i) Accounting for complex source morphology: the lensed images of the sources often exhibit clumpy morphology, as in the sources shown in Figure 5.2 and those studied by Meštrić et al. (2022). This calls for careful placement of multiple apertures on each feature, and masking to ensure that the background annulus of each knot is not contaminated by any others.

<sup>1</sup><https://jwst-uncover.github.io/DR4.html>

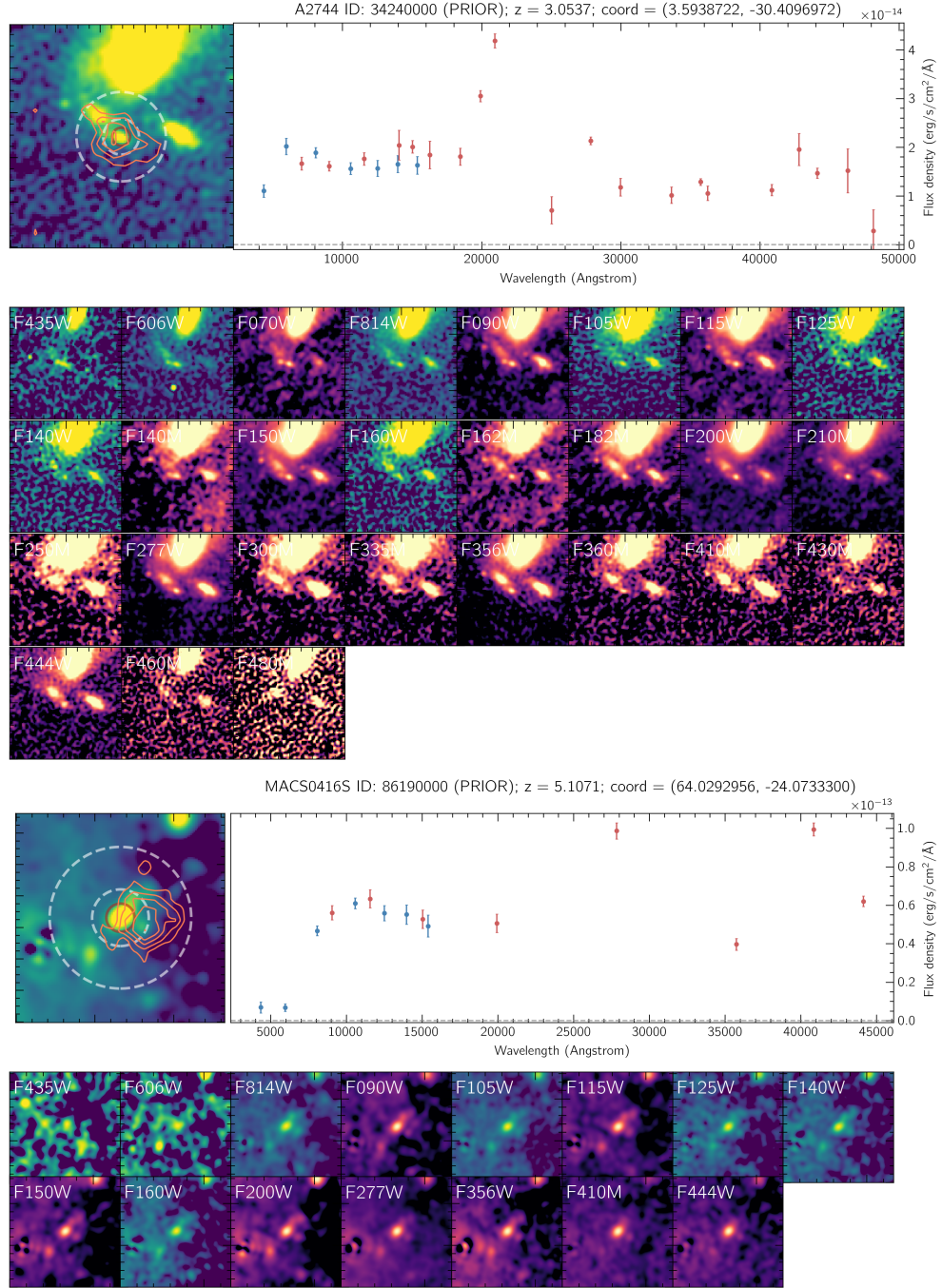


**Figure 5.2:** Example SEDs along with stacked postage stamp images. Stacked postage stamps are shown to the left of the SED, while the individual filters are shown below. Also shown in the stacked image are Ly $\alpha$  contours from MUSE and apertures and background annuli used for aperture photometry. Note that the object from A2744 (upper) has more filters than that from MACS0416 (lower) due to the UNCOVER program containing more filters, including several medium-band JWST filters.

- (ii) Elimination of possible low- or intermediate-redshift interlopers. For this process, I plan to use a scheme similar to that adopted in Chapter 4, using the BIC to determine whether each knot truly belongs to the target source.

As well as characterising the stellar populations in lensed LAEs, this work offers the chance to compare the stellar properties with the spectral results found in Chapter 3. This promises to shed further light on the properties of the underlying stellar populations that help shape the emergent Ly $\alpha$  line, and hence the properties of outflows.

### **5.2.2 Lensing reconstruction of LAE3.24**

In order to understand the intrinsic morphology of the source investigated in Chapter 4 (LAE3.24), an accurate lens model is required. Unfortunately, no existing lens models that we are aware of predict the relative magnifications of counterimages **a** and **b** to acceptable precision (most lens models either place the CC much closer to **b** than **a**, which would result in a higher magnification for **b**, contrary to what is seen in the images). This will require creation of a new lens model for MACS0416 specifically tuned to reproduce the observed brightnesses of the multiple images of LAE3.24. Fortunately, this is something that my collaborators have abundant experience in doing. Using such an optimised lens model, we will be able to test different intrinsic source profiles for LAE3.24 by forward-lensing them from the source plane into the image plane via the lens model, and seeing which intrinsic morphology best reproduces the observed lensed images. To further test whether there is a spatially-extended underlying stellar population, we will try using double-Sersic profiles for the source plane morphology. If the hypothesised source morphology presented in Chapter 4 is correct, the source should be well-fitted by a double-Sersic, with one shallower and more spatially extended (the older stellar population), and one steeper and more compact (the young population). Lensing reconstruction will also give us a more accurate estimate of its size and mass, which may be compared with evolutionary scenarios to ascertain whether it could evolve to become a dwarf galaxy or a globular cluster. The major potential limiting factor in lens modelling will be degeneracies in the lens model, which may make it difficult to ascertain source ellipticity reliably. While this limitation may prevent us from determining definitively whether the source has a disc or not, it will not impede our ability to check for multiple stellar populations with distinct Sersic components.

# Bibliography

- Aguirre, A., Hernquist, L., Schaye, J., Katz, N., Weinberg, D. H., and Gardner, J. Metal Enrichment of the Intergalactic Medium in Cosmological Simulations. *Astrophysical Journal*, 561(2):521–549 (2001). doi:10.1086/323370.
- Ahn, S.-H. Singly Peaked Asymmetric Ly $\alpha$  from Starburst Galaxies. *Astrophysical Journal, Letters*, 601(1):L25–L28 (2004). doi:10.1086/381750.
- Anglés-Alcázar, D., Faucher-Giguère, C.-A., Kereš, D., Hopkins, P. F., Quataert, E., and Murray, N. The cosmic baryon cycle and galaxy mass assembly in the FIRE simulations. *Monthly Notices of the RAS*, 470(4):4698–4719 (2017). doi:10.1093/mnras/stx1517.
- Aniano, G., Draine, B. T., Gordon, K. D., and Sandstrom, K. Common-Resolution Convolution Kernels for Space- and Ground-Based Telescopes. *Publications of the ASP*, 123(908):1218 (2011). doi:10.1086/662219.
- Astropy Collaboration, Price-Whelan, A. M., Lim, P. L., et al. The Astropy Project: Sustaining and Growing a Community-oriented Open-source Project and the Latest Major Release (v5.0) of the Core Package. *apj*, 935(2):167 (2022). doi:10.3847/1538-4357/ac7c74.
- Astropy Collaboration, Price-Whelan, A. M., Sipőcz, B. M., et al. The Astropy Project: Building an Open-science Project and Status of the v2.0 Core Package. *Astronomical Journal*, 156(3):123 (2018). doi:10.3847/1538-3881/aabc4f.
- Astropy Collaboration, Robitaille, T. P., Tollerud, E. J., et al. Astropy: A community python package for astronomy. *Astronomy and Astrophysics*, 558:A33 (2013). doi:10.1051/0004-6361/201322068.
- Bacon, R., Accardo, M., Adjali, L., et al. The MUSE second-generation VLT instrument. In I. S. McLean, S. K. Ramsay, and H. Takami, editors, *Ground-based and Airborne Instrumentation for Astronomy III*, volume 7735 of *Society of Photo-Optical Instrumentation Engineers (SPIE) Conference Series*, page 773508 (2010). doi:10.1117/12.856027.
- Bacon, R., Conseil, S., Mary, D., et al. The MUSE Hubble Ultra Deep Field Survey. I. Survey description, data reduction, and source detection. *Astronomy and Astrophysics*, 608:A1 (2017). doi:10.1051/0004-6361/201730833.
- Bahcall, J. N. and Salpeter, E. E. Absorption Lines in the Spectra of Distant Sources. *Astrophysical Journal*, 144:847 (1966). doi:10.1086/148675.

- Bell, E. F., McIntosh, D. H., Katz, N., and Weinberg, M. D. The Optical and Near-Infrared Properties of Galaxies. I. Luminosity and Stellar Mass Functions. *Astrophysical Journal, Supplement*, 149(2):289–312 (2003). doi:10.1086/378847.
- Berg, D. A., Chisholm, J., Erb, D. K., Skillman, E. D., Pogge, R. W., and Olivier, G. M. Characterizing Extreme Emission-line Galaxies. I. A Four-zone Ionization Model for Very High-ionization Emission. *Astrophysical Journal*, 922(2):170 (2021). doi:10.3847/1538-4357/ac141b.
- Beroiz, M., Cabral, J., and Sanchez, B. Astroalign: A python module for astronomical image registration. *Astronomy and Computing*, 32:100384 (2020). ISSN 2213-1337. doi:<https://doi.org/10.1016/j.ascom.2020.100384>.
- Berry, M., Gawiser, E., Guaita, L., et al. Stacked Rest-frame Ultraviolet Spectra of Ly $\alpha$ -emitting and Continuum-selected Galaxies at  $2 < z < 3.5$ . *Astrophysical Journal*, 749(1):4 (2012). doi:10.1088/0004-637X/749/1/4.
- Bertin, E. and Arnouts, S. SExtractor: Software for source extraction. *Astronomy and Astrophysics, Supplement*, 117:393–404 (1996). doi:10.1051/aas:1996164.
- Bizyaev, D., Chen, Y.-M., Shi, Y., Riffel, R. A., Riffel, R., Diamond-Stanic, A. M., and Roy, N. SDSS IV MaNGA: Star-formation-driven Biconical Outflows in the Local Universe. *Astrophysical Journal*, 882(2):145 (2019). doi:10.3847/1538-4357/ab3406.
- Blaizot, J., Garel, T., Verhamme, A., et al. Simulating the diversity of shapes of the Lyman- $\alpha$  line. *Monthly Notices of the RAS*, 523(3):3749–3772 (2023). doi:10.1093/mnras/stad1523.
- Bordoloi, R., Simcoe, R. A., Matthee, J., et al. EIGER IV. The Cool  $10^4$  K Circumgalactic Environment of High-redshift Galaxies Reveals Remarkably Efficient Intergalactic Medium Enrichment. *Astrophysical Journal*, 963(1):28 (2024). doi:10.3847/1538-4357/ad1b63.
- Bradley, L., Sipócz, B., Robitaille, T., et al. astropy/photutils: (2022). doi:10.5281/zenodo.6385735.
- Bregman, J. N., Schulman, E., and Tomisaka, K. High-Resolution X-Ray Imaging of the Starburst Galaxy M82. *Astrophysical Journal*, 439:155 (1995). doi:10.1086/175160.
- Bruzual, G. and Charlot, S. Stellar population synthesis at the resolution of 2003. *Monthly Notices of the RAS*, 344(4):1000–1028 (2003). doi:10.1046/j.1365-8711.2003.06897.x.
- Calzetti, D., Armus, L., Bohlin, R. C., Kinney, A. L., Koornneef, J., and Storchi-Bergmann, T. The Dust Content and Opacity of Actively Star-forming Galaxies. *Astrophysical Journal*, 533(2):682–695 (2000). doi:10.1086/308692.
- Cameron, A. J., Katz, H., Witten, C., Saxena, A., Laporte, N., and Bunker, A. J. Nebular dominated galaxies: insights into the stellar initial mass function at high redshift. *Monthly Notices of the RAS*, 534(1):523–543 (2024). doi:10.1093/mnras/stae1547.

- Carnall, A. C., McLure, R. J., Dunlop, J. S., and Davé, R. Inferring the star formation histories of massive quiescent galaxies with BAGPIPES: evidence for multiple quenching mechanisms. *Monthly Notices of the RAS*, 480(4):4379–4401 (2018). doi:10.1093/mnras/sty2169.
- Chen, M. C., Chen, H.-W., Gronke, M., Rauch, M., and Broadhurst, T. Resolved galactic superwinds reconstructed around their host galaxies at  $z > 3$ . *Monthly Notices of the RAS*, 504(2):2629–2657 (2021). doi:10.1093/mnras/stab1041.
- Chisholm, J., Tremonti, C., and Leitherer, C. Metal-enriched galactic outflows shape the mass-metallicity relationship. *Monthly Notices of the RAS*, 481(2):1690–1706 (2018). doi:10.1093/mnras/sty2380.
- Chisholm, J., Tremonti, C. A., Leitherer, C., Chen, Y., and Wofford, A. Shining a light on galactic outflows: photoionized outflows. *Monthly Notices of the RAS*, 457(3):3133–3161 (2016). doi:10.1093/mnras/stw178.
- Claeysens, A., Richard, J., Blaizot, J., et al. Spectral variations of Lyman  $\alpha$  emission within strongly lensed sources observed with MUSE. *Monthly Notices of the RAS*, 489(4):5022–5029 (2019). doi:10.1093/mnras/stz2492.
- Claeysens, A., Richard, J., Blaizot, J., et al. The Lensed Lyman-Alpha MUSE Arcs Sample (LLAMAS). I. Characterisation of extended Lyman-alpha halos and spatial offsets. *Astronomy and Astrophysics*, 666:A78 (2022). doi:10.1051/0004-6361/202142320.
- Curti, M., Mannucci, F., Cresci, G., and Maiolino, R. The mass-metallicity and the fundamental metallicity relation revisited on a fully  $T_e$ -based abundance scale for galaxies. *Monthly Notices of the RAS*, 491(1):944–964 (2020). doi:10.1093/mnras/stz2910.
- Duval, F., Schaefer, D., Östlin, G., and Laursen, P. Lyman  $\alpha$  line and continuum radiative transfer in a clumpy interstellar medium. *Astronomy and Astrophysics*, 562:A52 (2014). doi:10.1051/0004-6361/201220455.
- Engelbracht, C. W., Kundurthy, P., Gordon, K. D., et al. Extended Mid-Infrared Aromatic Feature Emission in M82. *Astrophysical Journal, Letters*, 642(2):L127–L132 (2006). doi:10.1086/504590.
- Erb, D. K. Feedback in low-mass galaxies in the early Universe. *Nature*, 523(7559):169–176 (2015). doi:10.1038/nature14454.
- Feltre, A., Charlot, S., and Gutkin, J. Nuclear activity versus star formation: emission-line diagnostics at ultraviolet and optical wavelengths. *Monthly Notices of the RAS*, 456(3):3354–3374 (2016). doi:10.1093/mnras/stv2794.
- Feltre, A., Maseda, M. V., Bacon, R., et al. The MUSE Hubble Ultra Deep Field Survey. XV. The mean rest-UV spectra of Ly $\alpha$  emitters at  $z > 3$ . *Astronomy and Astrophysics*, 641:A118 (2020). doi:10.1051/0004-6361/202038133.

- Feruglio, C., Ferrara, A., Bischetti, M., et al. On the discovery of fast molecular gas in the UFO/BAL quasar APM 08279+5255 at  $z = 3.912$ . *Astronomy and Astrophysics*, 608:A30 (2017). doi:10.1051/0004-6361/201731387.
- Finkelstein, S. L., Rhoads, J. E., Malhotra, S., and Grogin, N. Lyman Alpha Galaxies: Primitive, Dusty, or Evolved? *Astrophysical Journal*, 691(1):465–481 (2009). doi:10.1088/0004-637X/691/1/465.
- Foley, M. M., Goodman, A., Zucker, C., et al. A 3D View of Orion. I. Barnard’s Loop. *Astrophysical Journal*, 947(2):66 (2023). doi:10.3847/1538-4357/acb5f4.
- Garnett, D. R., Dufour, R. J., Peimbert, M., et al. Si/O Abundance Ratios in Extragalactic H II Regions from Hubble Space Telescope UV Spectroscopy. *Astrophysical Journal, Letters*, 449:L77 (1995). doi:10.1086/309620.
- Goicoechea, J. R. and Cernicharo, J. Far-Infrared OH Fluorescent Emission in Sagittarius B2. *Astrophysical Journal, Letters*, 576(1):L77–L81 (2002). doi:10.1086/343062.
- González-Alfonso, E., Fischer, J., Spoon, H. W. W., et al. Molecular Outflows in Local ULIRGs: Energetics from Multitransition OH Analysis. *Astrophysical Journal*, 836(1):11 (2017). doi:10.3847/1538-4357/836/1/11.
- Goovaerts, I., Pello, R., Thai, T. T., et al. Evolution of the Lyman- $\alpha$ -emitting fraction and UV properties of lensed star-forming galaxies in the range  $2.9 < z < 6.7$ . *Astronomy and Astrophysics*, 678:A174 (2023). doi:10.1051/0004-6361/202347110.
- Greve, A. The apparent “reversed” motion of gas and stars in M 82. *Astronomy and Astrophysics*, 529:A51 (2011). doi:10.1051/0004-6361/201016069.
- Gronke, M., Bull, P., and Dijkstra, M. A Systematic Study of Lyman- $\alpha$  Transfer through Outflowing Shells: Model Parameter Estimation. *Astrophysical Journal*, 812(2):123 (2015). doi:10.1088/0004-637X/812/2/123.
- Gurung-López, S., Gronke, M., Saito, S., Bonoli, S., and Orsi, Á. A. zELDA: fitting Lyman alpha line profiles using deep learning. *Monthly Notices of the RAS*, 510(3):4525–4555 (2022). doi:10.1093/mnras/stab3554.
- Gurung-López, S., Orsi, Á. A., and Bonoli, S. FLAREON: a fast computation of Ly  $\alpha$  escape fractions and line profiles. *Monthly Notices of the RAS*, 490(1):733–740 (2019). doi:10.1093/mnras/stz2591.
- Gutkin, J., Charlot, S., and Bruzual, G. Modelling the nebular emission from primeval to present-day star-forming galaxies. *Monthly Notices of the RAS*, 462(2):1757–1774 (2016). doi:10.1093/mnras/stw1716.
- Hagen, A., Ciardullo, R., Gronwall, C., et al. Spectral Energy Distribution Fitting of HETDEX Pilot Survey Ly $\alpha$  Emitters in COSMOS and GOODS-N. *Astrophysical Journal*, 786(1):59 (2014). doi:10.1088/0004-637X/786/1/59.

- Harrison, C. M. Impact of supermassive black hole growth on star formation. *Nature Astronomy*, 1:0165 (2017). doi:10.1038/s41550-017-0165.
- Hayes, M., Östlin, G., Schaefer, D., et al. The Lyman Alpha Reference Sample: Extended Lyman Alpha Halos Produced at Low Dust Content. *Astrophysical Journal, Letters*, 765(2):L27 (2013). doi:10.1088/2041-8205/765/2/L27.
- He, H., Dent, W. R. F., and Wilson, C. Tracking ALMA System Temperature with Water Vapor Data at High Frequency. *Publications of the ASP*, 134(1042):125001 (2022). doi:10.1088/1538-3873/aca717.
- Henriques, B. M. B., White, S. D. M., Thomas, P. A., et al. Galaxy formation in the Planck cosmology - I. Matching the observed evolution of star formation rates, colours and stellar masses. *Monthly Notices of the RAS*, 451(3):2663–2680 (2015). doi:10.1093/mnras/stv705.
- Herrera-Camus, R., Tacconi, L., Genzel, R., et al. Molecular and Ionized Gas Phases of an AGN-driven Outflow in a Typical Massive Galaxy at  $z \approx 2$ . *Astrophysical Journal*, 871(1):37 (2019). doi:10.3847/1538-4357/aaf6a7.
- Hirschmann, M., De Lucia, G., and Fontanot, F. Galaxy assembly, stellar feedback and metal enrichment: the view from the GAEA model. *Monthly Notices of the RAS*, 461(2):1760–1785 (2016). doi:10.1093/mnras/stw1318.
- Hopkins, P. F., Kereš, D., Oñorbe, J., Faucher-Giguère, C.-A., Quataert, E., Murray, N., and Bullock, J. S. Galaxies on FIRE (Feedback In Realistic Environments): stellar feedback explains cosmologically inefficient star formation. *Monthly Notices of the RAS*, 445(1):581–603 (2014). doi:10.1093/mnras/stu1738.
- Hunter, J. D. Matplotlib: A 2d graphics environment. *Computing in Science & Engineering*, 9(3):90–95 (2007). doi:10.1109/MCSE.2007.55.
- Iani, E., Caputi, K. I., Rinaldi, P., et al. MIDIS: JWST NIRCam and MIRI Unveil the Stellar Population Properties of Ly $\alpha$  Emitters and Lyman-break Galaxies at  $z \simeq 3\text{--}7$ . *Astrophysical Journal*, 963(2):97 (2024). doi:10.3847/1538-4357/ad15f6.
- Jones, T., Stark, D. P., and Ellis, R. S. Keck Spectroscopy of Faint  $3 < z < 7$  Lyman Break Galaxies. III. The Mean Ultraviolet Spectrum at  $z \sim 4$ . *Astrophysical Journal*, 751(1):51 (2012). doi:10.1088/0004-637X/751/1/51.
- Jung, I., Finkelstein, S. L., Arrabal Haro, P., et al. CEERS: Diversity of Ly $\alpha$  Emitters during the Epoch of Reionization. *Astrophysical Journal*, 967(1):73 (2024). doi:10.3847/1538-4357/ad3913.
- Kass, R. E. and Raftery, A. E. Bayes factors. *Journal of the American Statistical Association*, 90(430):773–795 (1995). doi:10.1080/01621459.1995.10476572.
- Kennicutt, R. C., Jr. Star Formation in Galaxies Along the Hubble Sequence. *Annual Review of Astron and Astrophys*, 36:189–232 (1998). doi:10.1146/annurev.astro.36.1.189.

- Kereš, D., Katz, N., Davé, R., Fardal, M., and Weinberg, D. H. Galaxies in a simulated  $\Lambda$ CDM universe - II. Observable properties and constraints on feedback. *Monthly Notices of the RAS*, 396(4):2332–2344 (2009). doi:10.1111/j.1365-2966.2009.14924.x.
- Krieger, N., Bolatto, A. D., Walter, F., et al. The Molecular Outflow in NGC 253 at a Resolution of Two Parsecs. *Astrophysical Journal*, 881(1):43 (2019). doi:10.3847/1538-4357/ab2d9c.
- Krieger, N., Walter, F., Bolatto, A. D., et al. NOEMA High-fidelity Imaging of the Molecular Gas in and around M82. *Astrophysical Journal Letters*, 915(1):L3 (2021). doi:10.3847/2041-8213/ac01e9.
- Kroupa, P. On the variation of the initial mass function. *Monthly Notices of the RAS*, 322(2):231–246 (2001). doi:10.1046/j.1365-8711.2001.04022.x.
- Kulas, K. R., Shapley, A. E., Kollmeier, J. A., Zheng, Z., Steidel, C. C., and Hainline, K. N. The Kinematics of Multiple-peaked Ly $\alpha$  Emission in Star-forming Galaxies at  $z \sim 2\text{--}3$ . *Astrophysical Journal*, 745(1):33 (2012). doi:10.1088/0004-637X/745/1/33.
- Lagos, C. d. P., Tobar, R. J., Robotham, A. S. G., Obreschkow, D., Mitchell, P. D., Power, C., and Elahi, P. J. Shark: introducing an open source, free, and flexible semi-analytic model of galaxy formation. *Monthly Notices of the RAS*, 481(3):3573–3603 (2018). doi:10.1093/mnras/sty2440.
- Lequeux, J., Kunth, D., Mas-Hesse, J. M., and Sargent, W. L. W. Galactic wind and Lyman  $\alpha$  emission in the blue compact galaxy Haro 2 = MKN 33. *Astronomy and Astrophysics*, 301:18 (1995).
- Lequeux, J., Peimbert, M., Rayo, J. F., Serrano, A., and Torres-Peimbert, S. Chemical Composition and Evolution of Irregular and Blue Compact Galaxies. *Astronomy and Astrophysics*, 80:155 (1979).
- Li, J., Liu, C., Zhang, Z.-Y., Tian, H., Fu, X., Li, J., and Yan, Z.-Q. Stellar initial mass function varies with metallicity and time. *Nature*, 613(7944):460–462 (2023). doi:10.1038/s41586-022-05488-1.
- Livermore, R. C., Finkelstein, S. L., and Lotz, J. M. Directly Observing the Galaxies Likely Responsible for Reionization. *Astrophysical Journal*, 835(2):113 (2017). doi:10.3847/1538-4357/835/2/113.
- Lotz, J. M., Koekemoer, A., Coe, D., et al. The Frontier Fields: Survey Design and Initial Results. *Astrophysical Journal*, 837(1):97 (2017). doi:10.3847/1538-4357/837/1/97.
- Lundgren, B. F., Creech, S., Brammer, G., et al. The Geometry of Cold, Metal-enriched Gas around Galaxies at  $z \sim 1.2$ . *Astrophysical Journal*, 913(1):50 (2021). doi:10.3847/1538-4357/abef6a.
- Ma, X., Hopkins, P. F., Faucher-Giguère, C.-A., Zolman, N., Muratov, A. L., Kereš, D., and Quataert, E. The origin and evolution of the galaxy mass-metallicity relation. *Monthly Notices of the RAS*, 456(2):2140–2156 (2016). doi:10.1093/mnras/stv2659.

- Madau, P. and Dickinson, M. Cosmic Star-Formation History. *Annual Review of Astron and Astrophys*, 52:415–486 (2014). doi:10.1146/annurev-astro-081811-125615.
- Maeda, F., Egusa, F., Tsujita, A., et al. Detection of CO(1-0) Emission at the Tips of the Tidal Tail in the Antennae Galaxies. *Astrophysical Journal*, 962(1):4 (2024). doi:10.3847/1538-4357/ad1932.
- Maiolino, R. and Mannucci, F. De re metallica: the cosmic chemical evolution of galaxies. *Astronomy and Astrophysics Reviews*, 27(1):3 (2019). doi:10.1007/s00159-018-0112-2.
- Martini, P., Leroy, A. K., Mangum, J. G., Bolatto, A., Keating, K. M., Sandstrom, K., and Walter, F. H I Kinematics along the Minor Axis of M82. *Astrophysical Journal*, 856(1):61 (2018). doi:10.3847/1538-4357/aab08e.
- Martins, F., Schaerer, D., Marques-Chaves, R., and Upadhyaya, A. Inferring the presence of very massive stars in local star-forming regions. *Astronomy and Astrophysics*, 678:A159 (2023). doi:10.1051/0004-6361/202346732.
- Mascia, S., Pentericci, L., Calabro, A., et al. New insight on the nature of cosmic reionizers from the CEERS survey. *Astronomy and Astrophysics*, 685:A3 (2024). doi:10.1051/0004-6361/202347884.
- McMullin, J. P., Waters, B., Schiebel, D., Young, W., and Golap, K. CASA Architecture and Applications. In R. A. Shaw, F. Hill, and D. J. Bell, editors, *Astronomical Data Analysis Software and Systems XVI*, volume 376 of *Astronomical Society of the Pacific Conference Series*, page 127 (2007).
- Meixner, M., Cooray, A., Leisawitz, D. T., et al. Origins Space Telescope science drivers to design traceability. *Journal of Astronomical Telescopes, Instruments, and Systems*, 7:011012 (2021). doi:10.1117/1.JATIS.7.1.011012.
- Melinder, J., Östlin, G., Hayes, M., et al. The Ly $\alpha$  Reference Sample. XIV. Ly $\alpha$  Imaging of 45 Low-redshift Star-forming Galaxies and Inferences on Global Emission. *Astrophysical Journal, Supplement*, 266(1):15 (2023). doi:10.3847/1538-4365/acc2b8.
- Messa, M., Vanzella, E., Loiacono, F., et al. Anatomy of a z=6 Lyman- $\alpha$  emitter down to parsec scales: extreme UV slopes, metal-poor regions and possibly leaking star clusters. *arXiv e-prints*, arXiv:2407.20331 (2024). doi:10.48550/arXiv.2407.20331.
- Meštrić, U., Vanzella, E., Zanella, A., et al. Exploring the physical properties of lensed star-forming clumps at  $2 \lesssim z \lesssim 6$ . *Monthly Notices of the RAS*, 516(3):3532–3555 (2022). doi:10.1093/mnras/stac2309.
- Mingozzi, M., James, B. L., Berg, D. A., et al. CLASSY. VIII. Exploring the Source of Ionization with UV Interstellar Medium Diagnostics in Local High-z Analogs. *Astrophysical Journal*, 962(1):95 (2024). doi:10.3847/1538-4357/ad1033.
- Mitchell, P. D., Lacey, C. G., Lagos, C. D. P., et al. Comparing galaxy formation in semi-analytic models and hydrodynamical simulations. *Monthly Notices of the RAS*, 474(1):492–521 (2018a). doi:10.1093/mnras/stx2770.

- Mitchell, P. D., Schaye, J., Bower, R. G., and Crain, R. A. Galactic outflow rates in the EAGLE simulations. *Monthly Notices of the RAS*, 494(3):3971–3997 (2020). doi:10.1093/mnras/staa938.
- Mongardi, C., Viel, M., D’Odorico, V., Kim, T. S., Barai, P., Murante, G., and Monaco, P. Absorption systems at  $z \sim 2$  as a probe of the circumgalactic medium: a probabilistic approach. *Monthly Notices of the RAS*, 478(3):3266–3289 (2018). doi:10.1093/mnras/sty1283.
- Nanayakkara, T., Brinchmann, J., Boogaard, L., et al. Exploring He II  $\lambda 1640$  emission line properties at  $z \sim 2\text{--}4$ . *Astronomy and Astrophysics*, 624:A89 (2019). doi:10.1051/0004-6361/201834565.
- Narayanan, D., Lower, S., Torrey, P., et al. Outshining by Recent Star Formation Prevents the Accurate Measurement of High- $z$  Galaxy Stellar Masses. *Astrophysical Journal*, 961(1):73 (2024). doi:10.3847/1538-4357/ad0966.
- Orlitová, I., Verhamme, A., Henry, A., Scarlata, C., Jaskot, A., Oey, M. S., and Schaerer, D. Puzzling Lyman-alpha line profiles in green pea galaxies. *Astronomy and Astrophysics*, 616:A60 (2018). doi:10.1051/0004-6361/201732478.
- Orsi, A., Lacey, C. G., and Baugh, C. M. Can galactic outflows explain the properties of Ly  $\alpha$  emitters? *Monthly Notices of the RAS*, 425(1):87–115 (2012). doi:10.1111/j.1365-2966.2012.21396.x.
- Ouchi, M., Ono, Y., and Shibuya, T. Observations of the Lyman- $\alpha$  Universe. *Annual Review of Astron and Astrophys*, 58:617–659 (2020). doi:10.1146/annurev-astro-032620-021859.
- Ouchi, M., Shimasaku, K., Furusawa, H., et al. Statistics of 207 Ly $\alpha$  Emitters at a Redshift Near 7: Constraints on Reionization and Galaxy Formation Models. *Astrophysical Journal*, 723(1):869–894 (2010). doi:10.1088/0004-637X/723/1/869.
- Owen, E. R., Wu, K., Inoue, Y., Yang, H. Y. K., and Mitchell, A. M. W. Cosmic Ray Processes in Galactic Ecosystems. *Galaxies*, 11(4):86 (2023). doi:10.3390/galaxies11040086.
- Pabst, C., Higgins, R., Goicoechea, J. R., et al. Disruption of the Orion molecular core 1 by wind from the massive star  $\theta^1$  Orionis C. *Nature*, 565(7741):618–621 (2019). doi:10.1038/s41586-018-0844-1.
- Pabst, C. H. M., Goicoechea, J. R., Teyssier, D., et al. Expanding bubbles in Orion A: [C II] observations of M 42, M 43, and NGC 1977. *Astronomy and Astrophysics*, 639:A2 (2020). doi:10.1051/0004-6361/202037560.
- Pakmor, R., Springel, V., Coles, J. P., et al. The MillenniumTNG Project: the hydrodynamical full physics simulation and a first look at its galaxy clusters. *Monthly Notices of the RAS*, 524(2):2539–2555 (2023). doi:10.1093/mnras/stac3620.
- Papastergis, E., Cattaneo, A., Huang, S., Giovanelli, R., and Haynes, M. P. A Direct Measurement of the Baryonic Mass Function of Galaxies and Implications

- for the Galactic Baryon Fraction. *Astrophysical Journal*, 759(2):138 (2012). doi: 10.1088/0004-637X/759/2/138.
- Péroux, C. and Howk, J. C. The Cosmic Baryon and Metal Cycles. *Annual Review of Astron and Astrophys*, 58:363–406 (2020). doi:10.1146/annurev-astro-021820-120014.
- Piqueras, L., Conseil, S., Shepherd, M., Bacon, R., Leclercq, F., and Richard, J. MPDAF - A Python Package for the Analysis of VLT/MUSE Data. In M. Molinaro, K. Shortridge, and F. Pasian, editors, *Astronomical Data Analysis Software and Systems XXVI*, volume 521 of *Astronomical Society of the Pacific Conference Series*, page 545 (2019).
- Planck Collaboration, Ade, P. A. R., Aghanim, N., et al. Planck 2013 results. XVI. Cosmological parameters. *Astronomy and Astrophysics*, 571:A16 (2014). doi:10.1051/0004-6361/201321591.
- Richard, J., Claeysens, A., Lagattuta, D., et al. An atlas of MUSE observations towards twelve massive lensing clusters. *Astronomy and Astrophysics*, 646:A83 (2021). doi: 10.1051/0004-6361/202039462.
- Rihtaršič, G., Bradač, M., Desprez, G., et al. CANUCS: Constraining the MACS J0416.1-2403 Strong Lensing Model with JWST NIRISS, NIRSpec and NIRCam. *arXiv e-prints*, arXiv:2406.10332 (2024). doi:10.48550/arXiv.2406.10332.
- Rivera-Thorsen, T. E., Hayes, M., Östlin, G., et al. The Lyman Alpha Reference Sample. V. The Impact of Neutral ISM Kinematics and Geometry on Ly $\alpha$  Escape. *Astrophysical Journal*, 805(1):14 (2015). doi:10.1088/0004-637X/805/1/14.
- Rosani, G., Caminha, G. B., Caputi, K. I., and Deshmukh, S. Bright Lyman- $\alpha$  emitters among Spitzer SMUVS galaxies in the MUSE/COSMOS field. *Astronomy and Astrophysics*, 633:A159 (2020). doi:10.1051/0004-6361/201935782.
- Rupke, D. S., Veilleux, S., and Sanders, D. B. Outflows in Infrared-Luminous Starbursts at  $z < 0.5$ . II. Analysis and Discussion. *Astrophysical Journal, Supplement*, 160(1):115–148 (2005). doi:10.1086/432889.
- Santistevan, I. B., Wetzel, A., El-Badry, K., et al. The formation times and building blocks of Milky Way-mass galaxies in the FIRE simulations. *Monthly Notices of the RAS*, 497(1):747–764 (2020). doi:10.1093/mnras/staa1923.
- Schwarz, G. Estimating the Dimension of a Model. *Annals of Statistics*, 6(2):461–464 (1978).
- Shapley, A. E., Steidel, C. C., Pettini, M., and Adelberger, K. L. Rest-Frame Ultraviolet Spectra of  $z \sim 3$  Lyman Break Galaxies. *Astrophysical Journal*, 588(1):65–89 (2003). doi: 10.1086/373922.
- Shibuya, T., Ouchi, M., Nakajima, K., et al. What is the Physical Origin of Strong Ly $\alpha$  Emission? II. Gas Kinematics and Distribution of Ly $\alpha$  Emitters. *Astrophysical Journal*, 788(1):74 (2014). doi:10.1088/0004-637X/788/1/74.

- Shimizu, I. and Umemura, M. Two types of Lyman  $\alpha$  emitters envisaged from hierarchical galaxy formation. *Monthly Notices of the RAS*, 406(2):913–921 (2010). doi: 10.1111/j.1365-2966.2010.16758.x.
- Shopbell, P. L. and Bland-Hawthorn, J. The Asymmetric Wind in M82. *Astrophysical Journal*, 493(1):129–153 (1998). doi:10.1086/305108.
- Sick, J., Courteau, S., Cuillandre, J.-C., et al. The Stellar Mass of M31 as inferred by the Andromeda Optical & Infrared Disk Survey. In M. Cappellari and S. Courteau, editors, *Galaxy Masses as Constraints of Formation Models*, volume 311 of *IAU Symposium*, pages 82–85 (2015). doi:10.1017/S1743921315003440.
- Somerville, R. S., Popping, G., and Trager, S. C. Star formation in semi-analytic galaxy formation models with multiphase gas. *Monthly Notices of the RAS*, 453(4):4337–4367 (2015). doi:10.1093/mnras/stv1877.
- Soto, K. T., Lilly, S. J., Bacon, R., Richard, J., and Conseil, S. ZAP: Zurich Atmosphere Purge. *Astrophysics Source Code Library*, record ascl:1602.003 (2016).
- Spilker, J. S., Aravena, M., Béthermin, M., et al. Fast molecular outflow from a dusty star-forming galaxy in the early Universe. *Science*, 361(6406):1016–1019 (2018). doi: 10.1126/science.aap8900.
- Spilker, J. S., Aravena, M., Phadke, K. A., et al. Ubiquitous Molecular Outflows in  $z > 4$  Massive, Dusty Galaxies. II. Momentum-driven Winds Powered by Star Formation in the Early Universe. *Astrophysical Journal*, 905(2):86 (2020a). doi:10.3847/1538-4357/abc4e6.
- Spilker, J. S., Phadke, K. A., Aravena, M., et al. Ubiquitous Molecular Outflows in  $z > 4$  Massive, Dusty Galaxies. I. Sample Overview and Clumpy Structure in Molecular Outflows on 500 pc Scales. *Astrophysical Journal*, 905(2):85 (2020b). doi:10.3847/1538-4357/abc4f7.
- Steidel, C. C., Erb, D. K., Shapley, A. E., et al. The Structure and Kinematics of the Circumgalactic Medium from Far-ultraviolet Spectra of  $z \sim= 2\text{--}3$  Galaxies. *Astrophysical Journal*, 717(1):289–322 (2010). doi:10.1088/0004-637X/717/1/289.
- Strickland, D. K., Heckman, T. M., Colbert, E. J. M., Hoopes, C. G., and Weaver, K. A. A High Spatial Resolution X-Ray and H $\alpha$  Study of Hot Gas in the Halos of Star-forming Disk Galaxies. I. Spatial and Spectral Properties of the Diffuse X-Ray Emission. *Astrophysical Journal, Supplement*, 151(2):193–236 (2004). doi:10.1086/382214.
- Sugahara, Y., Ouchi, M., Harikane, Y., Bouché, N., Mitchell, P. D., and Blaizot, J. Fast Outflows Identified in Early Star-forming Galaxies at  $z = 5\text{--}6$ . *Astrophysical Journal*, 886(1):29 (2019). doi:10.3847/1538-4357/ab49fe.
- Thompson, T. A. and Heckman, T. M. Theory and Observation of Winds from Star-Forming Galaxies. *Annual Review of Astron and Astrophys*, 62(1):529–591 (2024). doi: 10.1146/annurev-astro-041224-011924.

- Tsukui, T., Iguchi, S., Mitsuhashi, I., and Tadaki, K. Estimating the statistical uncertainty due to spatially correlated noise in interferometric images. *Journal of Astronomical Telescopes, Instruments, and Systems*, 9:018001 (2023). doi:10.1117/1.JATIS.9.1.018001.
- Tumlinson, J., Peebles, M. S., and Werk, J. K. The circumgalactic medium. *Annual Review of Astronomy and Astrophysics*, 55(Volume 55, 2017):389–432 (2017). ISSN 1545-4282. doi:<https://doi.org/10.1146/annurev-astro-091916-055240>.
- Vanzella, E., Calura, F., Meneghetti, M., et al. Paving the way for the JWST: witnessing globular cluster formation at  $z > 3$ . *Monthly Notices of the RAS*, 467(4):4304–4321 (2017). doi:10.1093/mnras/stx351.
- Vanzella, E., Caminha, G. B., Calura, F., et al. Ionizing the intergalactic medium by star clusters: the first empirical evidence. *Monthly Notices of the RAS*, 491(1):1093–1103 (2020). doi:10.1093/mnras/stz2286.
- Vanzella, E., Loiacono, F., Bergamini, P., et al. An extremely metal-poor star complex in the reionization era: Approaching Population III stars with JWST. *Astronomy and Astrophysics*, 678:A173 (2023). doi:10.1051/0004-6361/202346981.
- Veilleux, S., Maiolino, R., Bolatto, A. D., and Aalto, S. Cool outflows in galaxies and their implications. *Astronomy and Astrophysics Reviews*, 28(1):2 (2020). doi:10.1007/s00159-019-0121-9.
- Veilleux, S., Rupke, D. S. N., and Swaters, R. Warm Molecular Hydrogen in the Galactic Wind of M82. *Astrophysical Journal, Letters*, 700(2):L149–L153 (2009). doi:10.1088/0004-637X/700/2/L149.
- Verhamme, A., Schaerer, D., and Maselli, A. 3D Ly $\alpha$  radiation transfer. I. Understanding Ly $\alpha$  line profile morphologies. *Astronomy and Astrophysics*, 460(2):397–413 (2006). doi:10.1051/0004-6361:20065554.
- Weaver, J. R., Davidzon, I., Toft, S., et al. COSMOS2020: The galaxy stellar mass function. The assembly and star formation cessation of galaxies at  $0.2 < z \leq 7.5$ . *Astronomy and Astrophysics*, 677:A184 (2023). doi:10.1051/0004-6361/202245581.
- Whitaker, K. E., Ashas, M., Illingworth, G., et al. The Hubble Legacy Field GOODS-S Photometric Catalog. *Astrophysical Journal, Supplement*, 244(1):16 (2019). doi:10.3847/1538-4365/ab3853.
- Windhorst, R. A., Cohen, S. H., Jansen, R. A., et al. JWST PEARLS. Prime Extragalactic Areas for Reionization and Lensing Science: Project Overview and First Results. *Astronomical Journal*, 165(1):13 (2023). doi:10.3847/1538-3881/aca163.
- Yang, H., Malhotra, S., Gronke, M., et al. Green Pea Galaxies Reveal Secrets of Ly $\alpha$  Escape. *Astrophysical Journal*, 820(2):130 (2016). doi:10.3847/0004-637X/820/2/130.
- Yuan, Y., Krumholz, M. R., and Martin, C. L. The observable properties of cool winds from galaxies, AGN, and star clusters - II. 3D models for the multiphase wind of M82. *Monthly Notices of the RAS*, 518(3):4084–4105 (2023). doi:10.1093/mnras/stac3241.

- 
- Yui Dan, K., Seebeck, J., Veilleux, S., et al. JWST Discovery of a Very Fast Biconical Outflow of Warm Molecular Gas in the Nearby Ultra-Luminous Infrared Galaxy F08572+3915 NW. *arXiv e-prints*, arXiv:2412.05859 (2024). doi:10.48550/arXiv.2412.05859.